

TECHNISCHE UNIVERSITÄT MÜNCHEN

**MICROWAVE METAMATERIALS:  
Superlensing and  
Design of Low Reflection Coatings**

Ali Eren Culhaoglu

Vollständiger Abdruck der von der Fakultät für Elektrotechnik und Informationstechnik der Technischen Universität München zur Erlangung des akademischen Grades eines

Doktors der Naturwissenschaften (Dr. rer. nat.)

genehmigten Dissertation.

Vorsitzender: Univ.-Prof. Dr. sc. techn. Andreas Herkersdorf

Prüfer der Dissertation:

1. Univ.-Prof. Dr. techn. Peter Russer
2. Univ.-Prof. Dr. rer. nat. habil. Hans-Joachim Bungartz
3. Prof. Dr. Wolfgang J. R. Hofer, em.  
University of Victoria / Kanada

Die Dissertation wurde am 28.11.2011 bei der Technischen Universität München eingereicht und durch die Fakultät für Elektrotechnik und Informationstechnik am 11.07.2012 angenommen.



# Kurzfassung

Metamaterialien mit maßgeschneiderten und kontrollierbaren elektromagnetischen Eigenschaften bilden die Basistechnologie für neuartige Anwendungen in der Mikrowellentechnik, die mittels in der Natur vorkommenden Materialien schwer zu erreichen sind. Die Abbildungseigenschaften einer Metamaterial-Superlinse und die Gestaltung Metamaterial-basierter Antireflexionsbeschichtungen werden in dieser Arbeit untersucht. Mögliche Anwendungsgebiete finden sich in der Mikrowellensensorik und Radartarnung.

Neueste Fortschritte in der Mikro- und Nanotechnologie haben zu einem rasanten Anstieg des Interesses in der Realisierung von Metamaterialien geführt. Der Bereich von Metamaterialien umfasst ein breites Spektrum an künstlich zusammengesetzten elektromagnetischen Verbundwerkstoffen. In der Regel bestehen sie aus metallischen oder dielektrischen Einschlüssen oder Einheitszellen, die in einer gitterähnlichen Anordnung in ein Trägermaterial eingebettet werden. Für elektromagnetische Wellen, deren Wellenlänge deutlich größer als die der Einheitszelle ist, wirkt das gesamte Metamaterial wie ein homogener Stoff und kann mittels effektiven Stoffkonstanten makroskopisch beschrieben werden. Grundlegende Konzepte und Eigenschaften werden in Kapitel 2 dieser Arbeit behandelt.

Das Konzept einer Metamaterial-Superlinse, deren Auflösung unterhalb der Beugungsgrenze herkömmlicher Abbildungssysteme liegt, wird in Kapitel 3 behandelt. Eine ebene Platte aus Metamaterial bündelt die von einem beliebig gerichtetem Hertzischen Dipol ausgehenden Wellen in einer Abbildungsebene hinter der Platte. Ein beliebig gerichteter Hertzischer Dipol regt TE und TM Moden gleichzeitig an. Dabei führen Abweichungen von der idealen Abbildungskondition zu einer ungleichmäßigen Übertragung beider Moden und einer Verzerrung des Abbildes. Um dieses Phänomen näher zu untersuchen, wird eine analytische Lösung, basierend auf einer zweidimensionalen Fourier-Integraldarstellung der Felder im Spektralbereich, abgeleitet und die Feldverteilung im Bereich der Abbildungsebene numerisch ausgewertet.

In Kapitel 4 wird ein systematischer Ansatz zur Realisierung neuartiger Drude- und Lorentz-dispersiver Metamaterial-Radarabsorber beschrieben. Des Weiteren wird eine elektrisch dünne Metamaterial-basierte Antireflexionsbeschichtung entworfen, hergestellt und anschließend vermessen. Die elektromagnetischen Eigenschaften der Beschichtung werden anhand eines Ersatzschaltbildes, angelehnt an die Theorie gekoppelter Mikrostreifenleitungen, charakterisiert. Vorteile gegenüber konventionellen Radarabsorbern werden diskutiert und Optimierungsverfahren zur Steigerung der Effizienz gegeben. Mono und bistatische Radarquerschnittmessungen eines beschichteten metallischen Würfels werden bei Ka-Band (30 - 40 GHz) Frequenzen durchgeführt. Die Streuquerschnitte des beschichteten und unbeschichteten Würfels geben dabei Aufschluss über den Wirkungsgrad der Beschichtung. Messergebnisse werden mit der physikalischen Theorie der Beugung und Vollwellensimulationen verglichen. Auf eine Beschreibung der Beschichtung mit Impedanzrandbedingungen wird hingewiesen.



# Abstract

Metamaterials provide enabling technologies for several applications in the field of microwave engineering. The possibility of realizing materials with tailored and controllable electromagnetic properties which are hard to achieve with naturally occurring materials, has produced a major impact on the development of novel microwave devices. This work is devoted to the analysis of metamaterial superlenses and the design of metamaterial based low reflection coatings, providing the basis for novel applications in microwave imaging/sensing and radar cross section reduction.

Recent advances in micro- and nanofabrication technologies have resulted in a surge of interest in the realization of metamaterials, which constitute a broad class of artificially structured composite electromagnetic materials. As an ordinary material is composed of atoms or molecules, a metamaterial is assembled from lattices of “artificial” molecules or unit cells consisting of subwavelength sized metallo-dielectric scatterers. For wavelengths much larger than the unit cell size, the wave-material interaction can be described macroscopically by effective material parameters. Fundamental concepts and features of metamaterials are considered in Chapter 2 of this work.

The concept of metamaterial superlenses with imaging properties beyond that of diffraction limited systems is considered in Chapter 3. Imaging by a metamaterial slab with material parameters perturbed from the ideal imaging condition and excited by an arbitrarily oriented Hertzian dipole is investigated. An arbitrarily oriented dipole excites both TE and TM modes. A new type of image distortion, the unequal transmission of TE and TM portions of the fields, is identified and studied. A tool for evaluating the field intensities in the vicinity of the image plane is developed and the imaging characteristics of the slab are investigated in the spectral domain. The fields are represented in terms of a two-dimensional Fourier integral and numerically evaluated.

A systematic way of designing novel types of radar absorbing materials with realistic Drude and Lorentz dispersive metamaterials is described in the first part of Chapter 4. In the second part, a design for an electrically thin metamaterial based low reflection coating consisting of capacitively loaded strips is proposed, realized and measured. To characterize the electromagnetic response of the coating, an equivalent circuit model based on coupled microstrip line theory is developed. Advantages over conventional radar absorbing materials are illustrated and methods of increasing the performance are given. Mono- and bistatic radar cross section measurements of a coated metallic cube are carried out at Ka band (30 - 40 GHz) frequencies. The amount of scattering reduction is verified by comparing the scattering patterns of the coated and uncoated cube. Measurement results are compared to full wave and physical theory of diffraction simulations. Modeling the low reflection coating with impedance boundaries are pointed out.



# Acknowledgment

This thesis contains the work carried out during my doctoral studies initiated in March 2007 at the Microwaves and Radar Institute of the German Aerospace Center in Oberpfaffenhofen. Supervisors during the work have been Prof. Dr. Peter Russer from the Technische Universität München and Dr. habil. Andrey Osipov from the Microwaves and Radar Institute of the German Aerospace Center.

I would like to express my sincere gratitude to Prof. Dr. techn. Peter Russer for accepting me as a doctoral candidate. His invaluable comments and suggestions have always been a great inspiration to me and steered me in the right direction, especially in periods of difficulty. I am very grateful to him for providing me an additional workspace at the Technische Universität München, which gave me the possibility to cooperate with other colleagues and facilitated my entry into the subject.

I am endlessly grateful to Dr. habil. Andrey Osipov for his constant and tireless guidance, understanding and assistance. I was lucky to benefit from his vast and solid knowledge in electromagnetic theory and his inestimable experience in conducting scientific research. Without his support, it would have been impossible to complete this thesis.

I would like to express my sincere thanks to our group leader Dr. techn. Erich Kemptner for his endless administrative and technical support, for giving me the opportunity to work in such a lovely environment and proofreading my dissertation. His advices and comments has truly enriched the scope of this work.

I wish to thank our technician Stefan Thurner for his support regarding fabrication issues and conducting the measurements. Without him, the experimental results presented in Chapter 4 of this work would not have been possible.

My warmest thanks to Prof. Dr. Wolfgang J. R. Hoefer (Emeritus) from the Computational Electromagnetics Research Laboratory of the University of Victoria B.C. for providing me with Mefisto-3D-Pro, by which a significant part of Chapter 3 has come into being.



# Contents

<b>1</b>	<b>Introduction</b>	<b>1</b>
1.1	Motivation and Objectives . . . . .	2
1.2	Contributions of the Thesis . . . . .	3
1.3	Thesis Outline . . . . .	4
<b>2</b>	<b>Concept of Metamaterials</b>	<b>7</b>
2.1	General Definition . . . . .	7
2.2	Artificial Electromagnetic Materials . . . . .	7
2.3	Classification . . . . .	10
2.4	Wave Propagation . . . . .	12
2.5	Transmission Line Modeling . . . . .	13
2.5.1	Right-Handed Transmission Line . . . . .	14
2.5.2	Left-Handed Transmission Line . . . . .	15
2.5.3	Composite Right-Left-Handed Transmission Line . . . . .	16
2.6	Drude and Lorentz Dispersion . . . . .	19
2.7	Realization . . . . .	22
2.8	Applications . . . . .	25
2.9	Homogenization Methods . . . . .	27
2.10	Effective Parameter Extraction . . . . .	28
2.10.1	Strip-SRR Metamaterials . . . . .	29
2.10.2	CLS-SRR Metamaterials . . . . .	32
<b>3</b>	<b>Metamaterial Superlens</b>	<b>35</b>
3.1	Physical Background . . . . .	36
3.2	Analytical Formulation . . . . .	37
3.3	Analytical Properties . . . . .	40
3.4	Ideal Imaging . . . . .	42
3.5	Non-Ideal Imaging . . . . .	43
3.6	Results . . . . .	44
3.6.1	Small Amount of Absorption . . . . .	45
3.6.2	Unit Refractive Index . . . . .	49
3.6.3	Non-Unity Refractive Index . . . . .	51
3.6.4	Thickness of the Slab . . . . .	55
3.6.5	Aperture Size . . . . .	56
3.6.6	Excitation by Broadband Pulses . . . . .	57

<b>4</b>	<b>Metamaterial Microwave Absorbers</b>	<b>61</b>
4.1	Drude and Lorentz Dispersive Microwave Absorbers . . . . .	62
4.1.1	Principles of Operation . . . . .	62
4.1.2	Realization . . . . .	64
4.2	Metamaterial Low Reflection Coatings . . . . .	68
4.2.1	Principles of Operation . . . . .	68
4.2.2	Equivalent Circuit Model . . . . .	69
4.2.3	Design Example . . . . .	71
4.2.4	Optimization and Tuning . . . . .	72
4.2.5	Angle of Incidence and Polarization Dependence . . . . .	75
4.2.6	Realization . . . . .	77
4.2.7	Radar Cross Section Reduction . . . . .	78
4.2.8	Modeling with Impedance Boundaries . . . . .	81
<b>5</b>	<b>Results and Conclusion</b>	<b>83</b>
<b>A</b>	<b>Reflection and Transmission through Layered Media</b>	<b>87</b>
A.1	Semi-infinite Media . . . . .	87
A.2	Layered Media . . . . .	89
<b>B</b>	<b>Radar Cross Section</b>	<b>91</b>
	<b>List of Figures</b>	<b>95</b>
	<b>List of Tables</b>	<b>99</b>
	<b>Abbreviations and Symbols</b>	<b>101</b>
	<b>References</b>	<b>103</b>
	<b>Curriculum Vitae</b>	<b>114</b>

# 1

## Introduction

One of the basic features of civilization is the ability of mankind to utilize and control the properties of materials, whether natural or man made. The development of new materials has been vital to the development of mankind. Nowadays, microwave materials are being widely used in a variety of applications ranging from communication to sensing devices. The emergence of metamaterials with engineered and controllable electromagnetic properties enabled unique opportunities in the realization of enhanced microwave devices.

Metamaterials provide enabling technologies for several applications in the field of microwave engineering, such as antennas, filters, couplers, imaging systems and cloaking devices. Considerable efforts have been made in recent years to understand their electromagnetic properties. Several books with an extensive up to date collection of references have been published in this rapidly growing field [16; 18; 31; 34; 79].

Permittivity  $\epsilon$  and permeability  $\mu$  are the two major parameters used to characterize the electric and magnetic properties of materials. For certain applications in microwave engineering it is difficult to find a naturally occurring material with desired values of  $\epsilon$  and  $\mu$ . Metamaterials comprise a wide set of artificially structured composites with tunable  $\epsilon$  and  $\mu$  that are inaccessible or difficult to obtain with naturally occurring materials. There is no universally accepted uniform definition for metamaterials, a detailed discussion of which can be found in reviews [72] and [106].

As an ordinary material is made of atoms or molecules, a metamaterial is assembled from lattices of “artificial” molecules consisting of subwavelength sized metallo-dielectric scatterers or inclusions. If the size and periodicity of the inclusions is smaller than the wavelength, the metamaterial can be regarded as homogeneous and its properties can be represented by macroscopic effective material parameters  $\epsilon_r^{\text{eff}}$  and  $\mu_r^{\text{eff}}$ . The development of metamaterials is primarily concerned with the design of appropriate scatterers and their assembly into a bulk material. This provides the engineer with multiple degrees of freedom and makes it principally possible to engineer a material with desired values of  $\epsilon_r^{\text{eff}}$  and  $\mu_r^{\text{eff}}$ . The unit cells and inclusions of a metamaterial are scalable and can be easily designed to work at different frequency bands. Using modern micro- and nanofabrication techniques, manufacturing metamaterials with structure sizes and critical dimensions below 100  $\mu m$  and 100  $nm$ , respectively, has become possible.

# 1. INTRODUCTION

---

Materials with simultaneously negative values of  $\epsilon_r^{\text{eff}}$  and  $\mu_r^{\text{eff}}$ , known as double negative, negative refractive index, left-handed or backward wave materials, represent a special class of metamaterials. The negative refractive index  $n = -\sqrt{\epsilon_r^{\text{eff}}\mu_r^{\text{eff}}}$  constitutes thereby a peculiar property. An artificially structured metamaterial was shown to exhibit a negative index of refraction over a band of microwave frequencies at 5 GHz for the first time in [108]. The demonstration of a previously unexploited property and its subsequent verification [101] provided the basis for an impressive growth in the field of metamaterials.

## 1.1 Motivation and Objectives

The possibility of realizing materials with tailored and controllable electromagnetic properties which are hard to achieve with naturally occurring materials, has produced a major impact on the development of enhanced and novel microwave devices. This work is devoted to the analysis of imaging with metamaterial superlenses and the design of metamaterial based radar absorbing materials or low reflection coatings, providing a basis for enhanced devices in microwave imaging/sensing and radar cross section reduction technologies.

An intriguing feature of metamaterials is the possibility of realizing a superlens whose resolution is not subject to the traditional diffraction limit of a wavelength [3; 48; 59; 61]. A planar double negative metamaterial slab with  $\epsilon_r = \mu_r = -1$  acts as a collimating lens [117]. This is in sharp contrast to conventional lenses with a positive refractive index that need to have curved (convex or concave) surfaces to form an image. Apart from perfectly focusing the propagating waves, a double negative metamaterial slab can enhance the decaying evanescent part of the spectrum, so that in addition to the far-field components associated with a source the non-propagating near field components are also brought to a focus. Theoretically such a lens may offer imaging with infinite resolution [88].

The imaging characteristics of a double negative metamaterial slab have been considered up to now mainly in two dimensions, in combination with a line source [10; 28], and in three dimensions with a dipole oriented perpendicular to the surface of the slab [19; 37; 130]. In those cases only one type of mode is involved in the analysis, which depending on the type of excitation can be either TE or TM. A dipole oriented parallel to the interface of the slab, on the other hand, excites both type of modes simultaneously. These are transmitted unequally by the slab if either the slabs permittivity or permeability or both are perturbed from the ideal imaging condition of  $\epsilon_r = \mu_r = -1$ . Even a small perturbation in the slab material limits the spectrum of the transmitted field, resulting in a significant degradation of the image quality. Realistic metamaterials have unavoidable disadvantages of loss and narrow bandwidth, restricting their application. The superlens is therefore an idealization which is difficult to realize in reality and it is obvious that dispersion, losses and finite size of unit cells present in realistic double negative metamaterials degrade its imaging capabilities [72; 78; 84; 102; 110]. A common misconception regarding metamaterial

superlenses is that they are capable of focusing in three-dimensional space. However, a double negative metamaterial slab provides only two dimensional imaging and not focusing in three dimensional space [79].

By taking all these facts into account, it becomes an important task to analyze how well a double negative metamaterial superlens whose material parameters are slightly perturbed from the ideal imaging condition operates and to what extent imaging beyond the diffraction limit is possible. In this work, the imaging capabilities of realistic double negative metamaterial slabs excited by arbitrarily oriented Hertzian dipoles are investigated. A tool for evaluating the field intensities in the vicinity of the image plane is developed for this purpose. The imaging characteristics are investigated in the spectral domain where the fields are expanded in a two-dimensional Fourier integral and evaluated numerically.

Another interesting application area of metamaterial technology lies in the realization of novel cloaking devices [1; 5; 36; 98]. A cloaking device can virtually conceal an object that is placed inside it, leading to a significant amount of radar cross section reduction. A two dimensional cylindrical cloak made up of concentric metamaterial layers with variable refractive indices and operating at 8.5 GHz has been realized in [98]. Difficulties in realization, limitation to certain geometries or small electrical sizes, narrow band operation, polarization and angle of incidence dependence are major drawbacks of such cloaking devices. On the other hand, among the most practical and commonly used radar cross section reduction techniques is the application of radar absorbing materials or layers. Planar absorbers are thereby of particular interest since they are suitable for use in a wide variety of environments. Classical examples are Jaumann, Salisbury, and Dallenbach absorbers [64; 94]. Adjusting the electromagnetic specifications of the absorber to the given situation and its scope of application is an important task during the design process. The limited choice of naturally occurring materials with suitable dielectric and magnetic properties constitutes thereby a major challenge.

In recent years, metamaterials have been employed in the design of electrically thin radar absorbers or low reflection coatings [33; 114]. Metamaterial low reflection coatings have the benefit of being frequency scalable. Their performances and electromagnetic properties can be easily adjusted by a suitable choice and combination of resonant inclusions and durable materials such as Teflon<sup>®</sup>, ceramic or fiber/resin mixtures. Furthermore, metamaterial low reflection coatings are much thinner than conventional absorbers, by which a significant amount of weight reduction is achieved. They can withstand high mechanical stress and due to their high flexibility can be easily applied to uneven surfaces. In this work, a design for an electrically thin metamaterial low reflection coating is proposed, realized and measured.

## 1.2 Contributions of the Thesis

The main contributions of the thesis can be listed as follows:

- A complete analytical description of the imaging capabilities of a non-ideal double

## 1. INTRODUCTION

---

negative metamaterial slab excited by an arbitrarily oriented electric or magnetic dipole and the development of a numerical tool to simulate and study the spatial intensity distribution in the vicinity of the image plane

- Identification of a new type of image distortion, the unequal transmission of TE and TM portions of the fields, and feasibility studies of the imaging capabilities of realistic metamaterial superlenses with non-ideal material parameters, i.e.  $\epsilon_r \neq \mu_r \neq -1$  [23; 25]
- Investigation of the influence of the lens size (transverse extension) and thickness on the image quality [21; 27], as well as imaging with broadband pulses and Drude dispersive double negative slabs [22]
- A novel approach to the use of Drude and/or Lorentz dispersive metamaterials in the design of electrically thin microwave absorbers [24]
- A comprehensive and systematic study (theory, design, fabrication and experimental characterization) of truly planar metamaterial low reflection coatings consisting of a 2D periodic array of capacitively loaded strip inclusions
- Demonstration of applicability and effectiveness of the coatings in radar cross section reduction, by considering mono- and bistatic scattering measurements from an electrically large metallic cube coated with a fabricated sample [26]
- Illustration of the possibility of modeling the electromagnetic response of metamaterial low reflection coatings by an effective surface impedance, which can then be used in the framework of impedance boundary conditions to simulate the scattering cross section of electrically large and complex structures

### 1.3 Thesis Outline

The thesis is organized into three chapters whose contents are briefly described below:

Chapter 2 describes fundamental properties of metamaterials and provides the reader with a background in this rapidly growing field. A brief history of artificial materials with an emphasis on the subsequent steps leading to the general definition of metamaterials is presented. Unique properties of double negative metamaterials such as negative index of refraction, reversal of Snell's law and backward wave propagation are discussed. Common ways of realization are presented. Existing homogenization methods used for retrieving the effective material parameters of arbitrarily structured metamaterials are described and advantages/disadvantages are discussed. Milestones and new trends in application of metamaterial technology are mentioned and novel devices which have so far the most benefited from the use of metamaterials are pointed out. Finally, parameter fitting of dispersive models (PFDM) [76] is applied to determine the effective material parameters of metamaterials composed of metallic strip, capacitively loaded strip (CLS) and split ring resonator (SRR) inclusions.

Imaging capabilities of realistic double negative metamaterial slabs excited by arbitrarily oriented Hertzian dipoles are considered in Chapter 3. Differences between source excitations with dipole moments perpendicular and parallel to the interface of the slab are pointed out. Perturbations in the slab material and their influence on the resolving capabilities of the slab are investigated. A tool for evaluating the field intensities in the vicinity of the image plane is developed for this purpose. The fields are represented by a two dimensional Fourier integral in the spectral domain as described in [39] and numerically evaluated. The influence of a finite aperture (transverse extension of the slab) on the image quality is investigated next. Three dimensional full wave simulations of finite-size slabs are conducted. Finally, imaging of broadband pulses with a Gaussian spectrum are studied. A Drude model based, impedance matched to free space, composite right-left-handed (CRLH) slab is thereby considered. The configuration is studied numerically via the transmission line matrix (TLM) method [38; 54; 63].

Chapter 4 is devoted to a systematic design of planar microwave absorbers with realistic metamaterials. Design methodologies for a single layer Drude and Lorentz dispersive metamaterial absorber are presented in the first part of the chapter. The metamaterial unit cell is realized as a combination of metallic strip, capacitively loaded strip and split ring resonator inclusions. Effective material parameters obtained with the PFDM method [76], as described in Chapter 2, are used to describe the electromagnetic properties of the absorber. In the second part, a design for a truly planar metamaterial absorber consisting of a 2D periodic arrangement of capacitively loaded strip inclusions is presented and its applicability in the realization of electrically thin low reflection coatings is investigated. An equivalent circuit model based on coupled microstrip line theory is developed to characterize the electromagnetic response of the low reflection coating. The model is validated through full wave simulations. Optimization methods for adjusting the performance of the coating are given. A metamaterial low reflection coating with a unit cell size of  $\lambda/6$  and an overall thickness of  $\lambda/80$  at its operation band lying in the Ka band (30 - 40 GHz) is fabricated. Mono- and bistatic radar cross section measurements of a metallic cube coated with the realized sample are carried out. The cube has an edge length of approximately  $6\lambda$ . The amount of scattering reduction is verified by comparing the scattering patterns of the coated and uncoated cube. Measurement results are compared to full wave and physical theory of diffraction (PTD) simulations. Finally, modeling the low reflection coating with impedance boundaries are pointed out.

## 1. INTRODUCTION

---

## 2

# Concept of Metamaterials

Over the last several years there has been a surge of interest in metamaterials because of their potential to expand the range of electromagnetic properties in materials. Metamaterials comprise a wide set of artificially structured composites. Considerable efforts have been made in recent years to understand their electromagnetic properties. It is the purpose of this chapter to briefly review their origins, basic properties, ways of realization and potential application areas.

## 2.1 General Definition

Defined in a broad sense, metamaterials are composite electromagnetic materials that are assembled from regular or random lattices of artificially created unit cells consisting of dielectric or metallic inclusions embedded in a host. Although a periodic arrangement of unit cells is not necessary, it facilitates synthesis and analysis. As shown in Fig. 2.1, a metamaterial appears to be homogeneous for electromagnetic waves if the unit cells are electrically small. As a general rule of thumb a metamaterial should be assembled from unit cells with sizes smaller than  $\lambda/4$  [16]. The electromagnetic response can then be described by an effective relative permittivity  $\epsilon_r^{\text{eff}}$  and permeability  $\mu_r^{\text{eff}}$ . As the feature size of a unit cell approaches the wavelength, scattering effects begin to dominate and the effective medium description loses its validity.

Metamaterials comprise a wide set of artificially structured composites with tunable  $\epsilon_r^{\text{eff}}$  and  $\mu_r^{\text{eff}}$  that are inaccessible or difficult to obtain with naturally occurring materials. There is no uniform definition for them. A detailed discussion about metamaterials and their definition is provided in reviews [72] and [106].

## 2.2 Artificial Electromagnetic Materials

Although artificial dielectrics are usually not classified as metamaterials, the birth of metamaterials may be linked to the achievements of radar engineers in the 1940s - 50s. The concept of artificial dielectrics was first introduced in [65], where it was intended to be used as a low cost and light weight beam shaping element in lens

## 2. CONCEPT OF METAMATERIALS

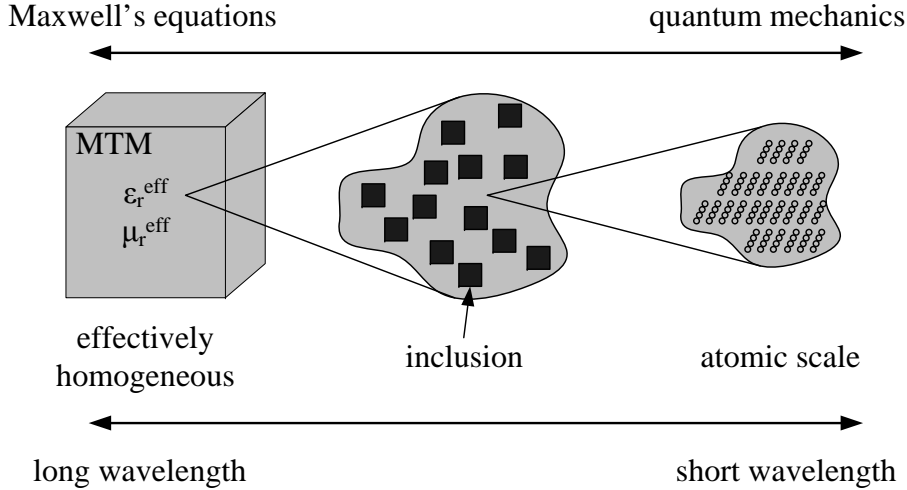


**Figure 2.1:** Feature size of a metamaterial with subwavelength inclusions embedded in a host.

antenna applications. Several lens designs consisting of metallic inclusions embedded in a dielectric matrix were proposed. Calling such artificial dielectrics metamaterials makes sense because the conducting properties of metals are being changed to a dielectric type behavior in the macroscopic scale.

A common example of artificial dielectrics is the wire medium, which has been known since 1960s [13]. It is formed by a regular lattice of conducting wires with radii that are small compared to the lattice period. The permittivity of a wire medium has plasma type frequency dependence and is negative over a broad range of frequencies below the plasma frequency. Recently, the wire medium has been rediscovered [89] and has attracted great attention.

Artificial magnetic materials are generally composed of inclusions with a resonant magnetic response. A widespread magnetic resonator is the split ring resonator (SRR) [90], which became popular after its application in the realization of double negative metamaterials [108]. Magnetic particles made of capacitively loaded loops, similar to the SRR, have been known for a long time [50; 97]. In [97] it was indicated that such particles could be used to obtain high values of permeability.

Another type of magnetic resonator is the Swiss roll [120], shown in Fig. 2.2(a). A Swiss roll resonator is made from a thin conducting sheet wrapped around a cylindrical cavity in a spiral shape and acts as a compact LC resonator. SRRs are more widely used than Swiss rolls since they are planar and can be easily manufactured using printed circuit board technology. An artificial magnetic composite formed by an array of SRRs possesses negative permeability within a narrow frequency band near the resonance frequency of a single resonator.

A combination of SRR and wire arrays, as shown in Fig. 2.2(b)-(c), yields a double negative metamaterial (DNG MTM) [108]. An alternative way of synthesizing DNG MTMs consists of periodically loading host transmission lines with series capacitors and shunt inductors, an example of which is shown in Fig. 2.2(d). There is a correspondence between negative permittivity and a shunt inductor, as well as between

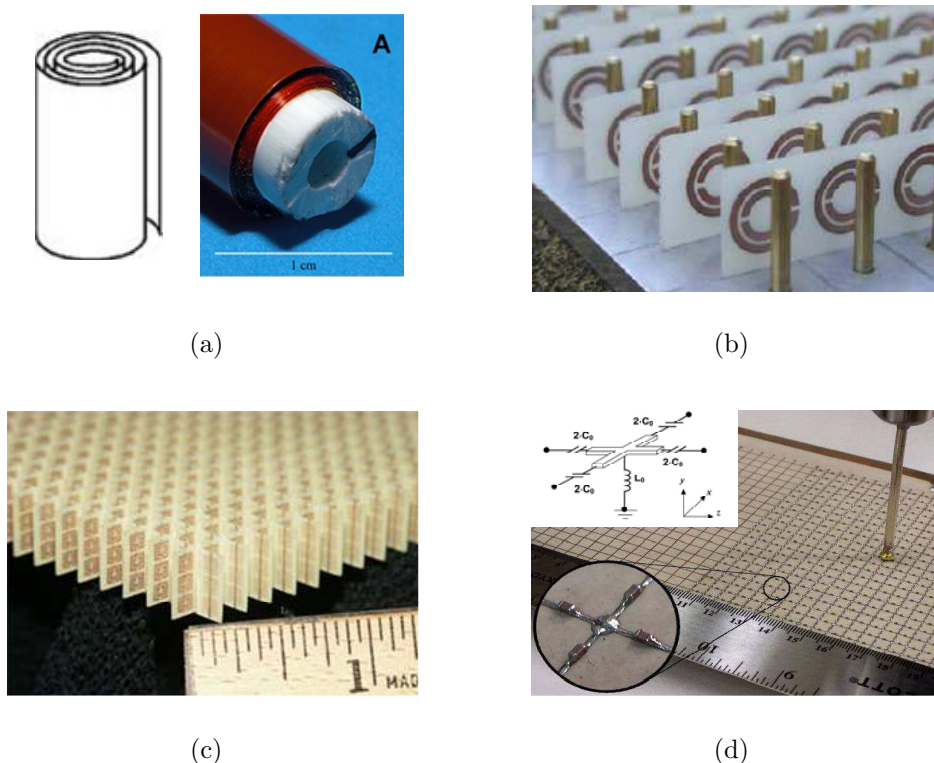


**Figure 2.2:** (a) Swiss roll type magnetic resonator, taken from [120], (b) realization of a 1D double negative metamaterial (DNG MTM) in terms of a periodic arrangement of metallic wires and split ring resonators (SRR), taken from [108], (c) planarized version with metallic strips, taken from [101], (d) 2D planar transmission line metamaterial composed of lumped inductors and capacitors, taken from [31].

negative permeability and a series capacitor [16]. This allows one to synthesize double negative transmission line metamaterials with a negative refractive index and will be investigated in detail in Sec. 2.5.

Electromagnetic bandgap (EBG) materials are another type of artificial electromagnetic material which offer the opportunity to control and manipulate electromagnetic wave propagation. They are periodical structures with a periodicity or unit cell size on the order of a wavelength. An effective medium description is therefore not possible and periodic media concepts must be used to describe their properties. At optical frequencies they are called photonic bandgap materials or crystals [62]. In EBG materials frequency bands exist within which the waves are highly attenuated and do not propagate [121]. The bandgaps are caused by spatial resonances in the material and depend on the periodicity and the propagation direction of the incident wave [62; 122]. EBG materials have found numerous applications in frequency selective devices at microwave and optical frequencies. In general, metamaterials occupy a special niche between homogeneous media and EBG materials.

Artificial impedance surfaces (AIS) and frequency selective surfaces (FSS) have received considerable attention in the last few years [85; 114]. In their simplest form, they are composed of an array of arbitrarily shaped conducting patches embedded

## 2. CONCEPT OF METAMATERIALS

---

in a dielectric substrate. They provide planar surfaces with tunable impedances and offer interesting applications in the design of low-profile antennas, thin absorbing screens, radomes and filters. The surface impedance is basically altered by modifying the texture of the patch array. If the feature size of the patch array is much smaller than the wavelength, their properties can be described by an effective surface impedance. This concept will be used in Chapter 4 during the design of an electrically thin metamaterial based microwave low reflection coating.

High impedance surfaces (HIS) [103] are a well known subclass of artificial impedance surfaces. A prominent example is the mushroom structure [105]. In contrast to a perfect electric conductor (PEC) where phase shift upon reflection is  $180^\circ$ , a HIS acts as magnetic wall or perfect magnetic conductor (PMC) with zero phase shift upon reflection.

Modern fabrication techniques and facilities enable more advanced electromagnetic materials with superior characteristics. Compound materials with structure sizes and critical dimensions below  $100 \mu\text{m}$  and  $100 \text{nm}$  have been realized. Although the concept of microwave metamaterials has still not been fully developed and far from being practically applicable, interest in scientific community is shifting towards photonic metamaterials, also known as optical metamaterials, designed to operate at THz, infrared, and visible frequencies [100].

### 2.3 Classification

The study of electromagnetic phenomena that occur during wave-material interactions is based on Maxwell's equations [57]. In a medium free of external charge and current they are defined as

$$\begin{aligned}\nabla \times \mathbf{E} &= -j\omega\mathbf{B} \\ \nabla \times \mathbf{H} &= j\omega\mathbf{D} \\ \nabla \cdot \mathbf{D} &= 0 \\ \nabla \cdot \mathbf{B} &= 0.\end{aligned}\tag{2.1}$$

The time factor  $e^{j\omega t}$  with angular frequency  $\omega$  and time  $t$  is assumed and suppressed.  $\mathbf{E}$  is the electric field vector in volt per meter [V/m],  $\mathbf{H}$  is the magnetic field vector in ampere per meter [A/m],  $\mathbf{D}$  is the electric displacement vector in coulomb per meter<sup>2</sup> [C/m<sup>2</sup>] and  $\mathbf{B}$  is the magnetic flux density in weber per meter<sup>2</sup> [Wb/m<sup>2</sup>]. The four field vectors are interrelated through the constitutive relations

$$\begin{aligned}\mathbf{D} &= \tilde{\epsilon} \cdot \mathbf{E} + \tilde{\xi} \cdot \mathbf{H} \\ \mathbf{B} &= \tilde{\mu} \cdot \mathbf{H} + \tilde{\zeta} \cdot \mathbf{E}\end{aligned}\tag{2.2}$$

with  $\tilde{\epsilon}$  and  $\tilde{\mu}$  the  $2^{\text{nd}}$  order permittivity and permeability tensors, respectively, and

$\tilde{\xi}$  and  $\tilde{\zeta}$  the  $2^{nd}$  order magneto-electric tensors responsible for any cross-coupling between the electric and magnetic field. The entries of these tensors are complex and the most general description of a material involves 72 parameters. Electromagnetic materials can be classified as:

- inhomogeneous : material parameters are functions of space coordinates
- nonlinear : material parameters depend on the strength of the electromagnetic field
- dispersive : material parameters depend on frequency

These can be further divided into following subclasses:

- isotropic : all tensors are scalars with  $\tilde{\xi} = 0$  and  $\tilde{\zeta} = 0$
- bi-isotropic : all tensors are scalars with  $\tilde{\xi} \neq 0$  and  $\tilde{\zeta} \neq 0$
- anisotropic :  $\tilde{\epsilon}$  and  $\tilde{\mu}$  are  $2^{nd}$  rank tensors with  $\tilde{\xi} = 0$  and  $\tilde{\zeta} = 0$
- bianisotropic :  $\tilde{\epsilon}$  and  $\tilde{\mu}$  are  $2^{nd}$  rank tensors with  $\tilde{\xi} \neq 0$  and  $\tilde{\zeta} \neq 0$

In an inhomogeneous medium material parameters are functions of position. A medium is nonlinear if material parameters vary with applied field strength and dispersive if a frequency dependence exists. In an isotropic medium material parameters are independent of field polarization, leading to scalar values of  $\tilde{\epsilon}$  and  $\tilde{\mu}$ . In an anisotropic medium, however, they vary depending on the direction of  $\mathbf{E}$  and  $\mathbf{H}$ . In this case  $\mathbf{D}$  and  $\mathbf{B}$  are not in the same direction as  $\mathbf{E}$  and  $\mathbf{H}$ ,  $\tilde{\epsilon}$  and  $\tilde{\mu}$  are tensors.

In a linear, isotropic ( $\tilde{\xi} = \tilde{\zeta} = 0$ ) and passive medium material parameters are expressed by the scalar quantities

$$\tilde{\epsilon} = \epsilon = \epsilon' - j\epsilon'' \quad \text{and} \quad \tilde{\mu} = \mu = \mu' - j\mu'', \quad (2.3)$$

where  $\epsilon'$  or  $\mu'$  represent the real parts and losses are characterized by  $\epsilon''$  or  $\mu''$ , which are positive for any passive medium and assumed time dependence of  $e^{j\omega t}$ . As shown in Fig. 2.3, if losses are negligible materials can be classified according to  $\epsilon'$  and  $\mu'$  into four groups:

- double positive (DPS) if  $\epsilon' > 0$  and  $\mu' > 0$
- double negative (DNG) if  $\epsilon' < 0$  and  $\mu' < 0$
- single negative (SNG)
  - $\mu$  negative (MNG) if  $\epsilon' > 0$  and  $\mu' < 0$
  - $\epsilon$  negative (ENG) if  $\epsilon' < 0$  and  $\mu' > 0$

The complex index of refraction  $n = \sqrt{\epsilon\mu}/\sqrt{\epsilon_0\mu_0}$  and characteristic impedance  $\eta = \sqrt{\mu/\epsilon}$  of a medium are important parameters for characterizing wave propagation. The square root has to be taken in consistency with causality. For passive media and time dependence of  $e^{j\omega t}$ , causality dictates that  $\text{Im}\{\epsilon\} < 0$  and  $\text{Im}\{\mu\} < 0$ . The proper choice of the square root function has been examined in [130], where  $\epsilon$  and  $\mu$  were expressed in polar form as  $\epsilon = |\epsilon| e^{j\phi_\epsilon}$  and  $\mu = |\mu| e^{j\phi_\mu}$ . The arguments of  $\epsilon$ ,  $\mu$ ,  $n$  and  $\eta$  are tabulated in Tab. 2.1 for different types of metamaterials.

## 2. CONCEPT OF METAMATERIALS

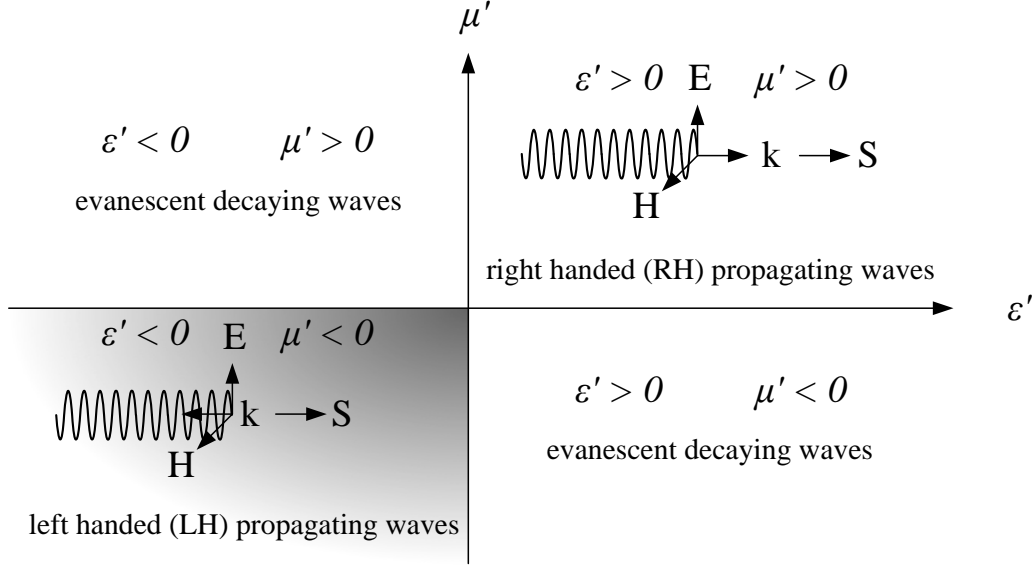


**Figure 2.3:** Material classification according to  $\epsilon'$  and  $\mu'$  and types of supported waves.

	$\phi_\epsilon$	$\phi_\mu$	$\phi_n$	$\phi_\eta$
DPS	$(-\frac{\pi}{2} \ 0]$	$(-\frac{\pi}{2} \ 0]$	$(-\frac{\pi}{2} \ 0]$	$(-\frac{\pi}{4} \ \frac{\pi}{4})$
DNG	$[-\pi \ -\frac{\pi}{2})$	$[-\pi \ -\frac{\pi}{2})$	$[-\pi \ -\frac{\pi}{2})$	$(-\frac{\pi}{4} \ \frac{\pi}{4})$
MNG	$[-\pi \ -\frac{\pi}{2})$	$(-\frac{\pi}{2} \ 0]$	$(-\frac{\pi}{2} \ 0]$	$(-\frac{\pi}{4} \ \frac{\pi}{4})$
ENG	$(-\frac{\pi}{2} \ 0]$	$(-\frac{\pi}{2} \ 0]$	$(-\frac{\pi}{2} \ 0]$	$(-\frac{\pi}{4} \ \frac{\pi}{4})$

**Table 2.1:** Sign of wave parameters, reproduced from the results in [130].

### 2.4 Wave Propagation

The coupled first-order vector differential equations (2.1) and (2.2) can be combined to obtain decoupled second-order vector differential equations for the two field quantities  $\mathbf{E}$  and  $\mathbf{H}$ . In a linear, isotropic and passive medium (2.3), together with the relations  $\nabla \cdot \epsilon \mathbf{E} = 0$  and  $\nabla \times \nabla \times \mathbf{E} = \nabla(\nabla \cdot \mathbf{E}) - \nabla^2 \mathbf{E}$ , the scalar wave equation for  $\mathbf{E} = E_x \hat{\mathbf{x}} + E_y \hat{\mathbf{y}} + E_z \hat{\mathbf{z}}$  is obtained in the Cartesian coordinate system as

$$(\nabla^2 + k^2) E_{x,y,z} = 0 \quad (2.4)$$

and has plane wave solutions of the form  $E = E_0 e^{-j(\mathbf{k} \cdot \mathbf{r} - \omega t)}$ . Here  $\mathbf{r} = x \hat{\mathbf{x}} + y \hat{\mathbf{y}} + z \hat{\mathbf{z}}$  and  $\mathbf{k} = k_x \hat{\mathbf{x}} + k_y \hat{\mathbf{y}} + k_z \hat{\mathbf{z}}$  are the position and wave vectors, respectively. The dispersion relation is given by  $k = \sqrt{k_x^2 + k_y^2 + k_z^2} = nk_0$  with  $k_0 = \omega/c_0$  the angular wavenumber in vacuum.

Most of the naturally occurring materials fall into the first quadrant of the graph plotted in Fig. 2.3, i.e.  $\epsilon' > 0$  and  $\mu' > 0$ . Disregarding losses ( $\epsilon'' = \mu'' = 0$ ), these materials are transparent to electromagnetic radiation since  $n^2 = \epsilon' \mu'$  is positive and  $k = nk_0$  is real. On the other hand,  $k$  is imaginary in quadrants II and IV where either  $\epsilon' < 0$  or  $\mu' < 0$ . Waves are evanescent in this case and no wave propagation

occurs.

A special place is occupied by DNG materials lying in quadrant III where  $\epsilon'$  and  $\mu'$  are simultaneously negative. Since  $n^2 = \epsilon'\mu'$  remains positive and  $k = nk_0$  is real, waves can still propagate in such a medium. The refractive index is negative in this case (Tab. 2.1), i.e.  $n = -\sqrt{|\epsilon'|\mu'}$ .

A peculiar property of DNG medium is that Snell's law (A.2) is reversed and negative refraction occurs at DPS-DNG interfaces [34]. Negative refraction was verified experimentally for the first time in [101], where refraction from a double negative metamaterial prism consisting of metallic wires ( $\epsilon < 0$ ) and SRRs ( $\mu < 0$ ) has been studied at X band ( $\approx 10$  GHz) frequencies.

Another major characteristic of DNG media is that plane waves are propagating backward in such a medium. The existence of backward waves and fundamental properties of wave propagation in DNG medium have been known for a long time [99; 117]. In a DPS medium with  $\epsilon' > 0$  and  $\mu' > 0$ ,  $\mathbf{E}$ ,  $\mathbf{H}$ , and  $\mathbf{k}$  form a right-handed orthogonal system of vectors such that

$$\mathbf{k} \times \mathbf{E} = \omega\mu'\mathbf{H} \quad (2.5)$$

$$\mathbf{k} \times \mathbf{H} = -\omega\epsilon'\mathbf{E}. \quad (2.6)$$

On the other hand, in a DNG medium with  $\epsilon' < 0$  and  $\mu' < 0$

$$\mathbf{k} \times \mathbf{E} = -\omega|\mu'|\mathbf{H} \quad (2.7)$$

$$\mathbf{k} \times \mathbf{H} = \omega|\epsilon'|\mathbf{E}, \quad (2.8)$$

showing that  $\mathbf{E}$ ,  $\mathbf{H}$ , and  $\mathbf{k}$  now form a left-handed triplet.

This constitutes the origin of the term left-handed (LH) media. The flow of power flux per unit area is given by the Poynting vector  $\mathbf{S} = \mathbf{E} \times \mathbf{H}$  with units of watts per meter<sup>2</sup> [W/m<sup>2</sup>] and is the same in DPS and DNG media.  $\mathbf{E}$ ,  $\mathbf{H}$ , and  $\mathbf{S}$  always form a right handed (RH) triplet. The only difference is that energy ( $\mathbf{S}$ ) and wavefronts ( $\mathbf{k}$ ) travel in opposite directions in DNG media (Fig. 2.3). Based on the transmission line approach, this phenomenon and the relation between phase and group velocity in DNG media will be discussed in more detail in the following section.

## 2.5 Transmission Line Modeling

The transmission line approach in modeling double negative media was first introduced in [31] and will be employed throughout this section to investigate wave propagation in such media. Homogeneous and isotropic media are thereby represented in terms of equivalent transmission line circuits, where the electric permittivity and magnetic permeability are modeled by distributed network elements [95]. Due to the discrete nature of metamaterials, i.e. finite unit cell size, the transmission line modeling provides an insightful tool for the analysis and design of double negative metamaterials [16; 123]. In order to facilitate a better understanding of the fundamental characteristics of double negative media, only lossless lines will be considered.

## 2. CONCEPT OF METAMATERIALS

---

### 2.5.1 Right-Handed Transmission Line

For the lossless case, the distributed circuit model of a conventional (right-handed) and homogeneous (continuous and invariant along the direction of propagation) transmission line is shown in Fig. 2.4(a). It consists of an infinitesimal line of length  $\Delta z$  with a series per unit length inductance  $L'_R$  (Henries per meter) and a shunt per unit length capacitance  $C'_R$  (Farads per meter). The voltages and currents at the terminals are related to each other by Kirchoff's voltage and current laws. For steady-state sinusoidal voltages and currents based on cosine phasors with  $V(z, t) = \text{Re} \{V(z)e^{j\omega t}\}$  and  $I(z, t) = \text{Re} \{I(z)e^{j\omega t}\}$  the relations are

$$\begin{aligned} V(z) &= Z' I(z) \Delta z + V(z + \Delta z) \\ I(z) &= Y' V(z + \Delta z) \Delta z + I(z + \Delta z), \end{aligned} \quad (2.9)$$

with  $Z' = j\omega L'_R$  the per unit length impedance and  $Y' = j\omega C'_R$  the per unit length admittance of the transmission line. Assuming that  $\Delta z \rightarrow 0$  and expanding  $V(z + \Delta z)$  and  $I(z + \Delta z)$  in a Taylor series to first order in  $\Delta z$ , i.e.

$$\begin{aligned} V(z + \Delta z) &= V(z) + \frac{\partial V(z)}{\partial z} \Delta z \\ I(z + \Delta z) &= I(z) + \frac{\partial I(z)}{\partial z} \Delta z, \end{aligned} \quad (2.10)$$

the well known telegrapher's equations are obtained as:

$$\begin{aligned} \frac{\partial V(z)}{\partial z} &= -Z' I(z) = -j\omega L'_R I(z) \\ \frac{\partial I(z)}{\partial z} &= -Y' V(z) = -j\omega C'_R V(z). \end{aligned} \quad (2.11)$$

The voltage and current wave equations are derived by differentiating these equations with respect to  $z$ , and combining the results in two different ways yields

$$\begin{aligned} \frac{\partial^2 V}{\partial z^2} + k^2 V(z) &= 0 \\ \frac{\partial^2 I}{\partial z^2} + k^2 I(z) &= 0. \end{aligned} \quad (2.12)$$

The propagation constant  $k$  and characteristic impedance  $Z_0$  of the transmission line are determined from  $Z'$  and  $Y'$  as

$$k = -j\sqrt{Z'Y'} = \omega\sqrt{L'_R C'_R} \quad \text{and} \quad Z_0 = \sqrt{\frac{Z'}{Y'}} = \sqrt{\frac{L'_R}{C'_R}}. \quad (2.13)$$

Traveling wave solutions for (2.12) are  $V(z) = V^+e^{-jkz} + V^-e^{jkz}$  and  $I(z) = I^+e^{-jkz} + I^-e^{jkz}$ , representing the sum of a forward traveling wave and a backward traveling wave. The  $e^{-jkz}$  term represents wave propagation in the  $+z$  direction and the  $e^{jkz}$  represents wave propagation in the  $-z$  direction.  $V^+$ ,  $V^-$ ,  $I^+$  and  $I^-$  are the amplitudes of the forward and backward traveling voltage and current waves.

The phase ( $v_p$ ) and group ( $v_g$ ) velocities of the waves guided by a right handed transmission line are determined from the propagation constant as

$$v_p = \frac{\omega}{k} = \frac{1}{\sqrt{L'_R C'_R}} \quad \text{and} \quad v_g = \frac{\partial \omega}{\partial k} = \left[ \frac{\partial k}{\partial \omega} \right]^{-1} = \frac{1}{\sqrt{L'_R C'_R}} \quad (2.14)$$

and can also be inferred from the  $\omega - k$  (dispersion) diagram plotted in Fig. 2.4(b). For a right handed transmission line the dispersion is linear and the phase and group velocities are both positive and parallel, confirming forward propagation. The refractive index  $n$  which is the ratio of  $v_p$  to  $c_0$  (the speed of light in vacuum) is also positive.

Comparing (2.12) and (2.4) and mapping  $V(z)$ ,  $I(z)$  in the transmission line solution to  $E_y(z)$ ,  $-H_x(z)$  in the field solution, the distributed inductance  $L'_R$  and capacitance  $C'_R$  of the transmission line become equivalent to the permittivity  $\epsilon$  and permeability  $\mu$  of a homogeneous medium supporting transverse electromagnetic (TEM) wave propagation.

As a result of the equivalence between  $\epsilon$  and  $\mu$  characterizing wave propagation in media and the series impedance  $Z'$  and the shunt admittance  $Y'$  of the distributed circuit model, following relations are established:

$$\epsilon = \frac{Y'}{j\omega} = C'_R \quad \text{and} \quad \mu = \frac{Z'}{j\omega} = L'_R. \quad (2.15)$$

### 2.5.2 Left-Handed Transmission Line

A left-handed (LH) homogeneous transmission line (Fig. 2.5(a)) is the electrical dual of the conventional right-handed line and consists of a times unit length series capacitance  $C'_L$  in parallel with a times unit length inductance  $L'_L$ , so that the inductive and capacitive roles are exchanged.

The permeability and permittivity are related to the per unit length impedance and admittance of the equivalent transmission line by [16]

$$\epsilon(\omega) = \frac{Y'}{j\omega} = -\frac{1}{\omega^2 L'_L} \quad \text{and} \quad \mu(\omega) = \frac{Z'}{j\omega} = -\frac{1}{\omega^2 C'_L}, \quad (2.16)$$

both of which are dispersive and negative, yielding a dispersive negative index of refraction  $n(\omega) = \sqrt{\epsilon(\omega)\mu(\omega)}$ . The propagation constant and characteristic impedance of the line are

## 2. CONCEPT OF METAMATERIALS

---

$$k = -j\sqrt{Z'Y'} = -\frac{1}{\omega\sqrt{L'_L C'_L}} \quad \text{and} \quad Z_0 = \sqrt{\frac{Z'}{Y'}} = \sqrt{\frac{L'_L}{C'_L}}, \quad (2.17)$$

where the negative square root has been chosen for  $k$ . The phase and group velocities of the waves guided by a left-handed transmission line are

$$v_p = \frac{\omega}{k} = -\omega^2\sqrt{L'_L C'_L} \quad \text{and} \quad v_g = \frac{\partial\omega}{\partial k} = \omega^2\sqrt{L'_L C'_L}, \quad (2.18)$$

which show that backward waves with opposite signs of phase and group velocities are supported by a left-handed transmission line. These results can also be seen from the dispersion diagram of a left-handed transmission line which is plotted in Fig. 2.5(b).

The group velocity  $v_g$  associated with the direction of power flow or Poynting vector is positive, whereas the phase velocity  $v_p$  associated with the direction of the propagation constant  $k = \omega/v_p$  is negative. Since the index of refraction is the ratio of  $v_p$  to  $c_0$ , with  $c_0$  the speed of light in vacuum, it can also be concluded that the refractive index is negative in this case.

Considering the equivalent circuit of a conventional right handed transmission line (Fig. 2.4(a)), it can be inferred that reducing the line length  $\Delta z$  also reduces the series inductance  $L'_R\Delta z$  as well as the parallel capacitance  $C'_R\Delta z$  by the same amount. On the other hand, when the length of the dual left-handed transmission line is reduced, the series capacitance  $C'_L/\Delta z$  and parallel inductance  $L'_L/\Delta z$  increase by the same amount and grow to infinity as  $\Delta z \rightarrow 0$ . As stated in [125], it is therefore impossible to realize completely homogeneous double negative metamaterials. Only a discrete realization is possible.

In addition to that, due to unavoidable parasitic effects, it is practically impossible to realize purely left-handed metamaterials [16]. A parasitic capacitance and inductance is always present in a left-handed transmission line, yielding a composite right-left-handed (CRLH) transmission line shown in Fig. 2.6(a). The CRLH transmission line [16] represents the most general equivalent circuit model of realistic double negative metamaterials and its characteristics will be investigated in the following section.

### 2.5.3 Composite Right-Left-Handed Transmission Line

The composite right-left-handed (CRLH) transmission line is composed of a per unit length series inductance ( $L'_R$ ) and shunt capacitance ( $C'_R$ ) as well as a times unit length series capacitance ( $C'_L$ ) and shunt inductance ( $L'_L$ ). The per-unit length impedance  $Z'$  and admittance  $Y'$  are given as [16]

$$Z'(\omega) = j \left( \omega L'_R - \frac{1}{\omega C'_L} \right) \quad \text{and} \quad Y'(\omega) = j \left( \omega C'_R - \frac{1}{\omega L'_L} \right), \quad (2.19)$$

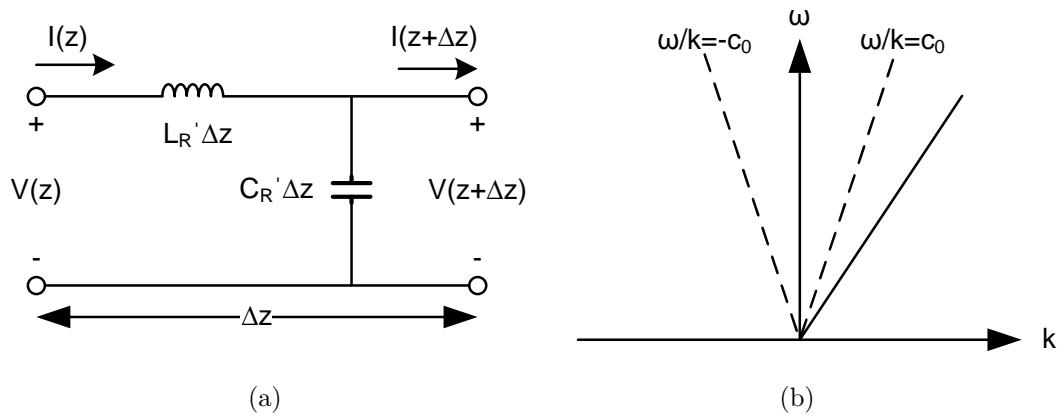


**Figure 2.4:** (a) Distributed parameter model of a right handed transmission line and (b) corresponding dispersion diagram.

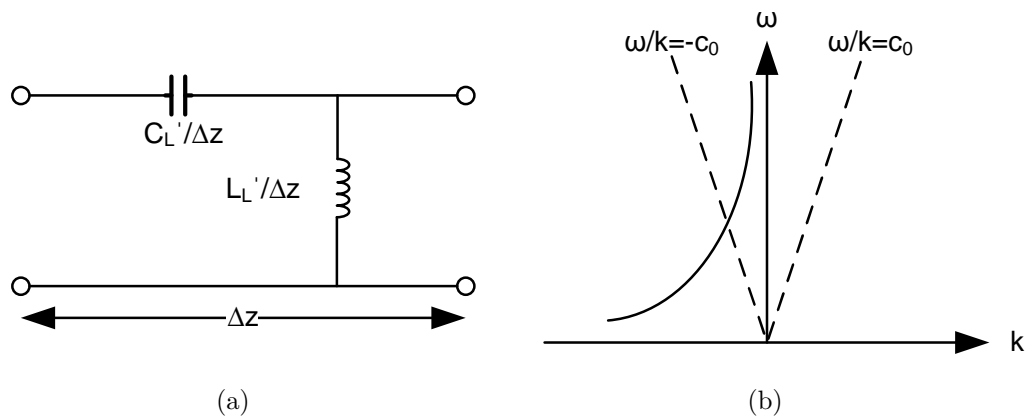


**Figure 2.5:** (a) Distributed parameter model of a left-handed transmission line and (b) corresponding dispersion diagram.

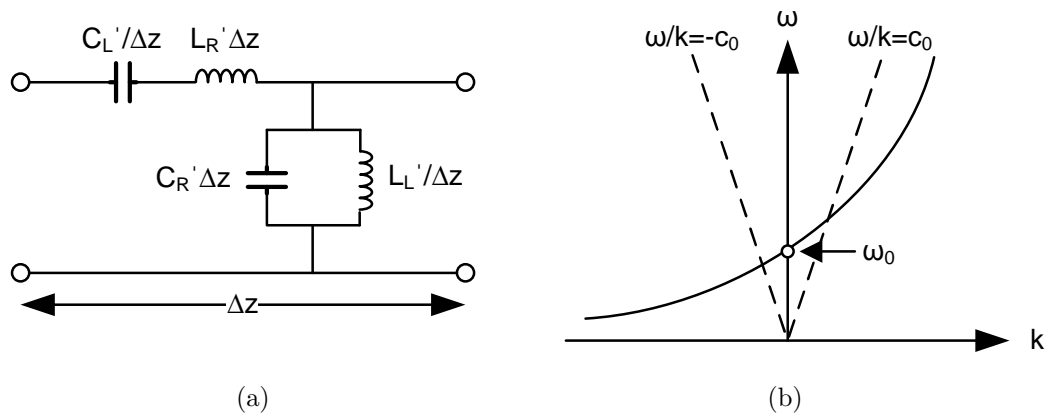


**Figure 2.6:** (a) Distributed parameter model of a composite right-left-handed transmission line and (b) corresponding dispersion diagram.

## 2. CONCEPT OF METAMATERIALS

---

from which the expressions of  $\epsilon$  and  $\mu$  can be obtained in a similar way as it has been done in the previous sections, yielding

$$\mu(\omega) = L'_R - \frac{1}{\omega^2 C'_L} \quad \text{and} \quad \epsilon(\omega) = C'_R - \frac{1}{\omega^2 L'_L}. \quad (2.20)$$

The CRLH transmission line concept provides a general model for a realistic description of metamaterials with both left and right handed frequency bands. Both  $\epsilon(\omega)$  and  $\mu(\omega)$  can be either positive or negative, depending on the frequency range. It is usually designed in the balanced configuration, leading to a continuous transition between the right- and left-handed frequency bands.

When the series ( $\omega_{se}$ ) and shunt ( $\omega_{sh}$ ) resonances

$$\omega_{se} = \frac{1}{\sqrt{L'_R C'_L}} \quad \text{and} \quad \omega_{sh} = \frac{1}{\sqrt{L'_L C'_R}}, \quad (2.21)$$

are equal, such that  $L'_R C'_L = L'_L C'_R$ , the CRLH transmission line is balanced. In this case the propagation constant and characteristic impedance are given by [16]

$$k = k_{RH} + k_{LH} = \omega \sqrt{L'_R C'_R} - \frac{1}{\omega \sqrt{L'_L C'_L}} \quad \text{and} \quad Z_0 = \sqrt{\frac{L'_R}{C'_R}} = \sqrt{\frac{L'_L}{C'_L}}. \quad (2.22)$$

The propagation constant splits up into a right handed ( $k_{RH}$ ) and a left-handed ( $k_{LH}$ ) part with a transition frequency occurring at

$$\omega_0 = \omega_{se} = \omega_{sh} = \frac{1}{\sqrt[4]{L'_R C'_R L'_L C'_L}}. \quad (2.23)$$

In summary, in a balanced CRLH transmission line, the series capacitance and shunt inductance provide left-handedness (anti parallel phase and group velocities) for  $\omega < \omega_0$ , whereas the series inductance and shunt capacitance provide the right-handedness (parallel phase and group velocities) for  $\omega > \omega_0$ . The resulting dispersion diagram is shown in Fig. 2.6(b). A detailed investigation of CRLH transmission lines, including the unbalanced case, relations for the phase and group velocities, can be found in [16; 31; 123].

It has to be emphasized that the previous analysis is only valid in the homogeneous limit ( $\Delta z \rightarrow 0$ ) and the line length (or unit cell size) is much smaller than the wavelength. As a rule of thumb the unit cell should be smaller than  $\lambda/4$  [16]. CRLH materials are not available in nature and have to be synthesized artificially. A common way of realization consists in loading host transmission line networks with lumped elements (Sec. 2.7). Therefore, such structures should be regarded as effectively homogeneous and can be described as an ideal (homogeneous) transmission line only for a restricted range of frequencies. If the effective homogeneity requirements are not met, the propagation characteristics are determined from a single unit cell us-

ing the Floquet theorem, which serves as a basis for the study of periodic structures [31; 57; 123].

## 2.6 Drude and Lorentz Dispersion

Simultaneously negative values of  $\epsilon$  and  $\mu$  can be realized only when there is frequency dispersion. Drude and Lorentz dispersion models are frequently employed in analytical and numerical modeling of realistic double neagive metamaterials. Examples and various modifications of these models can be found in [34]. In this work, only Drude and Lorentz dispersion are considered. The unit cell equivalent circuit representation of Drude and Lorentz dispersion is given in Fig. 2.7 [126].

The Lorentz model gives the frequency dependence of  $\epsilon_r(\omega) = \epsilon(\omega)/\epsilon_0$  or  $\mu_r(\omega) = \mu(\omega)/\mu_0$  as

$$\epsilon_r(\omega) = \epsilon_r(\infty) - \frac{\omega_{pe}^2}{\omega^2 - \omega_{0e}^2 - j\omega\Gamma_e} = \epsilon_r(\infty) - \frac{\omega_{pe}^2(\omega^2 - \omega_{0e}^2)}{(\omega^2 - \omega_{0e}^2)^2 + (\omega\Gamma_e)^2} - j \frac{\omega\Gamma_e\omega_{pe}^2}{(\omega^2 - \omega_{0e}^2)^2 + (\omega\Gamma_e)^2}$$

or

$$\mu_r(\omega) = \mu_r(\infty) - \frac{\omega_{pm}^2}{\omega^2 - \omega_{0m}^2 - j\omega\Gamma_m} = \mu_r(\infty) - \frac{\omega_{pm}^2(\omega^2 - \omega_{0m}^2)}{(\omega^2 - \omega_{0m}^2)^2 + (\omega\Gamma_m)^2} - j \frac{\omega\Gamma_m\omega_{pm}^2}{(\omega^2 - \omega_{0m}^2)^2 + (\omega\Gamma_m)^2} \quad (2.24)$$

with  $\epsilon_r, \mu_r(\infty) > 0$  the material parameter in the high frequency limit,  $\omega_{pe,pm} = 2\pi\nu_{pe,pm}$  the angular plasma frequency,  $\omega_{0e,0m} = 2\pi\nu_{0e,0m}$  the angular resonance frequency and  $\Gamma_{e,m}$  the damping amplitude.

The Drude model is a special case of the Lorentz model and is obtained by setting  $\omega_{0e,0m} = 0$ . It is given by

$$\epsilon_r(\omega) = \epsilon(\infty) - \frac{\omega_{pe}^2}{\omega^2 - j\omega\Gamma_e} = \epsilon_r(\infty) - \frac{\omega_{pe}^2}{\omega^2 + \Gamma_e^2} - j \frac{\omega_{pe}^2}{\omega^3 + \omega\Gamma_e^2}$$

or

$$\mu_r(\omega) = \mu(\infty) - \frac{\omega_{pm}^2}{\omega^2 - j\omega\Gamma_m} = \mu_r(\infty) - \frac{\omega_{pm}^2}{\omega^2 + \Gamma_m^2} - j \frac{\omega_{pm}^2}{\omega^3 + \omega\Gamma_m^2}. \quad (2.25)$$

In a lossless, linear and isotropic medium, under the assumption that both  $\epsilon$  and  $\mu$  are non dispersive,  $\epsilon'' \ll \epsilon'$  and  $\mu'' \ll \mu'$ , the energy density relation is given by [40; 70]

## 2. CONCEPT OF METAMATERIALS

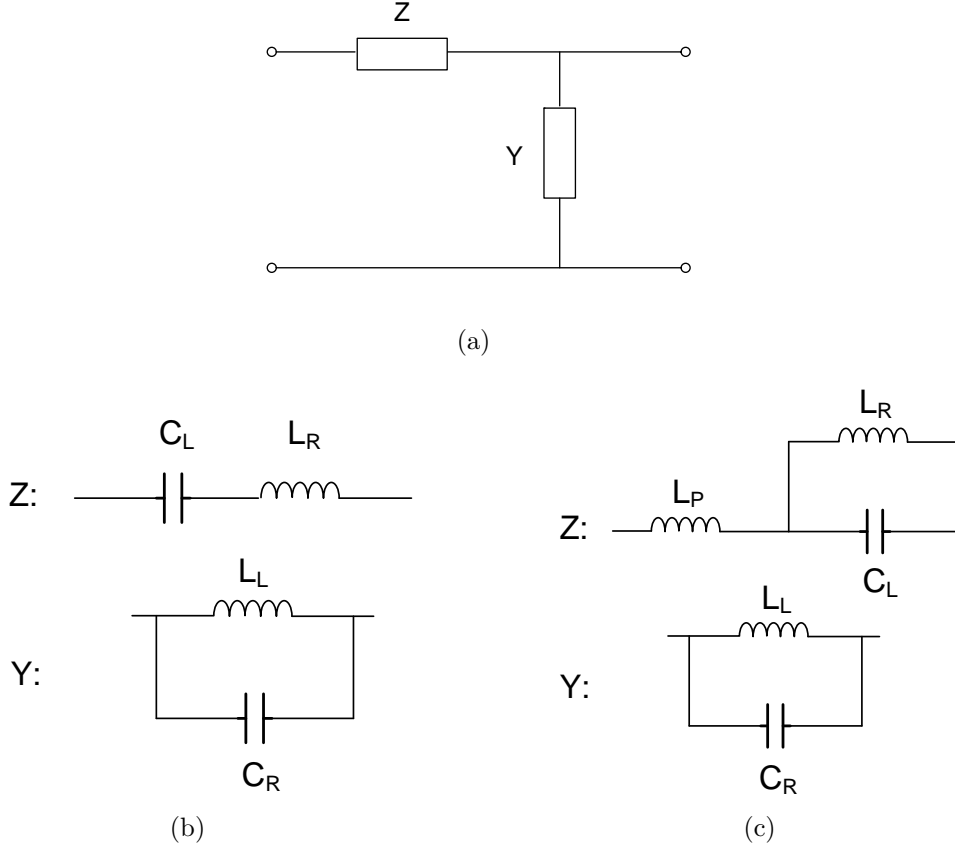


**Figure 2.7:** (a) Equivalent circuit representation of a metamaterial unit cell of size  $d \ll \lambda$  with (b) Drude and (c) Lorentz dispersion as taken from [126].

$$W = \frac{1}{2} \epsilon' |\mathbf{E}|^2 + \frac{1}{2} \mu' |\mathbf{H}|^2 \quad (2.26)$$

and is measured in units of joules per meter<sup>3</sup> [J/m<sup>3</sup>].  $W$  becomes negative for  $\epsilon' < 0$  and  $\mu' < 0$ , representing an unphysical result. In a dispersive medium where  $\epsilon$  and  $\mu$  are functions of frequency, on the other hand, it can be shown [70] that the energy density relation generalizes to

$$W = \frac{1}{2} \left\{ \frac{\partial[\omega\epsilon'(\omega)]}{\partial\omega} |\mathbf{E}|^2 + \frac{\partial[\omega\mu'(\omega)]}{\partial\omega} |\mathbf{H}|^2 \right\}. \quad (2.27)$$

The conditions

$$\frac{\partial[\omega\epsilon'(\omega)]}{\partial\omega} > 0 \quad \text{and/or} \quad \frac{\partial[\omega\mu'(\omega)]}{\partial\omega} > 0 \quad (2.28)$$

ensure thereby that  $W > 0$ .

In Drude and Lorentz dispersive metamaterials the condition of positive energy

density is always satisfied. Substituting (2.24) with  $\Gamma_e = 0$  into (2.28) yields

$$\begin{aligned} \frac{\partial[\omega\epsilon_r(\omega)]}{\partial\omega} &= \epsilon_r(\infty) - \frac{\partial}{\partial\omega} \left[ \frac{\omega\omega_{pe}^2}{\omega^2 - \omega_{0e}^2} \right] \\ &= \epsilon_r(\infty) + \frac{\omega_{pe}^2(\omega^2 + \omega_{0e}^2)}{(\omega^2 - \omega_{0e}^2)^2} > 0. \end{aligned} \quad (2.29)$$

The same procedure can be conducted with the Drude model, yielding

$$\begin{aligned} \frac{\partial[\omega\epsilon_r(\omega)]}{\partial\omega} &= \epsilon_r(\infty) - \frac{\partial}{\partial\omega} \left[ \frac{\omega_{pe}^2}{\omega} \right] \\ &= \epsilon_r(\infty) + \frac{\omega_{pe}^2}{\omega^2} > 0 \end{aligned} \quad (2.30)$$

It is obvious that the same results hold in the case of a Drude or Lorentz dispersive  $\mu_r(\omega)$ , as a result of which it can be concluded that Drude and Lorentz models satisfy the requirements of positive energy density.

Furthermore, in a double Lorentz dispersive medium with equal material parameters, i.e.  $\epsilon_r(\infty) = \mu_r(\infty) = 1$ ,  $\omega_p = \omega_{pe} = \omega_{pm}$ ,  $\omega_0 = \omega_{0e} = \omega_{0m}$  and  $\Gamma = \Gamma_e = \Gamma_m$ ,

$$\epsilon_r(\omega) = \mu_r(\omega) = 1 - \frac{\omega_p^2}{\omega^2 - \omega_0^2 - j\omega\Gamma}. \quad (2.31)$$

If losses are small ( $\Gamma \ll 1$ ), they can be expressed as

$$\epsilon_r(\omega) = \mu_r(\omega) = \frac{\omega^2 - \omega_x^2}{\omega^2 - \omega_p^2} \quad (2.32)$$

with  $\omega_x = \sqrt{\omega_0^2 + \omega_p^2}$ .

As shown in Fig. 2.8(a),  $\epsilon_r(\omega)$  and  $\mu_r(\omega)$  are negative for  $\omega_0 < \omega < \omega_x$ . The phase  $v_p$  and group  $v_g$  velocities are given by (Sec. 2.5)

$$v_p = \frac{\omega}{k} = c_0/n \quad \text{and} \quad v_g = \frac{\partial\omega}{\partial k} = c_0/\frac{\partial[n\omega]}{\partial\omega}. \quad (2.33)$$

and can be determined from the dispersion diagram shown in Fig. 2.8(b). For  $\omega_0 < \omega < \omega_x$   $v_p$  is negative. On the other hand,  $v_g$  is always positive. It is therefore obvious that  $v_p$  and  $v_g$  are anti parallel if  $\epsilon_r(\omega) < 0$  and  $\mu_r(\omega) < 0$ . In other words, if  $v_p$  and  $v_g$  are anti parallel,  $\epsilon_r(\omega) < 0$  and  $\mu_r(\omega) < 0$  and the medium is characterized by a negative refractive index.

## 2. CONCEPT OF METAMATERIALS

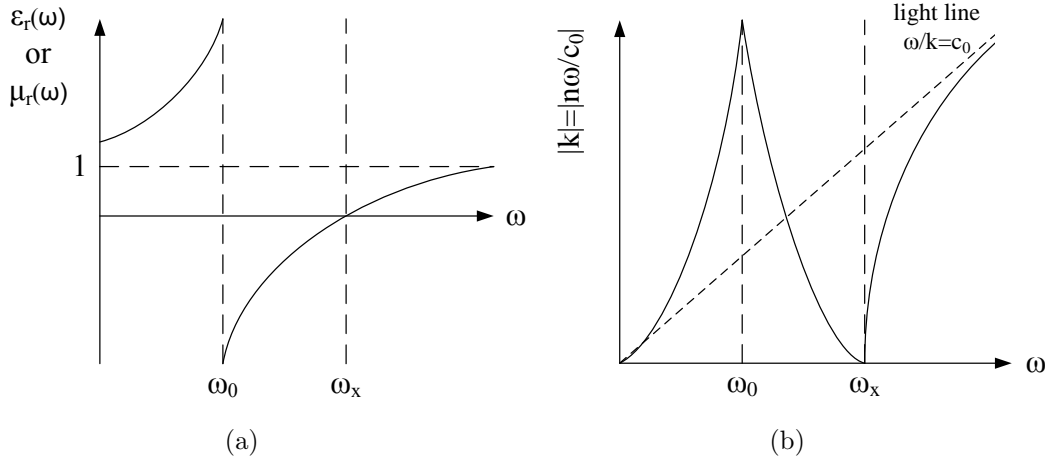


**Figure 2.8:** (a) Material parameters of a Lorentz dispersive medium with equal  $\epsilon_r(\omega)$  and  $\mu_r(\omega)$ , (b) corresponding dispersion relation.

### 2.7 Realization

Realization of metamaterials can be split into two major categories; the resonant and transmission line approaches. In the resonant approach the electric or magnetic polarizability of a host medium is modified through embedding subwavelength sized resonant inclusions. The transmission line approach, on the other hand, consists of loading host transmission line networks with lumped elements such as capacitors, inductors and resistors. The resonant approach is discussed first.

A periodic arrangement of infinitely long and electrically thin metallic wires, as shown on the left of Fig. 2.9, is commonly used to influence the electric polarizability of a host medium. The overall response is Drude dispersive (2.25). A quasi-static modeling in the low frequency limit [114], with the electric field polarized parallel to the wires ( $y$  axis), predicts the plasma frequency for the lossless case with  $\Gamma_e = 0$  as

$$\omega_{pe} = \frac{c}{d} \sqrt{\frac{\mu_0}{L}}. \quad (2.34)$$

Here  $L = \mu_0/2\pi \ln[d^2/4r(d-r)]$  is the total per unit length inductance (self and mutual inductances),  $d$  the periodicity and  $r$  the radius of the wires.  $\epsilon_r^{\text{eff}}(\omega)$  is negative for  $\omega < \omega_{pe}$ . It is possible to replace the wires by planar strips of width  $c = r/4$ , without affecting the electromagnetic specifications. Losses ( $\Gamma_e \neq 0$ ) are introduced by changing the conductivity of the wires or by embedding them in a lossy background medium.

More freedom in design and control over  $\epsilon_r^{\text{eff}}(\omega)$  is obtained by introducing a cut in the wires, yielding the cut-wire (CW) medium which is shown in the middle of Fig. 2.9. The resulting gap capacitance  $C$  between two consecutive CWs, together with the inductance  $L$  of the wires, provides a Lorentz dispersive  $\epsilon_r^{\text{eff}}(\omega)$  near the resonance frequency  $\omega_{0e} \approx 1/\sqrt{LC}$ . Capacitively loaded strips (CLS) [129] are planar versions of CWs.

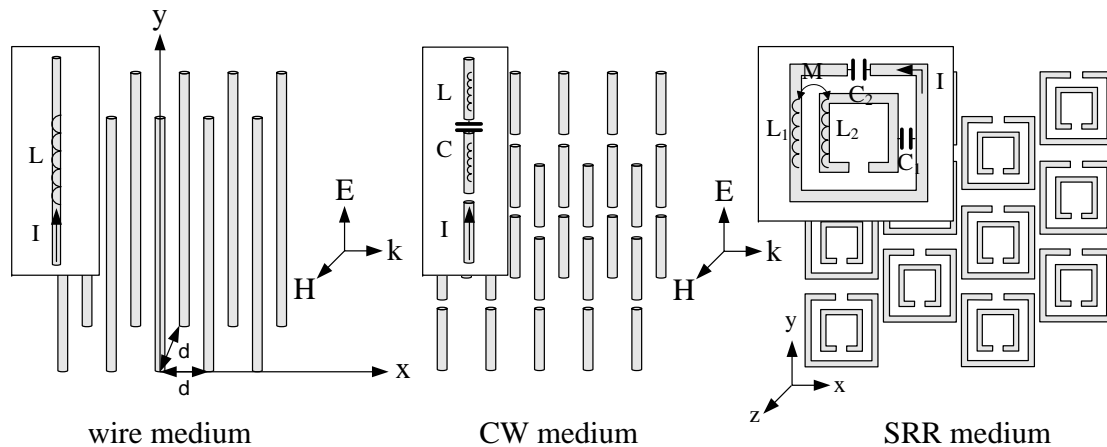


**Figure 2.9:** Various inclusion types (arranged in a periodic lattice) used in the realization of metamaterials. Insets show the equivalent circuit representation.

An array of split ring resonators (SRR), as shown on the right of Fig. 2.9, is commonly used to influence the magnetic polarizability of a medium. A single element consists of two concentric metallic rings each with a gap on opposite sides. According to Faraday's law, a time varying magnetic field polarized perpendicular to the plane of a SRR ( $z$  axis in Fig. 2.9) induces circulating currents in the metallic rings. The gap in each split ring acts thereby like a capacitor. Additional capacitance exists between the inner and outer split rings. The synthesized capacitance, together with the self and mutual inductances of the individual rings, makes the SRR resonate at  $\omega_{0m}$  [96]. The overall magnetic response is Lorentz dispersive (2.24). If the resonance is strong and the damping term  $\Gamma_m$  small, an array of SRRs yields  $\mu_r^{\text{eff}}(\omega) < 0$  slightly above  $\omega_{0m}$ . The overall size of a SRR is approximately  $\lambda/10$  at the operating wavelength  $\lambda$ . For closed and uninterrupted rings, on the other hand, a particle size of  $\lambda/4$  would be necessary to yield the same response. The electromagnetic response of a SRR is frequency scalable and can be adjusted by changing its physical dimensions. This property is analyzed in detail in Sec. 2.10.

It has to be mentioned that the SRR is a highly bianisotropic resonator. Depending on the symmetry and orientation with respect to the exciting field polarization it can exhibit an electric or magnetoelectric response. In order to avoid this, a mirror symmetry of the SRR with respect to the electric field polarization has to be provided. According to Fig. 2.9 this occurs for plane waves of the form  $(E_y, H_z, k_x)$ , in which case the resonator is excited solely by  $H_z$ . Polarizabilities of individual and coupled SRRs have been analyzed in [43; 44]. Numerous subwavelength resonators with capacitively loaded, spiral, multiple split and broad side coupled multilayer rings have been proposed on the basis of the SRR and have shown to yield improved performances [8; 14; 43; 80; 81].

Double negative metamaterials (DNG MTM) with  $\epsilon_r^{\text{eff}}(\omega) < 0$  and  $\mu_r^{\text{eff}}(\omega) < 0$  can be realized by a suitable combination of wire/CW and SRR arrays [87]. In order to prevent coupling, the wire/CW and SRR arrays should be placed sufficiently distant from each other [107]. Combining short wire segments with small loops together in



operation over a broader range of frequencies. Composite right-left-handed (CRLH) metamaterials [16] with combined right- and left-handed characteristics constitute a more general class of transmission line metamaterials (Sec. 2.5.3). Realizations of various CRLH transmission line metamaterials are shown in Fig. 2.10.

The metamaterial topologies mentioned up to now are anisotropic, showing their characteristic response for limited polarizations and incidence angles. For certain applications, on the other hand, fully 3D isotropic metamaterials are required. Following topologies can be used for a physical realization: a FDTD-derived structure proposed in [55] and [49], a structure derived from the rotated transmission line matrix scheme (Fig. 2.10(c)) [123; 124], a structure consisting of dielectric spheres [116], a 3D extension of the wire/split-ring approach [83], [67] and a straightforward extension of the 1D/2D CRLH structure [3; 4], which was the first 3D double negative metamaterial demonstrated experimentally.

## 2.8 Applications

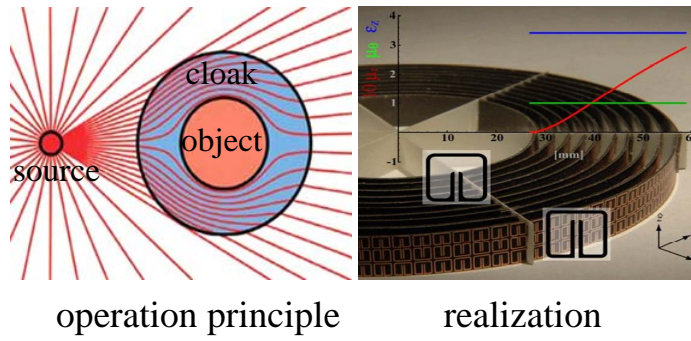
Recent research in the field of metamaterials has led to the realization of promising electromagnetic components. In the following some applications benefiting from the unique properties of microwave metamaterials are briefly reviewed.

Metamaterials are widely used in the design of subwavelength sized resonators and microwave filters with enhanced bandwidths and performances [45]. By a suitable combination of right- and left-handed transmission bands, CRLH transmission line metamaterials may be applied to construct zero phase delay lines to feed antenna arrays. Due to backward wave propagation in double negative metamaterials they have been employed in the realization of phase shifters [32]. Couplers that utilize a combination of regular microstrip and left-handed transmission lines have also been realized [58].

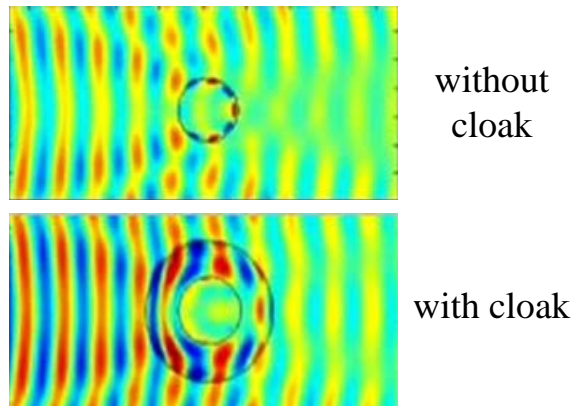
Potential benefits of using metamaterials in the field of antenna engineering include the improvement of directivity and bandwidth characteristics of conventional antennas [12]. Aside from enhanced device performance, miniaturization is a key issue in the design of antennas as a high integration density is becoming more and more important in modern communication technologies. Small and efficient patch antennas based on metamaterials have been designed. CRLH metamaterial inspired leaky wave antennas supporting backward waves and a continuous scan of the radiated beam from back- to end-fire have been realized [15; 75]. Metamaterial based artificial impedance surfaces (AIS) have been used as magnetic ground planes for wire antennas to achieve low profiles and to reduce unwanted interactions [35; 104].

The possibility of realizing sub-diffraction limited and aberration free planar superlenses from a slab of double negative material is another great potential application area of metamaterials. Various types of metamaterial superlenses with near- and far-field imaging characteristics and hyperlenses transforming evanescent waves into propagating ones have been realized. A review of various metamaterial superlenses is given in [127]. The concept of metamaterial superlenses will be analyzed in detail in Chapter 3.

## 2. CONCEPT OF METAMATERIALS



(a)



(b)

**Figure 2.11:** (a) Operation principle and realization of a 2D cylindrical metamaterial cloak with (b) plane wave scattering, taken from [98].

Among the most striking features of metamaterials is their use in cloaking and scattering reduction. In recent years, metamaterial technology has led to the realization of novel cloaking devices. The method of transformation optics [73; 91] has shown that cloaking requires a material with inhomogeneous (spatially varying) and independently controllable material properties  $\epsilon_r^{\text{eff}}$  and  $\mu_r^{\text{eff}}$ , making metamaterials highly suitable. A 2D cloak composed of concentric metallic shells consisting of horseshoe shaped metallic resonators, as shown in Fig. 2.11(a), has been developed to render an object invisible in a narrow band of microwave frequencies [98]. The metamaterial cloak can guide electromagnetic waves around the object to be cloaked without any scattering. In other words, a wave impinging on the cloak propagates around it without being scattered and emerges on the other side with the same phase as it would have propagated through vacuum. In this way the cloak casts no shadow (Fig. 2.11(b)) and makes the object inside it virtually invisible. A transmission line cloak composed of periodically stacked cylindrical transmission line networks has been studied and verified experimentally in [1; 2]. Recently, a 3D cloak operating at optical

wavelengths has been designed and realized [36].

Another effective way of reducing scattering from relevant targets is achieved through the application of absorbers. Metamaterials have been used in the design of electrically thin microwave absorbers [33; 114]. A microwave absorber based on SRR inclusions has been reported in [11]. The concept of Drude and Lorentz dispersive metamaterial absorbers will be discussed in detail in Chapter 4.

A completely different approach to reduction of scattering is based on the scattering cancellation technique, where the object to be cloaked and the cloak are characterized by opposite local polarizabilities and the overall polarizability is made sufficiently small [6]. Possibilities of reducing total scattering cross sections of spherical and cylindrical dielectric/conducting scatterers using metamaterial covers have been investigated theoretically in [5]. A major drawback of this method is that the required coating depends strongly on the shape of the object to be cloaked and works only for electrically small objects.

In Summary, metamaterials enable the realization of electromagnetic devices with unprecedented performances and functionalities. Metamaterials can be designed over a large portion of the electromagnetic spectrum by simply scaling the dimensions of a unit cell and its constituent inclusions. Due to recent advancements in nanofabrication technology, the interest in their realization has shifted towards THz frequencies. The THz regime of the electromagnetic spectrum extends from 100 GHz to 10 THz, where 1 THz corresponds to a wavelength of  $300 \mu\text{m}$ . For THz metamaterials the unit cell is few tens of microns and contains critical feature sizes of a few microns. Considerable progress has been made in design, fabrication, and characterization of metamaterials at THz frequencies [113].

## 2.9 Homogenization Methods

Assigning effective material parameters to composite electromagnetic materials composed of two or more materials with significantly different physical/chemical properties has always been an important issue. Well known methods are the Clausius Mossotti and Maxwell Garnett mixing formulas [114]. In this section, several methods that have been proposed in the past for the homogenization of metamaterials are briefly reviewed.

The most common approach is based on the Nicholson-Ross-Weir method [86; 118]. The measured or simulated scattering parameters of a finite thickness metamaterial slab are thereby related to the Fresnel reflection and transmission coefficients (App. A) of a homogeneous slab with  $\epsilon_r^{\text{eff}}$  and  $\mu_r^{\text{eff}}$ . For normal incidence (TEM wave), the method was applied to extract effective material parameters of wire and SRR metamaterials [111]. The method has been extended to work for oblique incidence [82], bianisotropic [68; 74] and chiral [92] metamaterials.

A major problem is thereby that the resonant behavior of one of the retrieved material parameters is accompanied by an antiresonant behavior of the other [66]. This violates physical laws and contradicts with principles of causality (passivity).

## 2. CONCEPT OF METAMATERIALS

---

Parameter fitting of dispersive models (PFDM) [76] is a similar technique by which this unphysical artifact can be overcome. If the dispersive behavior of the metamaterial is known a priori, for example to be Drude and/or Lorentz dispersive, the model parameters  $\omega_p$ ,  $\omega_0$ ,  $\Gamma$  (Sec. 2.6) are then optimized to fit the measured or simulated scattering parameters. Although restricted to an initial knowledge of the dispersive behaviour, PFDM provides an efficient way to extract  $\epsilon_r^{\text{eff}}$  and  $\mu_r^{\text{eff}}$  of various metamaterials. The method is employed in the following section to assign effective material parameters to metamaterials composed of conducting strip, CLS and SRR inclusions.

Another widespread homogenization method is based on field averaging [109], where local fields that vary throughout a unit cell are replaced by a discrete set of averaged ones. Thereby  $\mathbf{E}$ ,  $\mathbf{H}$ ,  $\mathbf{D}$  and  $\mathbf{B}$  are averaged over specific lines and surfaces of a unit cell. Effective material parameters are determined by plugging these averages into (2.1)-(2.2) and solving for  $\epsilon_r^{\text{eff}}$  and  $\mu_r^{\text{eff}}$ . In order to obtain accurate and reasonable results, the surfaces and contours used in the averaging process have to be determined carefully [109].

### 2.10 Effective Parameter Extraction

The parameter fitting of dispersive models (PFDM) method [76] is employed throughout this section to extract effective material parameters of metamaterials composed of metallic strip, capacitively loaded strip (CLS) and split ring resonator (SRR) inclusions. Simulated reflection  $R^{\text{sim}}$  and transmission  $T^{\text{sim}}$  coefficients from a finite thickness metamaterial slab are thereby related to the Fresnel reflection  $R^{\text{eff}}$  and transmission  $T^{\text{eff}}$  coefficients of a homogenized slab with Lorentz and Drude dispersive  $\epsilon_r^{\text{eff}}(\omega)$  or  $\mu_r^{\text{eff}}(\omega)$  (Sec. 2.6). The corresponding dispersion model parameters  $\omega_p$ ,  $\omega_0$  and  $\Gamma$  are then optimized to obtain the best fit to  $R^{\text{sim}}$  and  $T^{\text{sim}}$ . The goal function

$$\mathbf{G} = \sum_n \|R^{\text{sim}} - R^{\text{eff}}\|_{\nu_n} + \sum_n \|T^{\text{sim}} - T^{\text{eff}}\|_{\nu_n}$$

is minimized at  $n$  frequencies  $\nu_n$  in the frequency range of interest.

In order to determine  $R^{\text{sim}}$  and  $T^{\text{sim}}$ , full-wave simulations are carried out with HFSS<sup>®</sup> [7]. The simulation volume consisting of a single unit cell of thickness  $d$  is shown in Fig. 2.12. A two-port waveguide with pairs of PEC and PMC boundaries permits thereby the simulation of an infinite slab in the  $xy$  plane. TEM waves with  $E_x$ ,  $H_y$ ,  $k_z$  are launched from each waveport with characteristic impedances equal to that of free space and the reflection  $R^{\text{sim}}$  and transmission  $T^{\text{sim}}$  responses are evaluated. To ensure that the metamaterial slab is excited in its fundamental electric and magnetic modes, the strip or CLS is positioned perpendicular to the PEC walls and the SRR parallel to the PMC walls. The inclusions are modeled by 35  $\mu\text{m}$  thick copper and are immersed in a dielectric host with permittivity  $\epsilon_r^h$  and loss tangent  $\tan \delta$ . Unless otherwise indicated, the host material is assumed to be standard FR4 with  $\epsilon_r^h = 4.4$  and  $\tan \delta = 0.02$ .

The strip-SRR or CLS-SRR metamaterial unit cell compositions investigated in

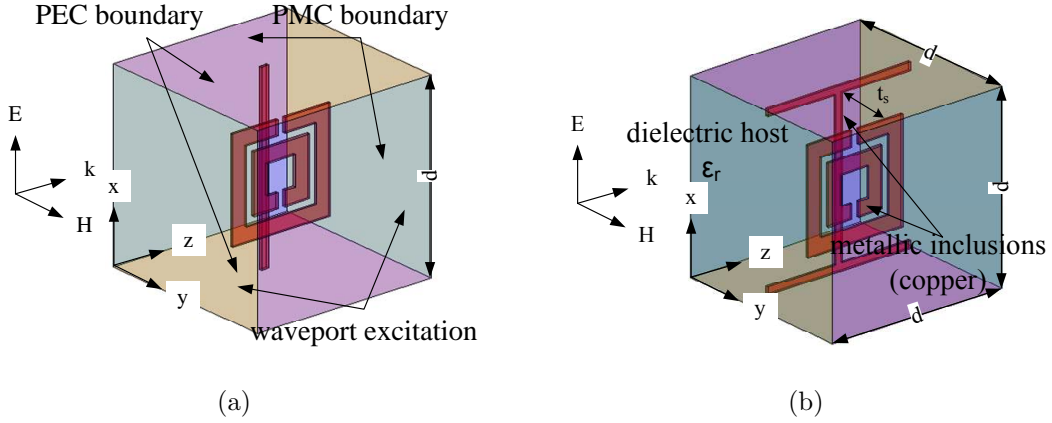


**Figure 2.12:** Simulation volume consisting of a unit cell, (a) strip-SRR and (b) CLS-SRR metamaterial.

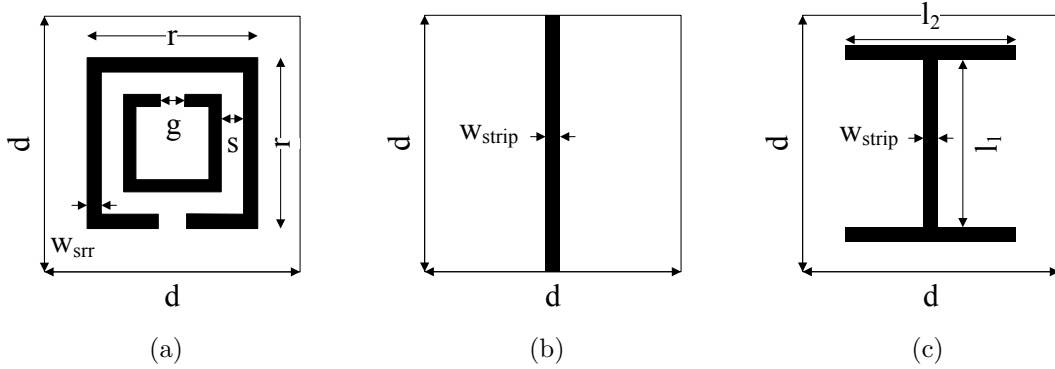


**Figure 2.13:** Physical dimensions of (a) SRR (b) strip and (c) CLS inclusion.

this section are tuned to operate at X- and Ku-band frequencies, ranging from 8 to 18 GHz. Together with the extracted effective material parameters they will be employed in Sec. 4.1 in the realization of planar and electrically thin Drude and Lorentz dispersive metamaterial absorbers. Since metamaterials are frequency scalable, operation in different frequency bands can be obtained by scaling the unit cell and inclusion dimensions.

### 2.10.1 Strip-SRR Metamaterials

For metamaterials composed of metallic strip and SRR inclusions it is known that  $\epsilon_r^{\text{eff}}(\omega)$  and  $\mu_r^{\text{eff}}(\omega)$  are Drude (2.25) and Lorentz (2.24) dispersive, respectively. Parameters to optimize are therefore  $\epsilon_r(\infty)$ ,  $\mu_r(\infty)$ ,  $\omega_{pe} = 2\pi\nu_{pe}$ ,  $\omega_{pm} = 2\pi\nu_{pm}$ ,  $\omega_{0m} = 2\pi\nu_{0m}$ ,  $\Gamma_e$  and  $\Gamma_m$ . These parameters depend strongly on the unit cell size  $d$ , permittivity of the host material  $\epsilon_r^h$  and inclusion size. As shown in Fig. 2.13(a)-(b), the physical dimensions of strip and SRR inclusions are given by:

- $r$  : outer edge length of SRR
- $s$  : gap between inner and outer rings

## 2. CONCEPT OF METAMATERIALS

---

- $g$  : split width in individual rings
- $w_{srr}$  : strip width of SRR
- $t_s$  : separation between inclusions
- $w_{strip}$  : width of strips

The frequency dependent magnitude and phase of R and T for a strip-SRR metamaterial with specifications given in Tab. 2.2 is plotted in Fig. 2.14.  $R^{\text{sim}}$  and  $T^{\text{sim}}$  are plotted by dotted lines,  $R^{\text{eff}}$  and  $T^{\text{eff}}$  are plotted by solid lines. The corresponding extracted material parameters and refractive index of the homogenized slab are plotted in Fig. 2.15.

From the characteristics of  $\mu_r^{\text{eff}}(\omega)$ , it is observed that the SRR resonates at  $\nu_{0m} = 8.7$  GHz. The real part of the permeability becomes negative for frequencies above  $\nu_{0m}$ , i.e  $\text{Re}\{\mu_r^{\text{eff}}\} < 0$ . Furthermore, due to the strips,  $\text{Re}\{\epsilon_r^{\text{eff}}\} < 0$  for frequencies approximately below 10 GHz. This yields  $\text{Re}\{n^{\text{eff}}\} < 0$  in the frequency range between 9 and 10 GHz.

Based on the configuration in Tab. 2.2, the influence of variations in  $d$ ,  $r$ ,  $s$ ,  $g$ ,  $w_{srr}$ ,  $t_s$ ,  $w_{strip}$ ,  $\epsilon_r^h$  on  $\omega_{pe,pm}$ ,  $\omega_{0m}$ ,  $\Gamma_{e,m}$  is investigated next. Primary focus is thereby on variations in  $\omega_{pe}$  and  $\omega_{0m}$ . A single parameter is changed while all others are held fixed. Results are discussed in the following and summarized in Tab. 2.3 and Tab. 2.4.

- **Unit cell size** [ $d$ ]:

According to (2.34),  $\nu_{pe}$  is inversely proportional to the periodicity  $d$  and increasing  $d$  shifts  $\nu_{pe}$  to lower frequencies. To demonstrate this,  $d$  is increased from 2.50 to 3.00 mm. A downward shift of  $\nu_{pe}$  from 26.9 to 21.5 GHz with  $\Delta\nu_{pe} = -5.4$  GHz is thereby observed. Although there is a small variation in  $\nu_{pm}$ , the magnetic response due to the SRR is almost unaffected.

- **Strip width** [ $w_{strip}$ ]:

Another way to shift  $\nu_{pe}$  to lower frequencies is achieved by making the strips thinner. The inductance of an array of conducting strips is inversely proportional to  $\nu_{pe}$  and increases with decreasing  $w_{strip}$ . A change in  $w_{strip}$  from 1 to 0.1 mm yields a linear downward shift of  $\nu_{pe}$  from 43.5 to 26.9 GHz. The change in  $\nu_{pm}$  is negligibly small.

- **Distance between strip and SRR** [ $t_s$ ]:

In order to prevent magnetoelectric coupling, the strip-SRR metamaterial is investigated in its most symmetric form (Sec. 2.7). However, it is obvious that the presence of SRRs will influence  $\epsilon_r^{\text{eff}}(\omega)$  and the presence of strips will influence  $\mu_r^{\text{eff}}(\omega)$ . In order to investigate this phenomenon, the distance between the inclusions is varied between  $t_s = 0.25$  and  $t_s = 1.5$  mm. A significant change in  $\epsilon_r(\infty)$  and  $\nu_{pe}$  occurs. On the other hand, the magnetic response due to SRRs changes only slightly. It can be concluded that the distance between the strip and SRR arrays has a significant influence on  $\epsilon_r^{\text{eff}}(\omega)$ . An independent modeling of SRR and strip media can therefore lead to incorrect results.

## 2.10 Effective Parameter Extraction

(mm)									(GHz)				
$d$	$r$	$s$	$g$	$t_s$	$w_{srr}$	$w_{strip}$	$\epsilon_r(\infty)$	$ \mu_r(\infty) $	$\nu_{pe}$	$\Gamma_e$	$\nu_{pm}$	$\nu_{0m}$	$\Gamma_m$
2.50	1.80	0.10	0.10	0.25	0.20	0.10	6.7	1.0	27.4	1.6	4.1	8.7	1.7

**Table 2.2:** Physical dimensions of unit cell/inclusions and extracted parameters of a strip-SRR metamaterial with host permittivity  $\epsilon_r^h = 4.4$  and loss tangent  $\tan \delta = 0.02$ .

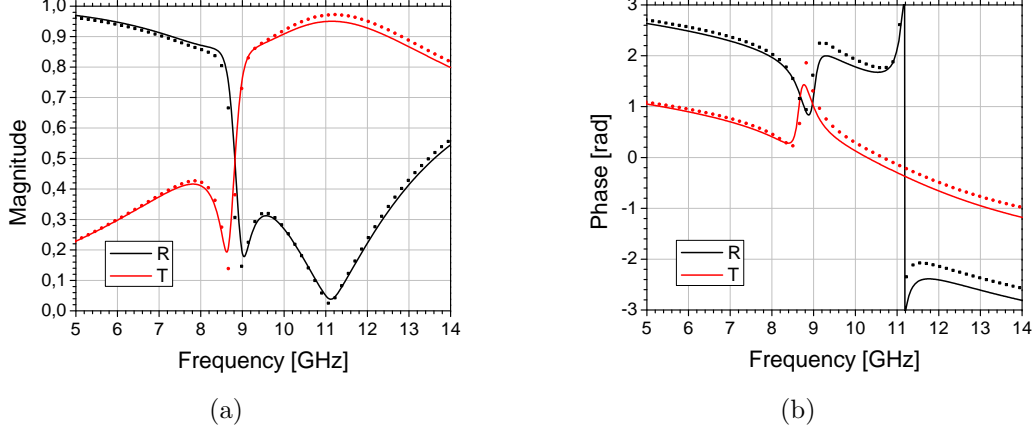


**Figure 2.14:** (a) Magnitude and (b) phase of R and T for the strip-SRR metamaterial in Tab. 2.2.  $R^{\text{eff}}$ ,  $T^{\text{eff}}$  (solid line) and  $R^{\text{sim}}$ ,  $T^{\text{sim}}$  (dotted line).

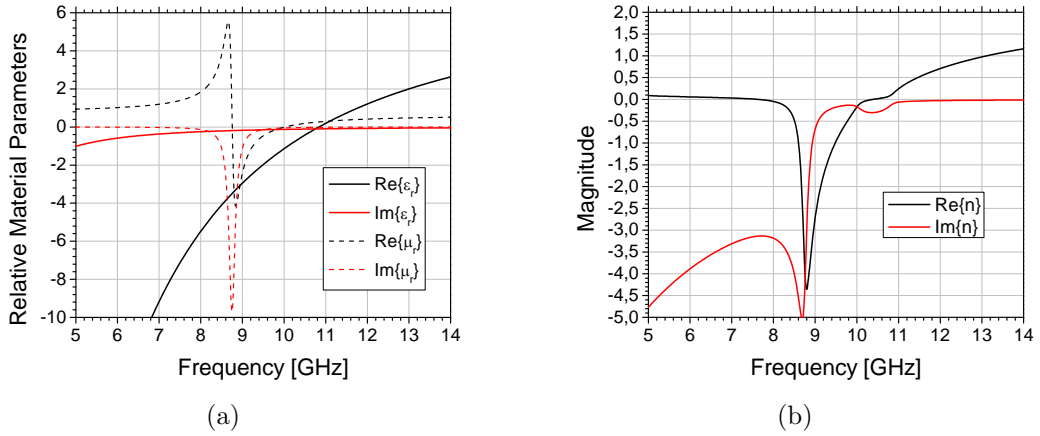


**Figure 2.15:** Extracted (a)  $\epsilon_r^{\text{eff}}(\omega)$  and  $\mu_r^{\text{eff}}(\omega)$  and (b)  $n^{\text{eff}}$  for the strip-SRR metamaterial given in Tab. 2.2.

### • Permittivity of host material $[\epsilon_r^h]$ :

It is expected that  $\epsilon_r^h$  has a significant influence on  $\epsilon_r^{\text{eff}}(\omega)$  and  $\mu_r^{\text{eff}}(\omega)$ . As shown in Tab. 2.3, three different host materials with vacuum ( $\epsilon_r^h = 1$ ,  $\tan \delta = 0$ ), Rogers RT Duroid ( $\epsilon_r^h = 2.2$ ,  $\tan \delta = 0.009$ ) and standard FR4 ( $\epsilon_r^h = 4.4$ ,  $\tan \delta = 0.02$ ) have been considered. The loss tangent is given by  $\tan \delta = \epsilon_r^{h''}/\epsilon_r^{h'}$ . Physical dimensions of the investigated metamaterial are the same as those in Tab. 2.2. It is reasonable to expect that  $\epsilon_r(\infty)$  increases with increasing  $\epsilon_r^h$ . As indicated by (2.34),  $\epsilon_r^h$  should have no influence on  $\nu_{pe}$ . This is validated by the results shown in Tab. 2.3, where

## 2. CONCEPT OF METAMATERIALS

---

$\nu_{pe}$  changes only slightly. On the other hand, a significant change in  $\mu_r^{\text{eff}}(\omega)$  takes place. Based on the equivalent LC circuit representation of SRRs [96], increasing  $\epsilon_r^h$  increases the gap capacitances leading to lower  $\nu_{0m}$  and  $\nu_{pm}$ .

- **Outer edge length of a SRR [ $r$ ]:**

The effective area of a SRR grows as  $r$  gets larger. As a result of the increasing overall inductance and capacitance, it is expected that  $\nu_{0m}$  shifts to lower frequencies. A change of the outer edge length from  $r = 1.4$  to  $r = 1.8$  mm shifts  $\nu_{0m}$  downwards from 13.2 to 8.7 GHz. The influence of  $r$  on  $\epsilon_r^{\text{eff}}(\omega)$  can be seen from the variations in  $\epsilon_r(\infty)$  and  $\nu_{pe}$ .

- **Split width of SRR [ $s$ ]:**

Enlarging the gap between inner and outer split rings yields a smaller inner split ring. On the basis of the decreasing capacitance between inner and outer rings,  $\nu_{0m}$  shifts to higher frequencies. A change of  $\Delta s = 0.1$  mm, for example, yields  $\Delta\nu_{0m} = 0.6$  GHz.

- **Gap in individual split ring [ $g$ ]:**

The gaps in individual split rings act like parallel plate capacitors whose capacitances vary according to  $C = \epsilon_r^h A/g$  where  $A = w_{srr}t$  is the effective area at the strip ends, with  $t$  the thickness of the strips. Due to the fact that  $\omega_{0m} \approx 1/\sqrt{LC}$ , an enlargement of the gap from  $g = 0.1$  mm to  $g = 0.3$  mm increases  $\nu_{0m}$  by 0.9 GHz.

- **Strip width of SRR [ $w_{srr}$ ]:**

A change in  $w_{srr}$  affects primarily  $\nu_{0m}$ . An increase of  $w_{srr}$  from 0.1 to 0.2 mm decreases the overall mutual inductance and capacitance of a SRR, yielding a significant upward shift of  $\nu_{0m}$  from 10.8 to 13.2 GHz.

### 2.10.2 CLS-SRR Metamaterials

More freedom in design and control over  $\epsilon_r^{\text{eff}}(\omega)$  is obtained by replacing the strips with capacitively loaded strips (CLS) (Fig. 2.13(c)). The resulting gap capacitance  $C_g$  between adjacent CLSs produces a Lorentz dispersive  $\epsilon_r^{\text{eff}}(\omega)$  near  $\omega_0 \approx 1/\sqrt{LC_g}$ . As opposed to strip-SRR metamaterials, since  $\epsilon_r^{\text{eff}}(\omega)$  is now also given by Lorentz dispersion,  $\omega_{0e} = 2\pi\nu_{0e}$  has to be optimized additionally. Its value is adjusted to the desired frequency by varying the longitudinal  $l_1$  and lateral  $l_2$  armlengths of an individual CLS.

The optimized model parameters for various physical compositions are listed in Tab. 2.5. All parameters except  $l_1$  and  $l_2$  are held constant at  $w_{strip} = 0.1$  mm,  $d = 3$  mm,  $t_s = 0.25$  mm,  $w_{srr} = 0.2$  mm,  $r = 1.4$  mm,  $g = 0.1$  mm,  $s = 0.1$  mm and  $\epsilon_r^h = 4.4 - j0.088$ .

The frequency dependent magnitude and phase of R and T for the IVth configuration in Tab. 2.5 is plotted in Fig. 2.16. The corresponding effective material parameters and refractive index of the homogenized slab are plotted in Fig. 2.17.

The gap between two consecutive lateral arms can be regarded as a parallel plate capacitor whose effective area increases as  $l_2$  increases. This leads to an enhancement of  $C_g$ . Another way of increasing the gap capacitance is achieved by making the gap smaller. This is obtained by increasing  $l_1$ . Based on the fact that  $\nu_{0e}$  is inversely proportional to  $C_g$ ,  $\nu_{0e}$  shifts to lower frequencies as  $l_1$  and  $l_2$  increase. Changing  $l_1$  by  $\Delta l_1 = 0.4$  mm (rows II and IV in Tab. 2.5), yields a downward shift of  $\nu_{0e}$  by 3.6 GHz. On the other hand,  $l_2$  has a less significant effect on  $\nu_{0e}$ . As seen from rows III to V in Tab. 2.5, increasing  $l_2$  from 2.0 to 2.8 mm yields  $\Delta\nu_{0e} = -1.9$  GHz.

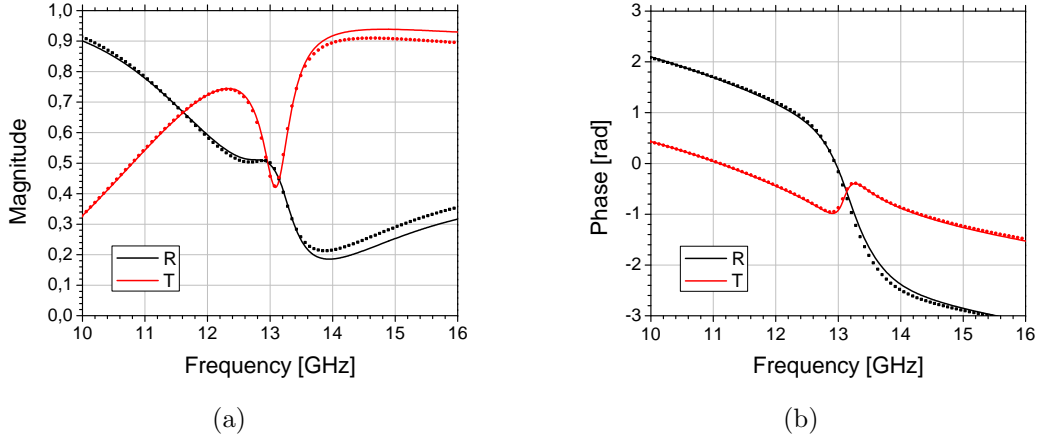


**Figure 2.16:** (a) Magnitude and (b) phase of R and T for the CLS-SRR metamaterial with parameters as in row IV of Tab. 2.5.  $R^{\text{eff}}$ ,  $T^{\text{eff}}$  (solid line) and  $R^{\text{sim}}$ ,  $T^{\text{sim}}$  (dotted line).

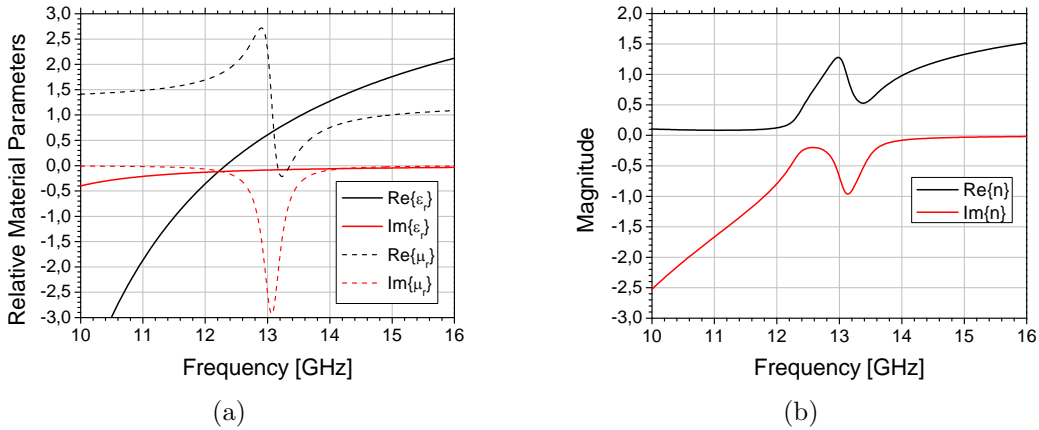


**Figure 2.17:** Extracted (a)  $\epsilon_r^{\text{eff}}(\omega)$  and  $\mu_r^{\text{eff}}(\omega)$  and (b)  $n^{\text{eff}}$  for the CLS-SRR metamaterial given in row IV of Tab. 2.5.

## 2. CONCEPT OF METAMATERIALS

Host Permittivity		(GHz)					
$\epsilon_r^h$	$\tan \delta$	$\epsilon_r(\infty) \mu_r(\infty)$	$\nu_{pe}$	$\Gamma_e$	$\nu_{pm}$	$\nu_{p0}$	$\Gamma_m$
1.0	0.000	1.5 0.9	27.1	1.9	8.3	18.3	1.0
2.2	0.009	3.4 0.9	27.6	0.6	5.8	12.3	1.1
4.4	0.020	6.7 1.0	27.4	1.6	4.1	8.7	1.7

**Table 2.3:** Effect of host permittivity  $\epsilon_r^h$  (strip-SRR metamaterial).

(mm)							(GHz)					
$d$	$r$	$s$	$g$	$t_s$	$w_{srr}$	$w_{strip}$	$\epsilon_r(\infty) \mu_r(\infty)$	$\nu_{pe}$	$\Gamma_e$	$\nu_{pm}$	$\nu_{0m}$	$\Gamma_m$
2.50	1.40	0.10	0.10	0.25	0.20	0.10	4.8 1.0	26.9	1.3	4.1	13.2	2.2
3.00	1.40	0.10	0.10	0.25	0.20	0.10	4.3 1.1	21.5	1.0	3.5	13.2	2.2
2.50	1.40	0.10	0.10	0.25	0.20	0.10	4.8 1.0	26.9	1.3	4.1	13.2	2.2
2.50	1.80	0.10	0.10	0.25	0.20	0.10	6.7 1.0	27.4	1.6	4.1	8.7	1.7
2.50	1.40	0.10	0.10	0.25	0.20	0.10	4.8 1.0	26.9	1.3	4.1	13.2	2.2
2.50	1.40	0.10	0.10	0.25	0.20	0.10	4.8 0.9	26.9	1.2	4.5	13.8	2.2
2.50	1.40	0.10	0.10	0.25	0.20	0.10	4.8 1.0	26.9	1.3	4.1	13.2	2.2
2.50	1.40	0.10	0.10	0.25	0.20	0.10	4.7 1.0	26.8	1.1	4.5	14.2	2.3
2.50	1.80	0.10	0.10	0.25	0.20	0.10	6.7 1.0	27.4	1.6	4.1	8.7	1.7
2.50	1.80	0.10	0.10	0.25	0.20	0.10	7.3 1.0	26.7	1.4	3.9	8.7	1.5
2.50	1.80	0.10	0.10	0.25	0.20	0.10	7.5 0.9	25.8	1.3	3.7	8.6	1.4
2.50	1.40	0.10	0.10	0.25	0.20	0.10	4.9 0.9	26.9	1.3	3.6	10.8	1.6
2.50	1.40	0.10	0.10	0.25	0.20	0.10	4.8 1.0	26.9	1.3	4.1	13.2	2.2
2.50	1.40	0.10	0.10	0.25	0.20	0.10	4.8 1.0	26.9	1.3	4.1	13.2	2.2
2.50	1.40	0.10	0.10	0.25	0.20	0.10	4.7 1.0	29.5	1.6	4.2	13.2	2.0
2.50	1.40	0.10	0.10	0.25	0.20	0.10	4.7 1.2	33.3	1.4	4.3	13.3	1.9
2.50	1.40	0.10	0.10	0.25	0.20	0.10	4.5 1.1	36.3	0.5	4.5	13.4	2.8
2.50	1.40	0.10	0.10	0.25	0.20	0.10	4.5 1.2	39.5	0.5	4.5	13.5	3.0
2.50	1.40	0.10	0.10	0.25	0.20	0.10	4.6 1.2	43.5	0.1	4.3	13.7	3.0

**Table 2.4:** Effect of physical dimensions on the extracted model parameters of a strip-SRR metamaterial.

	(mm)		(GHz)							
	$l_1$	$l_2$	$\epsilon_r(\infty) \mu_r(\infty)$	$\nu_{pe}$	$\nu_{pm}$	$\nu_{0e}$	$\nu_{0m}$	$\Gamma_e$	$\Gamma_m$	
I	2.3	2.3	4.0 1.5	18.2	3.9	10.9	13.3	1.4	1.8	
II	2.3	2.6	4.0 1.4	17.2	4.1	10.8	13.2	1.1	1.8	
III	2.7	2.0	3.9 1.3	19.3	3.9	8.9	13.3	1.3	2.1	
IV	2.7	2.6	4.2 1.2	20.3	3.5	7.2	13.1	1.4	2.1	
V	2.7	2.8	4.1 1.2	20.4	3.6	7.0	13.2	1.2	1.9	

**Table 2.5:** Effect of physical dimensions on the extracted model parameters of a CLS-SRR metamaterial.

# 3

## Metamaterial Superlens

One of the most intriguing potential applications of metamaterials is the possibility of creating a superlens from a planar slab of double negative material, whose resolution is not subject to the traditional diffraction limit of a wavelength. A planar double negative metamaterial slab with  $\epsilon_r = \mu_r = -1$  and surrounded by vacuum acts as a collimating lens [117]. Theoretically a metamaterial superlens offers imaging with infinite resolution [88].

However, realistic metamaterials have unavoidable disadvantages of loss and narrow bandwidth, restricting their application. The superlens is therefore an idealization which is difficult to realize in reality. Dispersion, losses and finite size of unit cells in realistic metamaterials degrade the image quality [28; 53; 71; 78; 84; 102; 110]. However, nearly-perfect lenses with subwavelength imaging capabilities were reported and experimentally verified; using structures based on wire-SRR metamaterials [41; 69; 119] as well as on transmission line implementations of metamaterials [3; 48; 59; 61].

The imaging characteristics of a double negative metamaterial slab have been considered up to now mainly in two dimensions in combination with a line source and in three dimensions with a dipole oriented perpendicular to the surface of the slab. In those cases only one type of modes is involved in the analysis, which depending on the type of excitation can be either TE or TM. On the other hand, a dipole oriented parallel to the interface of the slab excites both type of modes simultaneously. TE and TM modes are transmitted unequally if either  $\epsilon_r$  or  $\mu_r$  or both are perturbed from the ideal case with  $\epsilon_r = \mu_r = -1$ .

In this chapter, imaging by realistic double negative metamaterial slabs with  $\epsilon_r \neq -1$  and/or  $\mu_r \neq -1$  is considered. The slab is thereby excited by arbitrarily oriented electric or magnetic dipoles. A new type of image distortion, the unequal transmission of TE and TM portions of the fields, is identified and studied. A tool for evaluating the field intensities in the vicinity of the image plane is developed for this purpose. The fields are represented in the spectral domain as two dimensional Fourier integrals [39] and numerically evaluated.

Furthermore, the transverse extension or aperture size of the slab restrict its imaging capabilities. In theoretical investigations this is not considered and the slab is assumed to extend to infinity in the transversal plane. Based on full-wave transmission line matrix (TLM) simulations of an ideal but transversely limited double

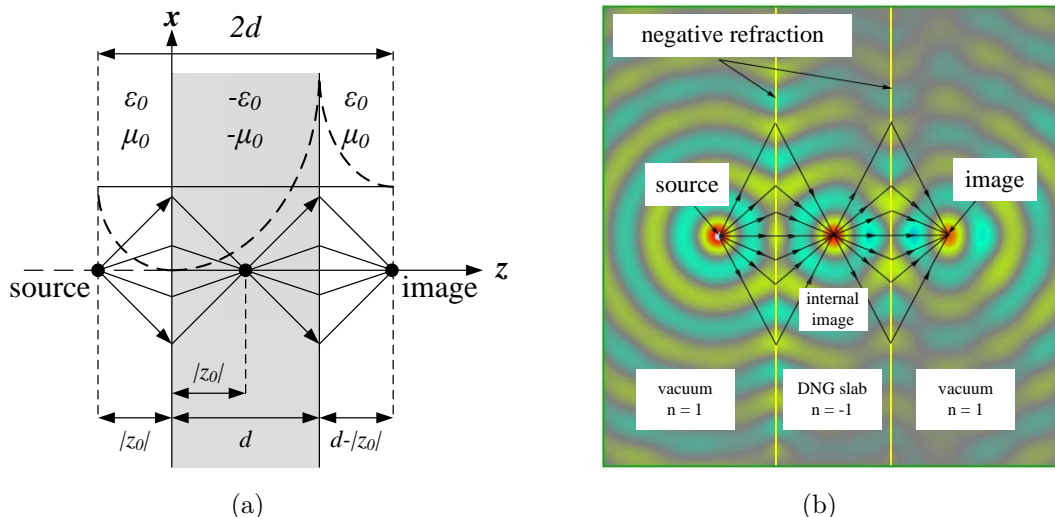


**Figure 3.1:** (a) Focusing of propagating modes (solid lines) and recovery of evanescent modes (dashed line) by a double negative metamaterial slab perfectly matched to vacuum, (b) MEFiSTo-3D Pro<sup>®</sup> simulation showing a snapshot of the electric field distribution.

negative metamaterial slab, the influence of a finite aperture on the image quality is investigated.

Finally, imaging of broadband pulses with a Gaussian spectrum are studied. A Drude dispersive CRLH slab is thereby considered. Simulations are carried out with MEFiSTo-3D Pro<sup>®</sup> [38], where double negative metamaterials are modeled by matching an inter cell network to a standard 3D symmetrical condensed node [112]. The modified TLM scheme yields a general framework for the modeling of CRLH metamaterials [54; 63].

### 3.1 Physical Background

As shown in Fig. 3.1, a slab with finite thickness  $d$ , surrounded by vacuum ( $\epsilon_0, \mu_0$ ) and material parameters  $\epsilon = -\epsilon_0, \mu = -\mu_0$  focuses waves emitted from a point source located at  $z = -|z_0|$  in front of the slab to a point located at  $z = 2d - |z_0|$  behind the slab. In the spectral domain, the source field can be expressed as a two dimensional Fourier integral

$$E(x, y, z) = \int_{-\infty}^{\infty} \int_{-\infty}^{\infty} E(k_x, k_y) e^{-jk_x x - jk_y y - jk_z z} dk_x dk_y, \quad (3.1)$$

corresponding to a sum of propagating and evanescent plane waves subject to the dispersion relation  $k_x^2 + k_y^2 + k_z^2 = k_0^2$  [79].

The wave vector along the optical axis of the slab ( $z$  axis) is given by  $k_z = \sqrt{k_0^2 - k_x^2 - k_y^2}$ . Near field modes with  $|k_x|$  and  $|k_y| > k_0$  decay exponentially away from the source and are evanescent. They are not detected by conventional imaging

systems. Even for the best manufactured lens the resolution is determined by the propagating part of the spectrum with  $|k_x|$  and  $|k_y| \leq k_0$ , leading to a truncation of the integral at approximately  $\pm k_0$  and a loss of subwavelength features.

A metamaterial slab with  $\epsilon = -\epsilon_0$  and  $\mu = -\mu_0$ , on the other hand, is capable of exponentially increasing the amplitude of the evanescent modes at the same rate they decay in free space [88]. This property is shown by the dashed line in Fig. 3.1(a) and will become clear in the following sections. Furthermore, from the viewpoint of geometrical optics, the angle of refraction at the slab interface is equal to the negative angle of incidence, so that propagating modes are focused inside the slab at  $z = |z_0|$  and refocused outside it at  $z = 2d - |z_0|$ . The phase advance inside the slab is negative (Sec. 2.4 and 2.5) and is exactly compensated by the phase advance outside it when the distance between the source and image planes is  $2d$ . Both magnitude and phase of the source field are therefore perfectly restored at the image plane.

In summary, the metamaterial slab acts as a perfect lens and translates the complete field distribution from the source plane to the image plane.

It has to be mentioned that for slabs surrounded by a medium other than vacuum, the permittivity and permeability in the slab need to be adjusted such that they are equal and opposite to those of the surrounding medium. This ensures that the slab impedance is perfectly matched to the surrounding medium and that the refractive indices of the slab and the surrounding medium are equal and opposite.

## 3.2 Analytical Formulation

A double negative metamaterial slab of thickness  $d$ , refractive index  $n_2 = \sqrt{\epsilon_{2r}\mu_{2r}}$  ( $\text{Re}\{n_2\} < 0$ ) and intrinsic impedance  $\eta_2 = \sqrt{\mu_{2r}/\epsilon_{2r}\eta_0}$  is immersed in a positive refractive index medium with  $n_1 = \sqrt{\epsilon_{1r}\mu_{1r}}$  and  $\eta_1 = \sqrt{\mu_{1r}/\epsilon_{1r}\eta_0}$ . The setup is shown in Fig. 3.2. Since the configuration is unbounded in the transversal direction, circular-cylindrical coordinates  $(\rho, z)$  with  $\rho = \sqrt{x^2 + y^2}$  and  $\hat{\boldsymbol{\rho}} = \hat{\mathbf{x}} \cos \varphi + \hat{\mathbf{y}} \sin \varphi$  are used.

A Hertzian dipole is placed on the  $z$ -axis at  $z' = z_0 < 0$  and  $\rho' = 0$ . Remember from the previous section that the ideal imaging condition is satisfied only if  $\epsilon_{2r} = -\epsilon_{1r}$  and  $\mu_{2r} = -\mu_{1r}$ , in which case the image plane is located at  $z = 2d - |z_0|$ .

For homogeneous slabs of infinite extent, exact modal Green's function solutions for TE and TM fields are available [39; 57]. The time-harmonic electromagnetic fields excited by an electric dipole  $\mathbf{J}(\mathbf{r}, t) = \mathbf{J}_0 \delta(\mathbf{r} - \mathbf{r}') e^{j\omega t}$  or magnetic dipole  $\mathbf{M}(\mathbf{r}, t) = \mathbf{M}_0 \delta(\mathbf{r} - \mathbf{r}') e^{j\omega t}$  are defined in terms of the electric  $\Pi_e(\mathbf{r}, \mathbf{r}')$  and magnetic  $\Pi_m(\mathbf{r}, \mathbf{r}')$  Hertz potentials. Here  $\mathbf{r}'$  and  $\mathbf{r}$  represent the position vectors of the source and observation point, respectively. For  $\mathbf{r} \neq \mathbf{r}'$  the fields are given by

$$\begin{aligned} \mathbf{E}(\mathbf{r}, \mathbf{r}') &= \nabla \times \nabla \times \hat{\mathbf{z}} \Pi_e(\mathbf{r}, \mathbf{r}') - j\omega \mu_r \mu_0 \nabla \times \hat{\mathbf{z}} \Pi_m(\mathbf{r}, \mathbf{r}') \\ \mathbf{H}(\mathbf{r}, \mathbf{r}') &= j\omega \epsilon_r \epsilon_0 \nabla \times \hat{\mathbf{z}} \Pi_e(\mathbf{r}, \mathbf{r}') + \nabla \times \nabla \times \hat{\mathbf{z}} \Pi_m(\mathbf{r}, \mathbf{r}'). \end{aligned} \quad (3.2)$$

### 3. METAMATERIAL SUPERLENS

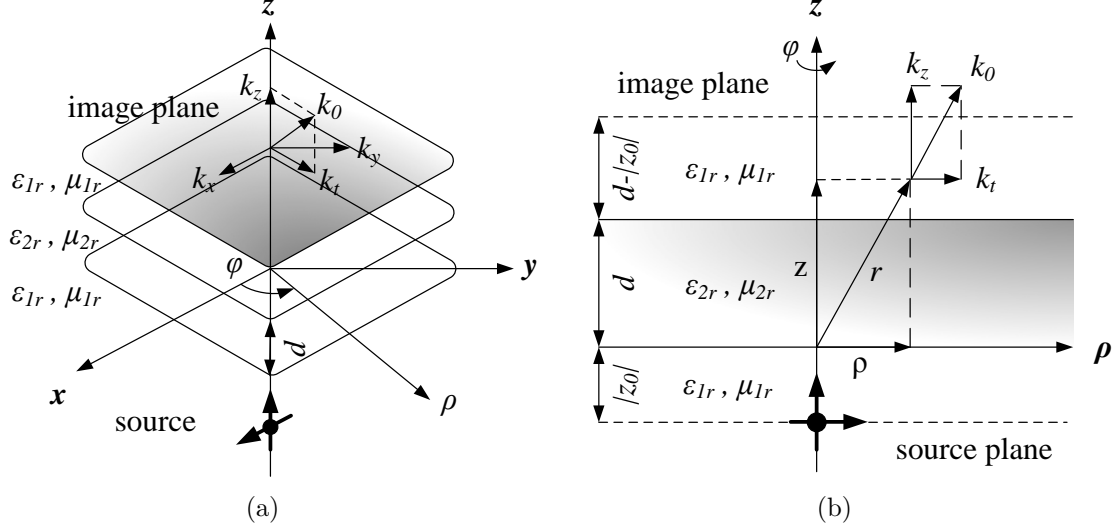


**Figure 3.2:** Problem setup in (a) 3D and (b) 2D.

A perpendicular or longitudinal point source  $\mathbf{J}_0 = J_0 \hat{\mathbf{z}}$  contributes to  $\Pi_e$  and excites TM modes only, whereas a magnetic current element  $\mathbf{M}_0 = M_0 \hat{\mathbf{z}}$  excites only TE modes. Both mode types are excited by a parallel or transversely directed source of either electric  $\mathbf{J}_0 = J_0 \hat{\boldsymbol{\rho}}$  or magnetic type  $\mathbf{M}_0 = M_0 \hat{\boldsymbol{\rho}}$ . The Hertz potentials are

$$\begin{aligned}\Pi_e(\mathbf{r}, \mathbf{r}') &= \left[ \frac{\mathbf{J}_0}{j\omega\epsilon_r\epsilon_0} \frac{\partial}{\partial z'} + \mathbf{M}_0 \times \hat{\mathbf{z}} \right] \cdot \hat{\boldsymbol{\rho}} \xi_e^t(\mathbf{r}, \mathbf{r}') \\ \Pi_m(\mathbf{r}, \mathbf{r}') &= \left[ \hat{\mathbf{z}} \times \mathbf{J}_0 + \frac{\mathbf{M}_0}{j\omega\mu_r\mu_0} \frac{\partial}{\partial z'} \right] \cdot \hat{\boldsymbol{\rho}} \xi_m^t(\mathbf{r}, \mathbf{r}'),\end{aligned}\quad (3.3)$$

for transverse sources  $\mathbf{J}_0 \cdot \hat{\mathbf{z}} = \mathbf{M}_0 \cdot \hat{\mathbf{z}} = 0$  and

$$\begin{aligned}\Pi_e(\mathbf{r}, \mathbf{r}') &= \frac{\mathbf{J}_0 \cdot \hat{\mathbf{z}}}{j\omega\epsilon_r\epsilon_0} \xi_e^l(\mathbf{r}, \mathbf{r}') \\ \Pi_m(\mathbf{r}, \mathbf{r}') &= \frac{\mathbf{M}_0 \cdot \hat{\mathbf{z}}}{j\omega\mu_r\mu_0} \xi_m^l(\mathbf{r}, \mathbf{r}').\end{aligned}\quad (3.4)$$

for longitudinal sources  $\mathbf{J}_0 \times \hat{\mathbf{z}} = \mathbf{M}_0 \times \hat{\mathbf{z}} = 0$ . The electromagnetic fields are evaluated in terms of the scalar functions  $\xi_{e,m}^l$  and  $\xi_{e,m}^t$ , which are defined as

$$\xi_{e,m}^l(\mathbf{r}, \mathbf{r}') = \frac{1}{4\pi} \int_{\infty - j\pi}^{\infty} k_t H_0^{(2)}(k_t \rho) g_{e,m}(z, z_0; k_t) dk_t \quad (3.5)$$

and

$$\xi_{e,m}^t(\mathbf{r}, \mathbf{r}') = \frac{1}{4\pi} \int_{\infty - j\pi}^{\infty} H_1^{(2)}(k_t \rho) g_{e,m}(z, z_0; k_t) dk_t. \quad (3.6)$$

## 3.2 Analytical Formulation

For purely longitudinal sources the fields may be derived directly from the scalar Green's function  $\xi_{e,m}^l(\mathbf{r}, \mathbf{r}')$ , which satisfies the scalar wave equation

$$(\nabla^2 + k^2) \xi_{e,m}^l(\mathbf{r}, \mathbf{r}') = \delta(\mathbf{r} - \mathbf{r}'). \quad (3.7)$$

The wavenumber can be decomposed into longitudinal and transversal components  $k_z$  and  $k_t$ , such that:

- $k_t = k_\rho = \sqrt{k_x^2 + k_y^2}$
- $k_{1z}(k_t) = \sqrt{n_1^2 k_0^2 - k_t^2}$  outside the slab
- $k_{2z}(k_t) = \sqrt{n_2^2 k_0^2 - k_t^2}$  inside the slab

The Hankel function of the second kind  $H^{(2)}(k_t \rho)$  ensures that the radiation condition is satisfied as  $\rho \rightarrow \infty$ .

The one-dimensional Green's function  $g_{e,m}(z, z_0; k_t)$  depends on the nature of the  $z$  stratification and is determined from the boundary conditions at  $z = 0$  and  $z = d$  as follows

$$g_{e,m}(z, z_0; k_t) = \begin{cases} \frac{1}{2jk_{1z}} [e^{-jk_{1z}|z-z_0|} - R_{e,m}(k_t)e^{jk_{1z}(z+z_0)}] & z < 0 \\ \frac{1}{2jk_{1z}} e^{jk_{1z}z_0} T_{e,m}(k_t) & \\ \left[ \cos k_{2z}(z-d) - \frac{j}{\tau_{e,m}(k_t)} \sin k_{2z}(z-d) \right] & 0 < z < d \\ \frac{1}{2jk_{1z}} e^{-jk_{1z}(z-d-z_0)} T_{e,m}(k_t) & z > d \end{cases} \quad (3.8)$$

The reflection  $R_{e,m}(k_t)$  and transmission  $T_{e,m}(k_t)$  coefficients of the slab are

$$\begin{aligned} R_{e,m}(k_t) &= \frac{(\tau_{e,m}^2 - 1)(1 - e^{-2jk_{2z}d})}{(\tau_{e,m} + 1)^2 - (\tau_{e,m} - 1)^2 e^{-2jk_{2z}d}} \\ T_{e,m}(k_t) &= \frac{4\tau_{e,m}}{(\tau_{e,m} + 1)^2 e^{jk_{2z}d} - (\tau_{e,m} - 1)^2 e^{-jk_{2z}d}}, \end{aligned} \quad (3.9)$$

with the normalized characteristic impedances

$$\tau_e(k_t) = \frac{k_{2z}\epsilon_1}{k_{1z}\epsilon_2} \quad \text{and} \quad \tau_m(k_t) = \frac{k_{1z}\mu_2}{k_{2z}\mu_1}, \quad (3.10)$$

for TM and TE modes, respectively. A detailed derivation of R and T is given in App. A.

### 3.3 Analytical Properties

In order to ensure a unique specification of the integrals in (3.5) or (3.6) it is necessary to discuss the analytic properties of  $k_{1z}(k_t)$  and  $k_{2z}(k_t)$  in the  $k_t$  plane. The Green's function in (3.8) depends on the integration variable  $k_t$  via  $k_{1z}(k_t)$  and  $k_{2z}(k_t)$ . The dependence is even with respect to  $k_{2z}(k_t)$ , whereas this is not the case for  $k_{1z}(k_t)$ . The lack of evenness implies the existence of first order branch points at  $k_t = \pm n_1 k_0$ .

To comply with conditions at  $|z| \rightarrow \infty$ , the integration path in (3.5) and (3.6) should be located on the sheet of the Riemann surface for  $k_{1z}(k_t)$  where  $\text{Im}\{k_{1z}(k_t)\} < 0$ . The branch cuts, as shown in Fig. 3.3, are drawn along the hyperbolas  $\text{Re}\{k_t\} \text{Im}\{k_t\} = \text{Re}\{n_1 k_0\} \text{Im}\{n_1 k_0\}$ , on which  $\text{Im}\{k_{1z}(k_t)\}$  vanishes. The integration is over the entire spectrum containing both propagating ( $|k_t| \leq n_1 k_0$ ) and evanescent ( $|k_t| > n_1 k_0$ ) modes. The sign of  $\text{Re}\{k_{1z}\}$  is positive along the path of integration and  $\text{Im}\{k_{1z}\}$  is negative on the entire top sheet. The branch cut along the negative real axis arises from the logarithmic singularity of the Hankel function at  $k_t = 0$ .

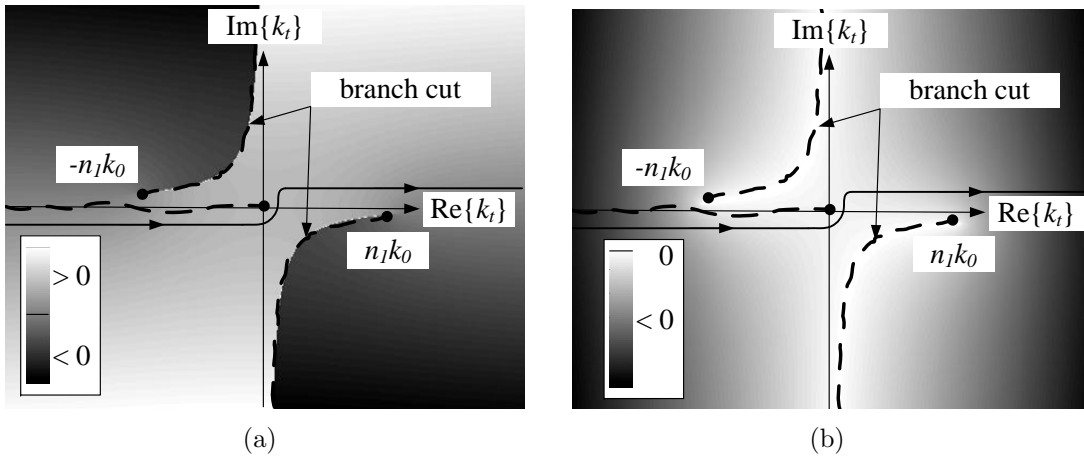


**Figure 3.3:** Analytic properties of (a)  $\text{Re}\{k_{1z}\}$  and (b)  $\text{Im}\{k_{1z}\}$  in the  $k_t$  plane.

The branch point singularities at  $k_t = \pm n_1 k_0$  lie on the  $\text{Re}\{k_t\}$  axis when medium 1 is lossless and  $n_1$  is purely real. In dissipative media, on the other hand, where  $n_1$  is complex, the branch points are displaced into the fourth and second quadrants of the complex  $k_t$  plane. In the absence of losses the integration path should be indented around the singularities into the first or third quadrants, for branch-point locations on the positive or negative  $\text{Re}\{k_t\}$  axis, respectively.

Pole singularities due to the denominator of  $R_{e,m}(k_t)$  or  $T_{e,m}(k_t)$  also exist. Their location is determined from the transcendental equation

$$(\tau_{e,m}(k_t^p) + 1)^2 e^{j\sqrt{\epsilon_{2r}\mu_{2r}k_0^2 - k_t^p{}^2}d} = (\tau_{e,m}(k_t^p) - 1)^2 e^{-j\sqrt{\epsilon_{2r}\mu_{2r}k_0^2 - k_t^p{}^2}d}. \quad (3.11)$$

As  $|k_t^p| \rightarrow \infty$  (electrostatic limit) the longitudinal wavenumber inside and outside the slab can be expressed as

$$k_{1z}(k_t^p) \approx k_{2z}(k_t^p) \approx \begin{cases} -jk_t^p & \text{Re}\{k_t^p\} > 0 \\ +jk_t^p & \text{Re}\{k_t^p\} < 0 \end{cases}, \quad (3.12)$$

yielding

$$k_t^p \approx \pm \left\{ \frac{1}{d} \ln \left( \frac{\tau_{e,m}(\infty) - 1}{\tau_{e,m}(\infty) + 1} \right) + jm \frac{\pi}{d} \right\} \quad m = 0, \pm 1, \pm 2, \dots, \quad (3.13)$$

with  $\tau_e(\infty) = \epsilon_{1r}/\epsilon_{2r}$  for TM and  $\tau_m(\infty) = \mu_{2r}/\mu_{1r}$  for TE modes.

There is an infinite number of poles, and their location is shown in Fig. 3.4. The poles describe the excitation of waveguide modes, which propagate inside the slab and decay exponentially away from it. For a slab surrounded by vacuum ( $\epsilon_{1r} = \mu_{1r} = 1$ ), the poles move outward along the  $\text{Re}\{k_t\}$  axis and disappear from the complex plane in the limit  $\epsilon_{2r} \rightarrow -1$  and  $\mu_{2r} \rightarrow -1$ . The pole singularities at the real axis are treated in a way analogous to the branch point singularities: either by displacement from the real axis by introducing a small amount of loss or by deforming the integration path around the singularities.

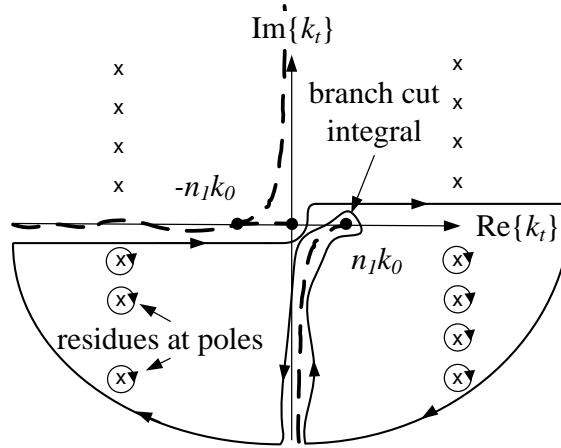


**Figure 3.4:** Integration contour.

Furthermore, by deforming the integration path into the lower half of the complex  $k_t$  plane, the contour integrals in (3.5) and (3.6) can be transformed into a sum of residues at the poles in the lower half plane and an integral around the branch cut traversed in opposite directions. There is no contribution from the semi-circle contour as it goes to  $\infty$ .

The spatial intensity distribution immediately behind the slab and in the vicinity of the image plane provide essential information about the imaging capabilities of the slab. The distribution is obtained by integrating (3.5) or (3.6) either analytically or numerically. As will be shown in the following section, a closed form solution for the ideal imaging condition with  $\epsilon_{1r} = \mu_{1r} = 1$  and  $\epsilon_{2r} = \mu_{2r} = -1$  exists. On the other hand, if  $\epsilon_{2r} = \mu_{2r} \neq -1$ , it is not possible to evaluate the integral in terms of

### 3. METAMATERIAL SUPERLENS

elementary functions in closed form. An asymptotic evaluation based on the saddle point technique or method of steepest descent [39] is possible only when  $k|z_0| \gg 1$  and  $k|z-d| \gg 1$ . Close to the slab interface, in the vicinity of the image plane (near field), the integrands do not have the required form and the asymptotic method fails. As a result of this, an algorithm based on Gauss-Kronrod quadrature [93], an efficient numerical integration technique for oscillatory integrands, is developed for this purpose and the integral numerically evaluated.

#### 3.4 Ideal Imaging

When traversing the space between source and image planes which are separated by a distance of  $2d$ , each Fourier component undergoes some change according to the total transmission coefficient  $\mathbf{T}_{e,m}^{\mathbf{T}}(k_t)$ . Let us assume that a plane wave  $e^{-jk_z z}$  is incident at  $z = z_0$  and we want to detect it at  $z = 2d - |z_0|$ . In medium 1:  $\mathbf{T}_1(k_t) = e^{-jk_{1z}z}$ , whereas in medium 2:  $\mathbf{T}_2(k_t) = \mathbf{T}_{e,m}(k_t)$  (given by 3.9) yielding

$$\begin{aligned} \mathbf{T}_{e,m}^{\mathbf{T}}(k_t) &= \mathbf{T}_1(k_t)\mathbf{T}_2(k_t)\mathbf{T}_1(k_t) \\ &= e^{-jk_{1z}(k_t)|z_0|}\mathbf{T}_{e,m}(k_t)e^{-jk_{1z}(k_t)(d-|z_0|)} \\ &= e^{-jk_{1z}(k_t)d}\mathbf{T}_{e,m}(k_t) \end{aligned} \quad (3.14)$$

or

$$\mathbf{T}_{e,m}^{\mathbf{T}}(k_t) = \frac{4\tau_{e,m}(k_t)e^{-jk_{1z}(k_t)d}}{(\tau_{e,m}(k_t) + 1)^2 e^{jk_{2z}(k_t)d} - (\tau_{e,m}(k_t) - 1)^2 e^{-jk_{2z}(k_t)d}}. \quad (3.15)$$

As mentioned previously, for a double negative slab surrounded by vacuum ideal imaging requires that  $\epsilon_{2r} = \mu_{2r} = -1$ . Since  $k_{1z} = k_{2z} = \tilde{k}_z$  in this case, the TM and TE characteristic impedances (3.10) are equal to -1 resulting in  $\mathbf{R}_{e,m}(k_t) = 0$ ,  $\mathbf{T}_{e,m}(k_t) = e^{j\tilde{k}d}$  and  $\mathbf{T}_{e,m}^{\mathbf{T}}(k_t) = 1$ . Each mode emitted from the source is transmitted uniformly through the slab and is recovered perfectly at the image plane. The double negative slab perfectly translates the object plane to the image plane.

The Green's function simplifies to

$$g_{e,m}(z, z_0; k_t) = \begin{cases} \frac{1}{2j\tilde{k}_z} e^{-j\tilde{k}_z|z-z_0|} & z < 0 \\ \frac{1}{2j\tilde{k}_z} e^{-j\tilde{k}_z(|z_0|-z)} & 0 < z < d \\ \frac{1}{2j\tilde{k}_z} e^{-j\tilde{k}_z(z-2d+|z_0|)} & z > d \end{cases} \quad (3.16)$$

For an electric dipole with  $\mathbf{J}_0 = J_0 \hat{\mathbf{z}}$  and  $z > d$  the integral in (3.5) becomes

$$\xi_{e,m}^t(\mathbf{r}, \mathbf{r}') = \frac{1}{8\pi j} \int_{\infty_{e^{-j\pi}}^{-j\pi}}^{\infty} \frac{k_t}{\tilde{k}_z} H_0^{(2)}(k_t \rho) e^{-j\tilde{k}_z(z-2d+|z_0|)} dk_t. \quad (3.17)$$

By changing the integration variable from  $k_t$  to  $\tilde{k}_z = \sqrt{k_0^2 - k_t^2}$ , so that  $d\tilde{k}_z = -(k_t/\tilde{k}_z)dk_t$ , the above integral can be integrated in closed form (Equation 6.616-4 in [47]) to yield

$$\xi_{e,m}^l(\mathbf{r}, \mathbf{r}') = \frac{e^{-jk_0\sqrt{\rho^2+(z-2d+|z_0|)^2}}}{4\pi\sqrt{\rho^2+(z-2d+|z_0|)^2}}, \quad (3.18)$$

which is identical to the Green's function of a dipole radiating at  $z = 2d - |z_0|$  [21; 57]. The fields are obtained from (3.4) and it is evident that a perfect reproduction of the source is obtained.

However, in the region  $d < z < 2d - |z_0|$  the integral in (3.17) diverges due to the fact that  $z - 2d + |z_0| < 0$  and the exponent grows as  $k_t \rightarrow \pm\infty$ . This divergence arises purely from the evanescent part of the spectrum, since for  $0 < k_t < k_0$  the integral is well defined. For  $z \geq 2d - |z_0|$  the factor  $z - 2d + |z_0|$  changes its sign and the integral converges.

The problem of non-integrable fields has been raised in [42; 84] and occurs only for the idealized case with  $\epsilon_{2r} = \mu_{2r} = -1$ . For other combinations of  $\epsilon_{2r}$  and  $\mu_{2r}$ , the remedy is provided by a high-frequency cutoff as will be discussed next.

### 3.5 Non-Ideal Imaging

Double negative metamaterial slabs provide perfect imaging only under the assumption of being non-dispersive, completely lossless, impedance matched, and having a refractive index of -1 relative to the surrounding medium. However, absorption and dispersion (Sec. 2.6) is always present in practice. The ideal imaging condition is therefore an idealization, which is difficult to reach in reality.

If  $\text{Re}\{\epsilon_{2r}\} \neq \text{Re}\{\mu_{2r}\} \neq -1$  and/or  $\text{Im}\{\epsilon_{2r}\} \neq \text{Im}\{\mu_{2r}\} \neq 0$  a high-frequency cutoff  $k_t^c$  in  $T(k_t)$  exists. In the electrostatic limit ( $|k_t| \rightarrow \infty$ ) it is approximately given by (3.11). Replacing  $k_t^p$  with  $k_t^c$  and solving for  $k_t^c$  yields

$$k_{te,tm}^c \approx \left| \frac{1}{d} \ln \left( \frac{\tau_{e,m} - 1}{\tau_{e,m} + 1} \right) \right|. \quad (3.19)$$

The highest resolvable wavenumber  $k_t^c$  determines the spectral width of the transmitted spectrum and imposes a limit on the minimum feature resolvable by the slab [23; 110]. The transmission coefficient of the slab decays exponentially for  $|k_t| > k_t^c$ , as a result of which the spatial components above  $k_t^c$  die out before reaching the image plane and the image is no longer perfect. Approaching the ideal case with  $\epsilon_{1r} = \mu_{1r} = 1$  and  $\epsilon_{2r}, \mu_{2r} \rightarrow -1$ ,  $k_t^c \rightarrow \infty$  and the resolution improves. Major factors yielding a high-frequency cutoff are:

- Refractive index and impedance mismatch between slab and surrounding medium, i.e  $n_1 \neq -|n_2|$  and/or  $\eta_1 \neq \eta_2$

### 3. METAMATERIAL SUPERLENS

---

- Presence of losses in slab material, i.e.  $\text{Im} \{\epsilon_{2r}\} \neq 0$  and/or  $\text{Im} \{\mu_{2r}\} \neq 0$
- Dispersion in slab material, i.e.  $\epsilon_{2r}(\omega)$  and/or  $\mu_{2r}(\omega)$
- Structural periodicity in the slab, i.e. finite unit cell size of metamaterials.

As already discussed in Chapter 2, metamaterials are made of unit cells with finite dimensions. If the size of a unit cell is  $d$ , there is no possibility of reproducing a Fourier component greater than  $k_t = 2\pi/d$  and modes with large values of  $k_t$  are subject to a cutoff [28; 110]. In addition, metamaterials are highly dispersive and lossy in the regions where the permittivity and permeability are simultaneously negative. As will be shown in the following section, even a small amount of loss in the slab material leads to an attenuation of evanescent modes with large  $k_t$ , resulting in a degradation of the image quality.

## 3.6 Results

The imaging characteristics of non-ideal double negative slabs surrounded by vacuum are investigated with the developed tool. Unless otherwise indicated, the slab has a thickness of  $d = 0.3\lambda$  and is excited by a Hertzian dipole radiating at  $z = z_0 = -0.2\lambda$ . As shown in Fig. 3.5(a), the focus is at  $z = 2d - |z_0| = 0.4\lambda$  in the ideal case. Longitudinal  $\mathbf{J}_0 = \hat{\mathbf{z}}$  and transverse  $\mathbf{J}_0 = \hat{\mathbf{x}}$  source excitations are considered.

Field intensities in the plane of the optical axis ( $yz$  plane) and transversal planes ( $xy$  plane) behind the slab are evaluated. The electric field strength

$$|\mathbf{E}| = \sqrt{|E_x|^2 + |E_y|^2 + |E_z|^2} \quad (3.20)$$

is measured in volt per meter [V/m]. Due to high intensities ( $I$ ) in the vicinity of the image plane, a logarithmic scale with  $I = 20 \log |\mathbf{E}|$  dB(V/m) is used.

The spot size  $\Delta y$  as shown in Fig. 3.5(b), defined as the full width at half maximum (FWHM) value of the main lobe of the intensity pattern along transversal planes, serves as a measure of the image quality. It is determined as  $\Delta y = 2(y_{I_{\max}} - y_{I_{\max}/2})$  and represents the distance over which the intensity of the main lobe falls to half its maximum value. As the material parameters of the slab approach the ideal case ( $\epsilon_{2r}, \mu_{2r} \rightarrow -1$ )  $\Delta y \rightarrow 0$ , indicating the improvement in resolution. For a diffraction limited image which is restricted to propagating modes only  $\Delta y = 0.42\lambda$ . In this case the spatial variation of the field distribution in the image plane is a sinc function with a main lobe zero-to-zero spacing of approximately one wavelength.

In the following sections the material parameters of the slab are perturbed from the ideal case, by varying the real and imaginary parts of  $\epsilon_{2r}$  and  $\mu_{2r}$  by  $\sigma$  and  $\Gamma$ , respectively. Three different perturbation mechanisms are considered:

1. Sec. 3.6.1:  $\epsilon_{2r} = -1 - j\Gamma$  and  $\mu_{2r} = -1 - j\Gamma$
2. Sec. 3.6.2:  $\epsilon_{2r} = -1/(1 + \sigma) - j\Gamma$  and  $\mu_{2r} = -(1 + \sigma) - j\Gamma$

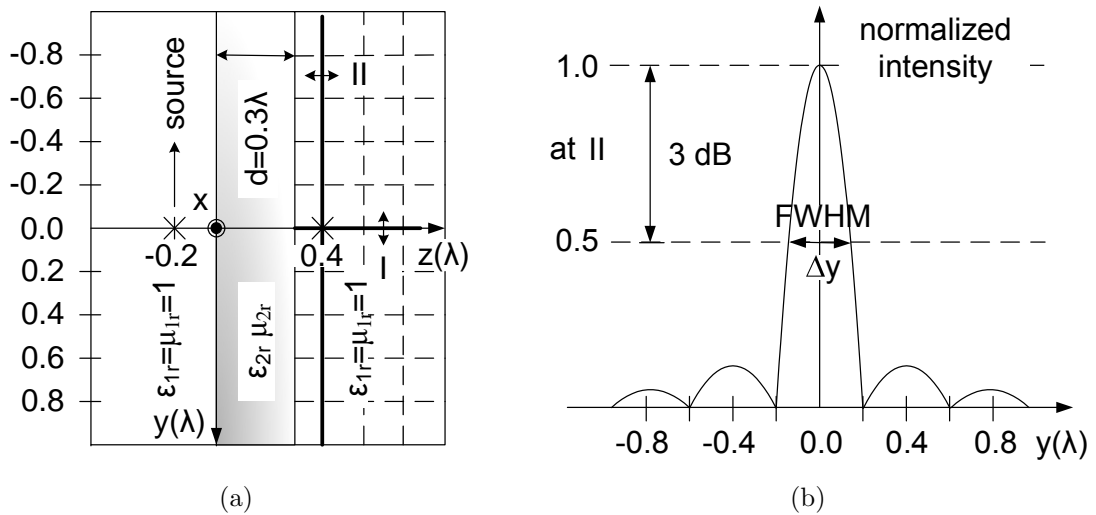


**Figure 3.5:** (a) Considered configuration and (b) intensity pattern at transversal planes, showing the spot size  $\Delta y$  determined from the FWHM value of the main lobe.

### 3. Sec. 3.6.3: $\epsilon_{2r} = -1/(1 + \sigma) - j\Gamma$ and $\mu_{2r} = -1$

The influence of losses are treated first in Sec. 3.6.1. The refractive index of the slab is thereby perturbed from the ideal case such that  $\text{Re}\{n_2\} = -1$  and  $\text{Im}\{n_2\} \neq 0$ . The slab impedance remains unperturbed and is perfectly matched to vacuum.

In addition to losses the real parts of  $\epsilon_{2r}$  and  $\mu_{2r}$  are perturbed next. Neglecting terms of second order, the perturbation mechanism in Sec. 3.6.2 results in a slab with  $\text{Re}\{n_2\} \approx -1$ ,  $\text{Im}\{n_2\} \neq 0$ ,  $\text{Re}\{\eta_2\} \neq \eta_0$  and  $\text{Im}\{\eta_2\} \approx 0$ .

The most perturbed configuration with  $\text{Re}\{n_2\} \neq -1$ ,  $\text{Im}\{n_2\} \neq 0$ ,  $\text{Re}\{\eta_2\} \neq \eta_0$  and  $\text{Im}\{\eta_2\} \neq 0$  is investigated in Sec. 3.6.3. This mechanism of the image distortion can play a considerable role in the case of excitation of the slab with generally oriented sources [25].

The effect of the slab thickness on the image quality is investigated in Sec. 3.6.4. Finally, full wave time domain simulations based on the TLM method are utilized to determine the imaging characteristics of transversely limited slabs in Sec. 3.6.5 and imaging with dispersive broadband Gaussian pulses in Sec. 3.6.6.

## 3.6.1 Small Amount of Absorption

Let us assume that the material parameters of the slab are perturbed from the ideal case according to

$$\epsilon_{2r} = -1 - j\Gamma \quad \text{and} \quad \mu_{2r} = -1 - j\Gamma \quad (3.21)$$

where losses are characterized with  $\Gamma \ll 1$ , being positive for a passive medium.

Prior to a detailed investigation of the intensity distribution in the vicinity of the image plane the problem is considered in the electrostatic limit as  $|k_t| \rightarrow \infty$ . For

### 3. METAMATERIAL SUPERLENS

$|k_t| \gg k_0$ , the longitudinal wavenumbers inside and outside the slab can be expressed as  $k_{1z} \approx k_{2z} \approx -j|k_t|$ , so that (3.15) becomes

$$T_{e,m}^T(k_t) \approx \frac{4\tau_{e,m}e^{-|k_t|d}}{(\tau_{e,m} + 1)^2e^{|k_t|d} - (\tau_{e,m} - 1)^2e^{-|k_t|d}}. \quad (3.22)$$

The second term in the denominator vanishes as  $|k_t| \rightarrow \infty$  and  $\tau_{e,m} \rightarrow -1$ , as a result of which

$$T^T(k_t) \approx T_{e,m}^T(k_t) \approx \frac{4e^{-2|k_t|d}}{\Gamma^2}. \quad (3.23)$$

The presence of any nonzero absorption leads to a strong suppression of the transmitted spectrum with large  $k_t$ . The decay is exponential and the same for TE and TM modes. Therefore, it makes essentially no difference by which dipole type and orientation the slab is excited with. The magnitude of  $T^T(k_t)$  for  $10^{-10} < \Gamma < 10^{-4}$  is plotted in Fig. 3.6. The corresponding cutoff wavenumbers are approximated from (3.19) as

$$k_t^c \approx k_{te,tm}^c \approx \frac{1}{d} \ln \left[ \frac{2}{\Gamma} \right] \quad (3.24)$$

and are listed in Tab. 3.1. It is clearly seen that  $k_t^c$  decreases with increasing  $\Gamma$ , so that fewer modes are uniformly transferred from source to image plane resulting in a degradation of the image quality.

	I	II	III	IV
$\Gamma$	$10^{-4}$	$10^{-6}$	$10^{-8}$	$10^{-10}$
$k_t^c/k_0$	5.25	7.70	10.14	12.58
$\Delta y/\lambda$	0.11	0.08	0.06	0.05

**Table 3.1:**  $k_t^c$  and  $\Delta y$  at image plane  $z = 0.4\lambda$ , for various values of  $\Gamma$ .

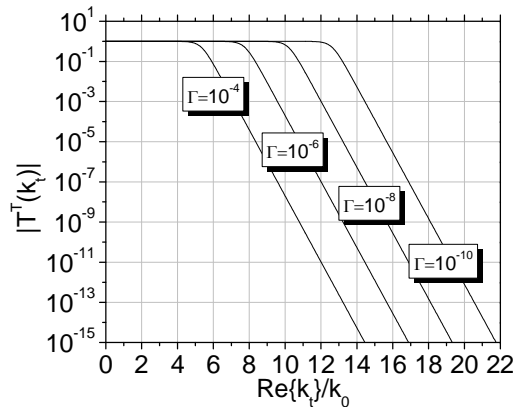


**Figure 3.6:**  $T^T(k_t)$  for a slab with material parameters as given in (3.24).

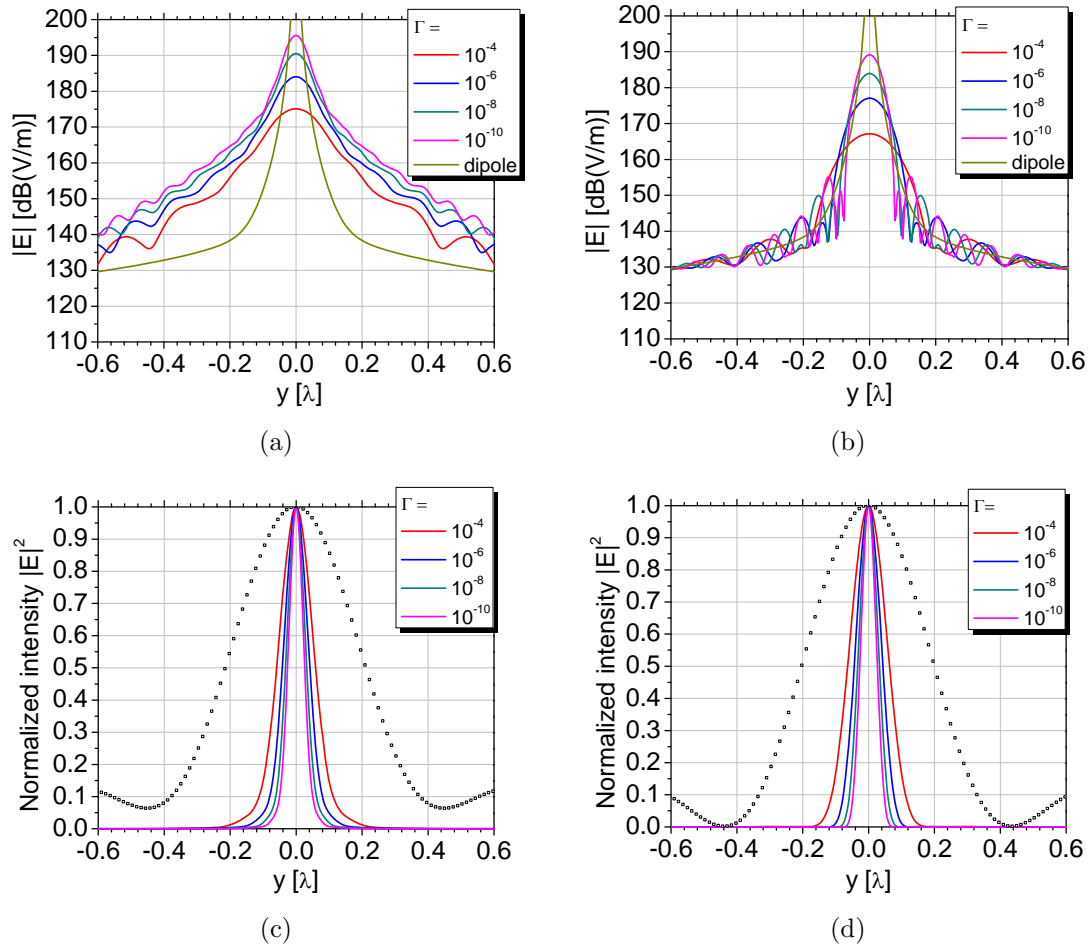


**Figure 3.7:**  $|\mathbf{E}|$  along the  $y$  axis at image plane  $z = 0.4\lambda$  ( $x = 0$ ) for (a)  $\mathbf{J}_0 = \hat{\mathbf{z}}$  and (b)  $\mathbf{J}_0 = \hat{\mathbf{x}}$ . The dipole field in the ideal case is shown for comparison purposes. Corresponding normalized field intensities for (c)  $\mathbf{J}_0 = \hat{\mathbf{z}}$  and (d)  $\mathbf{J}_0 = \hat{\mathbf{x}}$ . Squares: diffraction limited intensity distribution.

The intensity distribution at the image plane ( $z = 0.4\lambda$ ) is investigated next. Loss factors between  $\Gamma = 10^{-4}$  and  $\Gamma = 10^{-10}$  are considered. Results for perpendicular  $\mathbf{J}_0 = \hat{\mathbf{z}}$  and parallel  $\mathbf{J}_0 = \hat{\mathbf{x}}$  source excitation are plotted in Fig. 3.7 (a) and (b), respectively. The normalized intensity distributions are shown in Fig. 3.7 (c) and (d), and the corresponding FWHM values are provided in Tab. 3.1.

The maximum attainable intensity at the image plane decreases as more loss is introduced. Increasing the amount of absorption in the slab leads to a broadening of the main lobe, indicating the degradation of the image. For  $\Gamma = 10^{-4}$  the FWHM value of the main lobe is  $\Delta y[\text{I}] = 0.11\lambda$  and decreases to  $\Delta y[\text{IV}] = 0.05\lambda$  for  $\Gamma = 10^{-10}$ . The enhancement is  $\Delta y[\text{I}]/\Delta y[\text{IV}] = 2.2$ , which is in accordance with the cutoff wavenumbers, i.e.  $k_t^c[\text{I}] = 12.58k_0$ ,  $k_t^c[\text{IV}] = 5.25k_0$  and  $k_t^c[\text{I}]/k_t^c[\text{IV}] = 2.4$ .

The resolution degrades by approximately 50% as  $\Gamma$  increases from  $10^{-10}$  to  $10^{-4}$ . However, as shown in Fig. 3.7 (c) and (d), the image is still below the diffraction limited one with  $\Delta y = 0.42\lambda$ . It can be concluded that, although a double negative slab provides subwavelength imaging, the logarithmic dependence between  $\Gamma$  and  $k_t^c$

### 3. METAMATERIAL SUPERLENS

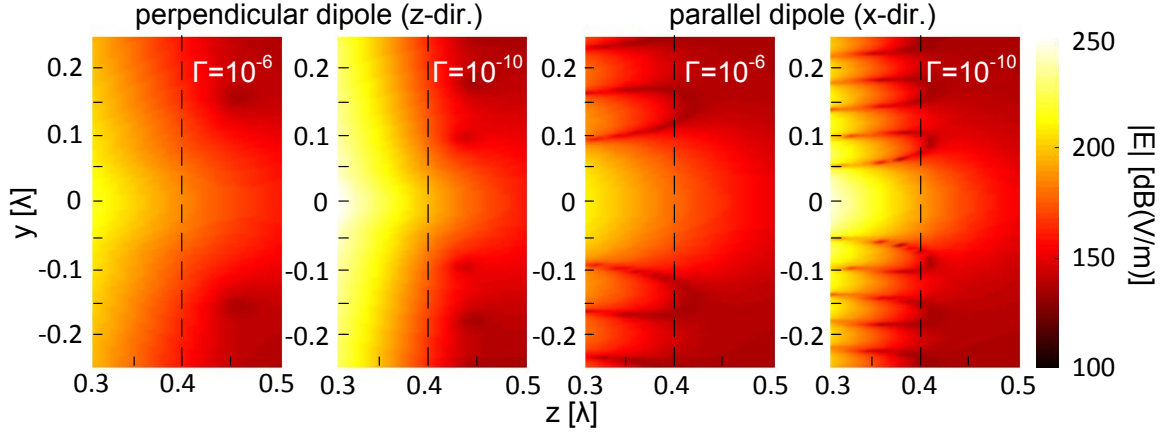


**Figure 3.8:**  $|\mathbf{E}|$  in the  $yz$  plane, immediately behind the slab. Perpendicular  $\mathbf{J}_0 = \hat{\mathbf{z}}$  and parallel  $\mathbf{J}_0 = \hat{\mathbf{x}}$  source excitation for  $\Gamma = 10^{-6}$  and  $\Gamma = 10^{-10}$ . The image plane is shown by the dashed line.

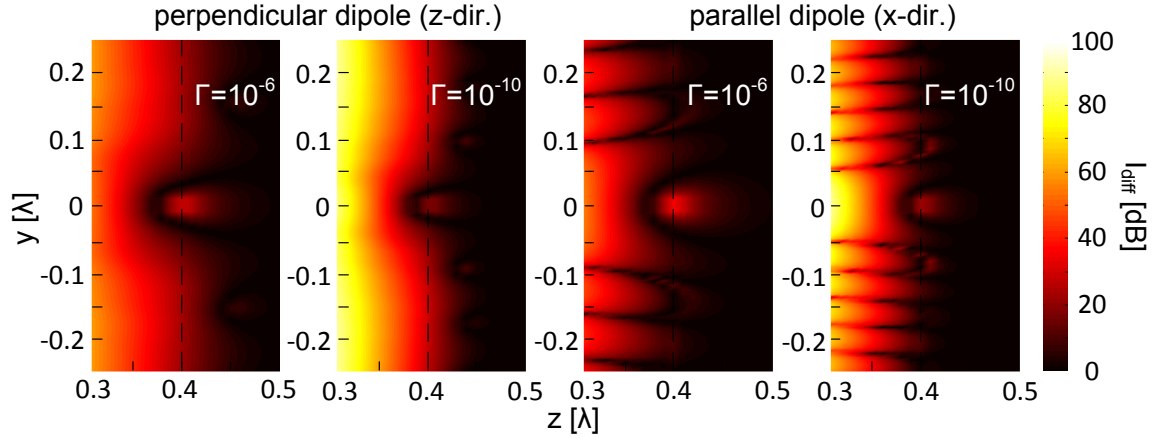


**Figure 3.9:**  $I_{\text{diff}}$  for the same configurations in Fig. 3.8.

complicates fabrication of a metamaterial superlens with performance close to 100%.

A common misconception regarding metamaterial superlenses is that they provide subwavelength imaging in three dimensional space. Three dimensional focusing requires that maximum intensity occurs exactly at the focal point ( $x = 0$ ,  $y = 0$ ,  $z = 0.4\lambda$ ) and declines in all directions radially outwards. However, a double negative slab is only capable of two dimensional imaging and not focusing in three dimensional space [79]. This is visualized by plotting the intensity distribution in the  $yz$  plane, immediately behind the slab.

The results for perpendicular  $\mathbf{J}_0 = \hat{\mathbf{z}}$  and parallel  $\mathbf{J}_0 = \hat{\mathbf{x}}$  source excitations with  $\Gamma = 10^{-6}$  and  $\Gamma = 10^{-10}$  are shown in Fig. 3.8. Intensity is at maximum at the slab-vacuum interface ( $z = 0.3\lambda$ ) and attenuates with increasing  $z$ , irrespective of the type of excitation and amount of absorption. As mentioned in Sec. 3.3, this is due to the excitation of waveguide modes which propagate inside the slab and decay exponentially away from it. A certain amount of energy couples to these modes and diffuses into the surrounding medium, thereby distorting the focal spot.

In the region  $0.3\lambda < z < 0.4\lambda$  the fields grow to infinity as  $\Gamma \rightarrow 0$ , resulting in divergent fields in the ideal case with  $\epsilon_{2r} = \mu_{2r} = -1$  (Sec. 3.4). However, in the limit

$\Gamma = 0$ , the fields replicate themselves perfectly at the image plane and for  $z \geq 0.4\lambda$ .

In order to visualize this phenomenon, following parameter is defined

$$I_{\text{diff}} = \left| 20 \log \frac{|\mathbf{E}|}{|\mathbf{E}|_{\text{D}}} \right|, \quad (3.25)$$

with  $|\mathbf{E}_{\text{D}}|$  representing the field of a dipole located at the focal point  $z = 2d - |z_0| = 0.4\lambda$  and radiating in free space without the double negative slab. A value of  $I_{\text{diff}} = 0$  indicates thereby that the fields emitted by the source are uniquely transferred to the focal point behind the slab. Same configurations as in Fig. 3.8 are considered. The results are plotted in Fig. 3.9.

In the region  $0.3\lambda < z < 0.4\lambda$ , the intensity deviates strongly from that of a dipole located at  $z = 0.4\lambda$  and radiating in free space, and the smaller  $\Gamma$  the greater the intensity mismatch. For  $z \geq 0.4\lambda$ , on the other hand, the intensity mismatch decreases with decreasing  $\Gamma$ , confirming that in the limit as  $\Gamma \rightarrow 0$  the fields replicate themselves perfectly at the image plane. It is therefore concluded that a double negative slab does not provide a true three dimensional image of the source and it is more appropriate to identify its imaging capabilities as two dimensional.

### 3.6.2 Unit Refractive Index

Consider the slab with material parameters

$$\epsilon_{2r} = -1/(1 + \sigma) - j\Gamma \quad \text{and} \quad \mu_{2r} = -(1 + \sigma) - j\Gamma \quad (3.26)$$

where in addition to losses the real parts of  $\epsilon_{2r}$  and  $\mu_{2r}$  are perturbed by  $\sigma$ . Neglecting second order terms and assuming that  $\Gamma \rightarrow 0$ , the refractive index and impedance of the slab are approximately given by

$$n_2 \approx -1 - j\Gamma \quad \text{and} \quad \eta_2 \approx (1 + \sigma)\eta_0. \quad (3.27)$$

The real part of the slabs refractive index retains its value of  $\text{Re}\{n_2\} = -1$ , so that propagating modes are still focused at  $z = 2d - |z_0| = 0.4\lambda$ . On the other hand, due to a impedance mismatch between the slab and surrounding space, i.e.  $\text{Re}\{\eta_2\}/\eta_0 = 1 + \sigma$ , the reflection coefficient is no more zero.

In the electrostatic limit as  $k_t \rightarrow \pm\infty$  and under the assumption that  $k_{1z} \approx k_{2z} \approx -j|k_t|$ , the TE and TM mode normalized characteristic impedances in (3.10) depend solely on the material parameters of the slab. In the limit  $\Gamma \rightarrow 0$  they are identical to  $\tau = \tau_{e,m} \approx -(1 + \sigma)$ . Furthermore, for this type of perturbation it follows from (3.19) that  $k_{te}^c = k_{tm}^c = k_t^c$  and  $T_e^T(k_t) = T_m^T(k_t) = T^T(k_t)$ , so that the TE and TM modes are transmitted equally by the slab and the type and orientation of the dipole excitation do not matter. For  $\Gamma$  and  $\sigma \ll 1$ ,  $k_t^c$  is approximately given by

### 3. METAMATERIAL SUPERLENS

$$k_t^c \approx \begin{cases} \frac{1}{d} \ln \left[ \frac{2}{\Gamma} \right] & \text{if } \sigma < \Gamma \\ \frac{1}{d} \ln \left[ \frac{2}{\sigma} \right] & \text{if } \sigma > \Gamma. \end{cases} \quad (3.28)$$

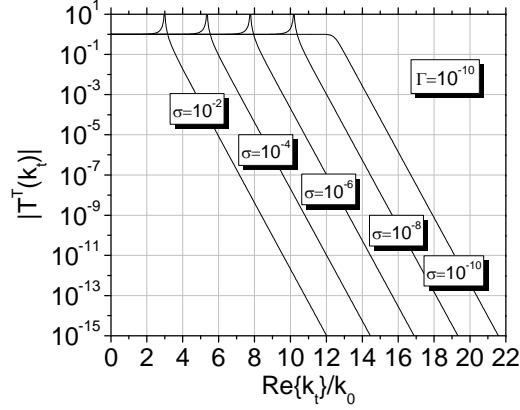


**Figure 3.10:**  $T^T(k_t)$  for a slab with material parameters as given in (3.26)

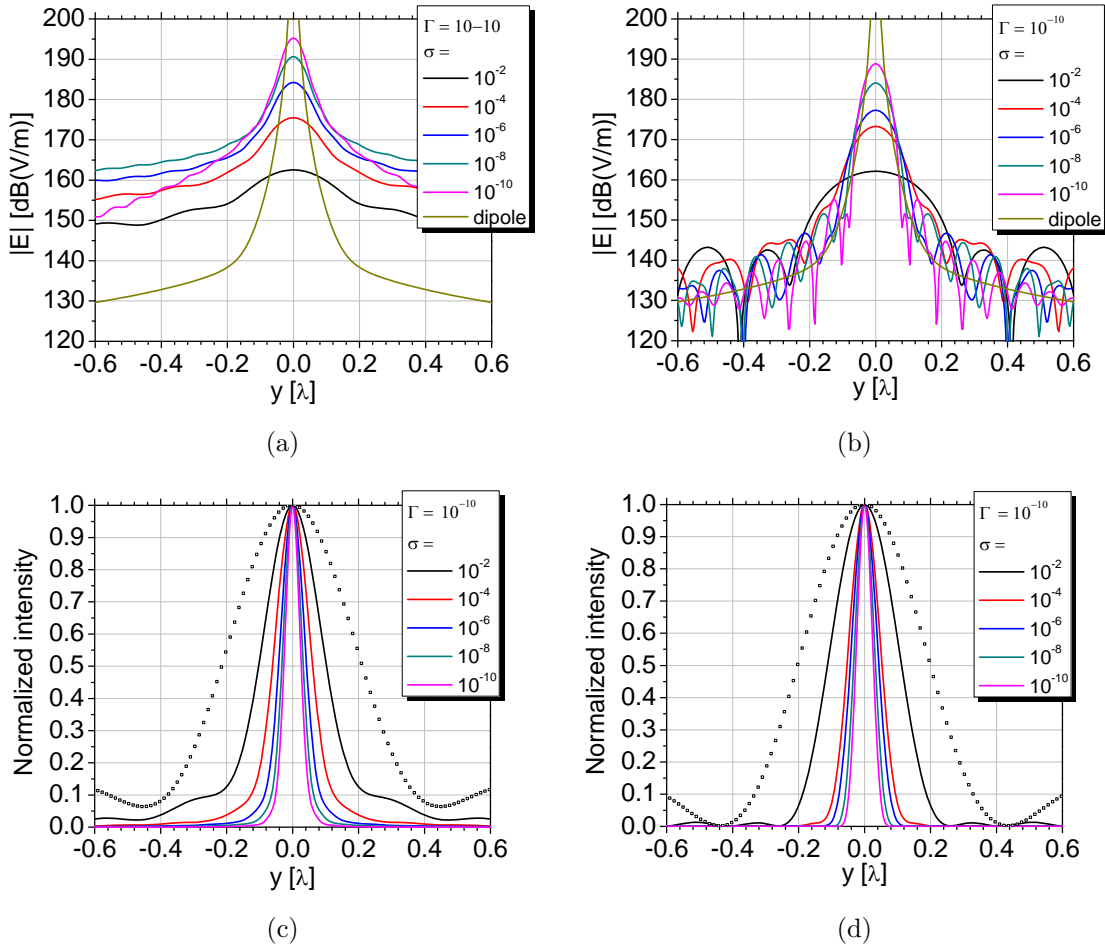


**Figure 3.11:**  $|E|$  along the  $y$  axis at image plane  $z = 0.4\lambda$  ( $x = 0$ ) for (a)  $\mathbf{J}_0 = \hat{z}$  and (b)  $\mathbf{J}_0 = \hat{x}$ . The dipole field in the ideal case is shown for comparison purposes. Corresponding normalized field intensities for (c)  $\mathbf{J}_0 = \hat{z}$  and (d)  $\mathbf{J}_0 = \hat{x}$ . Squares: diffraction limited intensity distribution.

The total transmission coefficient  $T^T(k_t)$  is plotted in Fig. 3.10 for  $10^{-10} < \sigma < 10^{-2}$  and  $\Gamma = 10^{-10}$ . The highest obtainable cutoff is limited to  $k_t^c \approx 12.58k_0$  and is achieved with  $\sigma \approx \Gamma \approx 10^{-10}$ , showing that the effect of absorption can be neglected as long as  $\sigma > \Gamma$  (3.28). Analogous to the case in Sec. 3.6.1,  $k_t^c$  decreases with increasing  $\sigma$ , indicating the degradation of the image quality.

The intensity distribution at the image plane ( $z = 0.4\lambda$ ) is investigated next. Perturbation values between  $\sigma = 10^{-10}$  and  $\sigma = 10^{-2}$  are considered. The amount of absorption is thereby fixed at  $\Gamma = 10^{-10}$ . The results for perpendicular  $\mathbf{J}_0 = \hat{\mathbf{z}}$  and parallel  $\mathbf{J}_0 = \hat{\mathbf{x}}$  source excitation are plotted in Fig. 3.11 (a) and (b), respectively. The corresponding normalized intensity distributions are shown in Fig. 3.11 (c) and (d). As expected, the main lobe broadens and the maximum attainable intensity decreases as  $\sigma$  increases. The FWHM value of the main lobe increases from  $0.04\lambda$  for  $\sigma = 10^{-10}$  to  $0.21\lambda$  for  $\sigma = 10^{-2}$ . The resolution degrades thereby by approximately 80%.

### 3.6.3 Non-Unity Refractive Index

According to the formulation in Sec. 3.2, a perpendicular dipole  $\mathbf{J}_0 = J_0\hat{\mathbf{z}}$  excites TM modes and a magnetic current element  $\mathbf{M}_0 = M_0\hat{\mathbf{z}}$  excites TE modes only. Both mode types are excited by a parallel directed dipole of either electric  $\mathbf{J}_0 = J_0\hat{\boldsymbol{\rho}}$  or magnetic type  $\mathbf{M}_0 = M_0\hat{\boldsymbol{\rho}}$ .

Up to now perturbations for which TE and TM modes are transmitted equally by the double negative slab have been considered. However, this may not always be the case. The unequal transmission of TE and TM portions of the fields is identified and studied next.

Let us assume for instance that

$$\epsilon_{2r} = -1/(1 + \sigma) - j\Gamma \quad \text{and} \quad \mu_{2r} = -1. \quad (3.29)$$

For this type of perturbation  $\text{Re}\{n_2\} \neq -1$ ,  $\text{Im}\{n_2\} \neq 0$ ,  $\text{Re}\{\eta_2\} \neq \eta_0$  and  $\text{Im}\{\eta_2\} \neq 0$ . For  $\sigma$  and  $\Gamma \ll 1$ ,  $\text{Re}\{n_2\} \approx -1$ , so that propagating modes are still focused at  $z = 0.4\lambda$ . Furthermore,  $\tau_e(k_t)$  does not change and is the same as in Sec. 3.6.2. As  $|k_t| \rightarrow \infty$ , the approximate cutoff wavenumber for TM modes ( $k_{te}^c$ ) remains thereby unaffected and is given by (3.28). For TE modes, on the other hand, with  $\mu_{1r} = 1$ ,  $\mu_{2r} = -1$  and  $\tau_m = -1$ , the total transmission coefficient is  $T_m^T(|k_t| \rightarrow \infty) = 1$ .

The electrostatic limit predicts that the complete TE mode spectrum is transformed uniformly by the slab and leads to incorrect conclusions. Due to the difference between  $k_{1z}$  and  $k_{2z}$  in the terms of order  $k_t^{-2}$ , a cutoff for TE modes ( $k_{te}^c < k_{tm}^c < \infty$ ) also exists, which is obtained from (3.19) with  $\tau_m = -k_{1z}(k_{tm}^c)/k_{2z}(k_{tm}^c)$  as follows

$$k_{tm}^c = |(1/d) \ln \{2/(1 - k_{1z}(k_{tm}^c)/k_{2z}(k_{tm}^c))\}| > k_{te}^c. \quad (3.30)$$

### 3. METAMATERIAL SUPERLENS

	I	II	III	IV
	$\sigma = 10^{-4}$	$\sigma = 10^{-8}$	$\sigma = 0$	$\sigma = 0$
	$\Gamma = 10^{-10}$	$\Gamma = 10^{-10}$	$\Gamma = 10^{-10}$	$\Gamma = 10^{-20}$
$k_{te}^c/k_0$	5.62	10.47	12.60	19.82
$k_{tm}^c/k_0$	8.20	13.59	15.90	19.82

**Table 3.2:** Cutoff wavenumber  $k_{te,tm}^c/k_0$  for material parameters as given in (3.29).

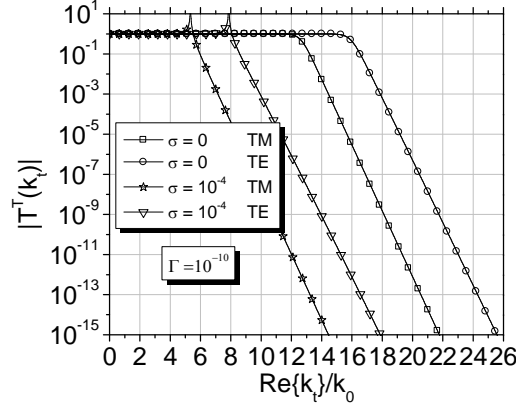


**Figure 3.12:**  $T^T(k_t)$  for a slab with material parameters as given in (3.29).

The same results hold for TM modes, if the permittivity remains unity and perturbations are applied to the permeability. In that case  $k_{tm}^c < k_{te}^c < \infty$ .

The total transmission factors for  $\Gamma = 10^{-10}$ ,  $\sigma = 0$  and  $\sigma = 10^{-4}$  are plotted in Fig. 3.12. A closer look at the case with  $\sigma = 0$  reveals that  $k_{tm}^c - k_{te}^c \approx 3k_0$ . The difference between the cutoff wave numbers leads to the unequal transmission of TE and TM modes through the slab. This mechanism of the image distortion can play a considerable role in the case of excitation of the slab with generally oriented sources. As shown in Tab. 3.2, the difference between  $k_{tm}^c$  and  $k_{te}^c$  vanishes as  $\epsilon_{2r} \rightarrow -1$ .

In the case of generally oriented sources, obtaining the exact field distribution in the vicinity of the image plane behind the slab becomes important. Two distinct excitations with longitudinal  $\mathbf{J}_0 = \hat{\mathbf{z}}$  and transverse  $\mathbf{J}_0 = \hat{\mathbf{x}}$  dipoles are investigated next. Perturbations with  $\sigma = 10^{-4}$  and  $\sigma = 0$  are considered. The dissipation factor is set to  $\Gamma = 10^{-10}$ .

The field intensities are evaluated in the  $xy$  (image plane) and  $yz$  planes behind the slab. The normalized intensity distribution is determined as

$$I_{\text{norm}}^{\text{xy}} = \frac{I(x, y, 0.4\lambda)}{I_{\text{max}}^{\text{xy}}} \quad \text{and} \quad I_{\text{norm}}^{\text{yz}} = \frac{I(0, y, z)}{I_{\text{max}}^{\text{yz}}}, \quad (3.31)$$

with

$$I_{\text{max}}^{\text{xy}} = \max \{I(|x| < 0.5\lambda, |y| < 0.5\lambda, 0.4\lambda)\} \quad (3.32)$$

and

$$I_{\text{max}}^{\text{yz}} = \max \{I(0, |y| < 0.5\lambda, 0.3\lambda < z < 0.5\lambda)\}.$$

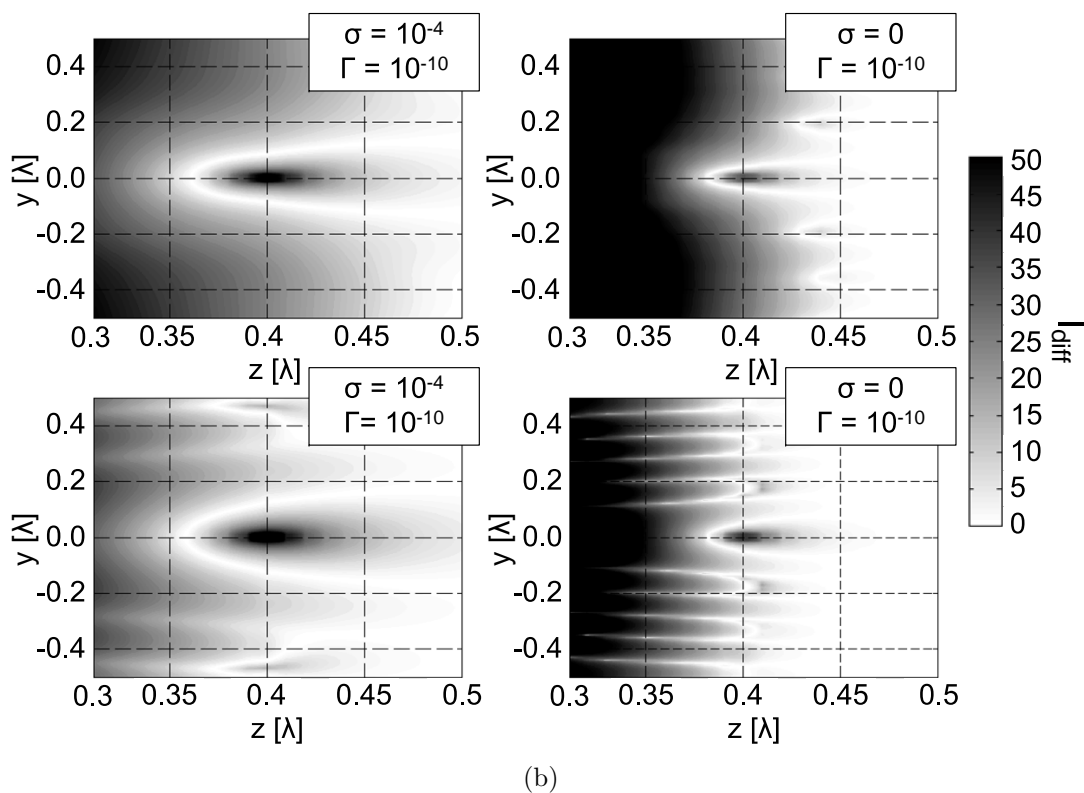
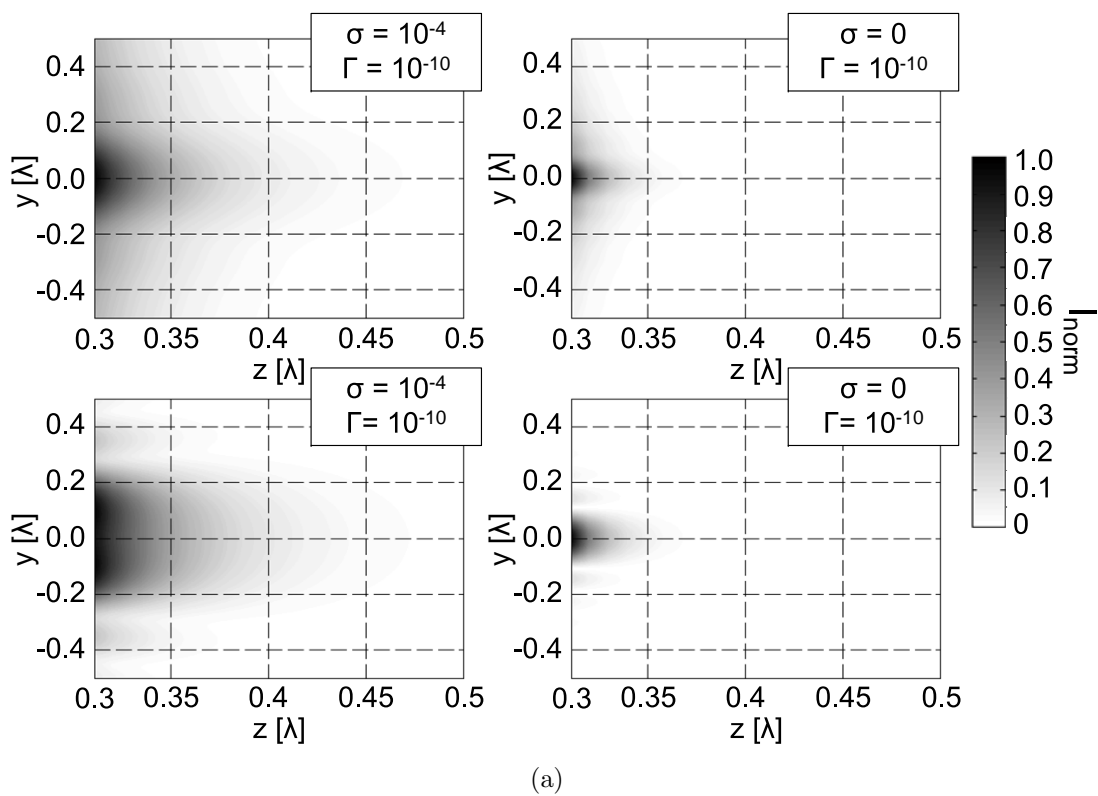


**Figure 3.13:** (a)  $I_{\text{norm}}^{yz}$  and (b)  $I_{\text{diff}}^{yz}$  for  $\mathbf{J}_0 = \hat{\mathbf{z}}$  (top row) and  $\mathbf{J}_0 = \hat{\mathbf{x}}$  (bottom row).

### 3. METAMATERIAL SUPERLENS

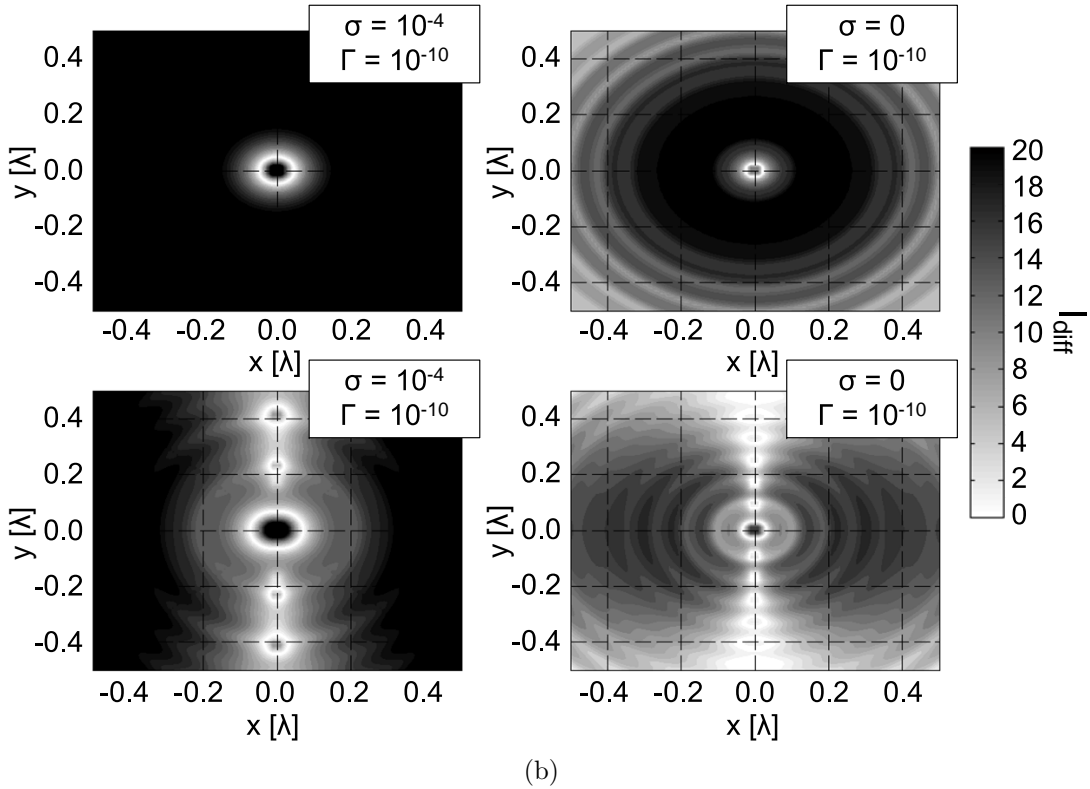
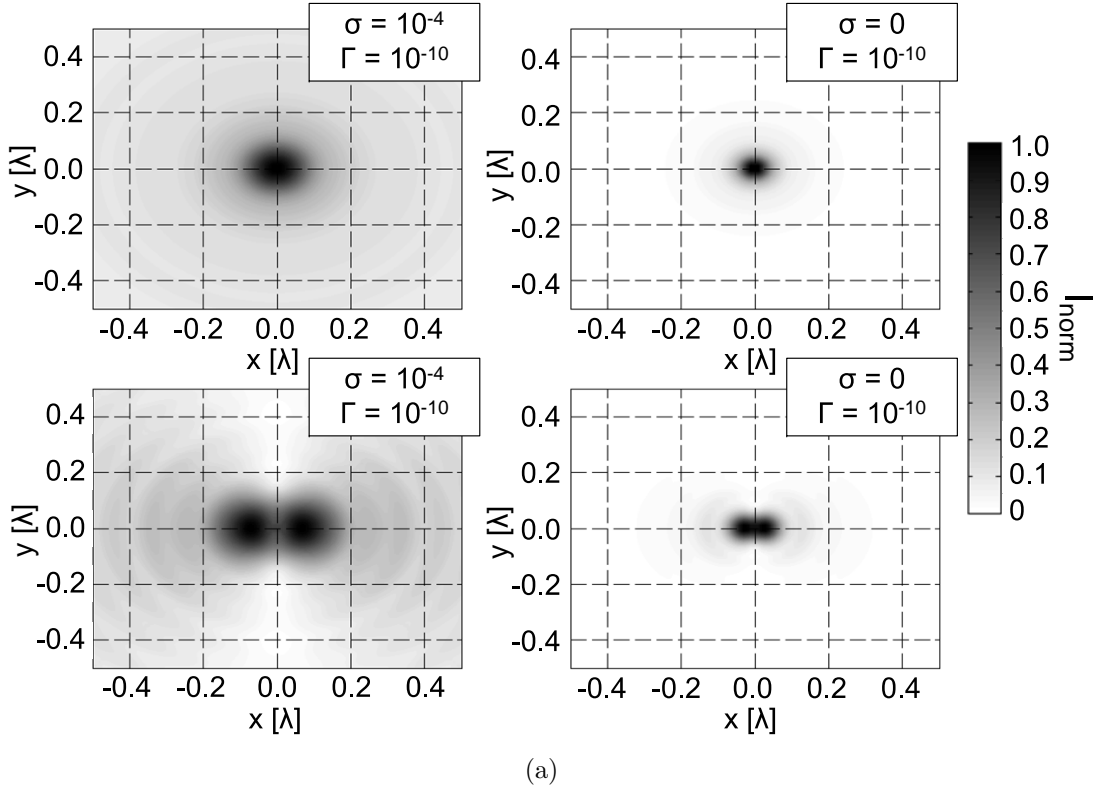


**Figure 3.14:** (a)  $I_{\text{norm}}^{\text{xy}}$  and (b)  $I_{\text{diff}}^{\text{xy}}$  at the image plane for  $\mathbf{J}_0 = \hat{\mathbf{z}}$  (top row) and  $\mathbf{J}_0 = \hat{\mathbf{x}}$  (bottom row).

Analogous to (3.25), in order to visualize the imaging capabilities of the slab more clearly, it is convenient to define the following parameter:

$$I_{\text{diff}}^{\text{xy, yz}} = \left| 20 \log \frac{|\mathbf{E}^{\text{xy, yz}}|}{|\mathbf{E}_{\text{D}}^{\text{xy, yz}}|} \right|, \quad (3.33)$$

with  $|\mathbf{E}_{\text{D}}|$  representing the field of a dipole located at  $z = 2d - |z_0| = 0.4\lambda$  and radiating in free space without the double negative slab. Remember that  $I_{\text{diff}} = 0$  indicates that the fields emitted by the source are transferred without distortion to the focal point behind the slab.

$I_{\text{norm}}^{\text{yz}}$  is plotted in Fig. 3.13(a). As expected, the intensity is at maximum at the slab-vacuum interface at  $z = 0.3\lambda$  and attenuates rapidly with increasing distance  $z$ . Irrespective of the type of excitation, approaching the ideal case by decreasing  $\sigma$  from  $10^{-4}$  to  $10^{-10}$ , localizes the maximum intensity in a small region around the optical axis and interface of the slab.

$I_{\text{diff}}^{\text{yz}}$  is plotted in Fig. 3.13(b). In the region  $0.3\lambda < z < 0.4\lambda$ , the intensity deviates strongly from that of a dipole located at  $z = 0.4\lambda$  and radiating in free space. The intensity mismatch increases as  $\sigma \rightarrow 0$ . For  $z \geq 0.4\lambda$  the intensity mismatch decreases with decreasing  $\sigma$ , confirming that in the ideal case  $\sigma = 0$  and  $\Gamma = 0$  the fields replicate themselves perfectly at the image plane.

The intensity distribution at the image plane is investigated next.  $I_{\text{norm}}^{\text{xy}}$  is plotted in Fig. 3.14(a). The central spot located at  $x = 0$  and  $y = 0$  is clearly visible for both types of excitation. As  $\sigma$  gets smaller - approaching the ideal case - the central spot shrinks, indicating the enhancement of the image. The resolution improvement is most clearly observed from  $I_{\text{diff}}^{\text{xy}}$  which is plotted in Fig. 3.14(b). The intensity mismatch in the vicinity of the focal point degrades as  $\sigma$  decreases.

### 3.6.4 Thickness of the Slab

The impact of the slab thickness on the total transmission factor  $T^{\text{T}}(k_t)$  and the image quality is considered. The source with  $\mathbf{J}_0 = \hat{\mathbf{z}}$  is fixed at  $z_0 = -0.2\lambda$  and the thickness of the slab is varied between  $0.2\lambda < d < 2\lambda$ . The slabs material parameters are chosen according to (3.21) with  $\Gamma = 10^{-10}$ . Remember that for this type of perturbation mechanism the TE and TM modes are transmitted equally by the slab so that  $T_e^{\text{T}}(k_t) = T_m^{\text{T}}(k_t) = T^{\text{T}}(k_t)$ . The image plane behind the slab is adjusted according to the focal point predicted by geometrical optics, i.e.  $z = 2d - |z_0|$ , and coincides with the second interface of the slab for  $d = 0.2\lambda$ .

The magnitude of  $T^{\text{T}}(k_t)$  for  $0.2\lambda < d < \lambda$  is plotted in Fig. 3.15(a). As indicated by (3.24),  $k_t^c$  decreases as the slab becomes thicker. In other words, the evanescent modes exhibit a lower cutoff and the resolution at the image plane degrades for increasing slab thickness.

The FWHM ( $\Delta y$ ) of the intensity pattern at the image plane as a function of  $d$  is plotted in Fig. 3.15(b). There is a significant resolution improvement for thin slabs with  $0.2\lambda < d < \lambda$ . The improvement becomes less significant as  $d > \lambda$ . Increasing

### 3. METAMATERIAL SUPERLENS

$d$  by  $\Delta d = 0.8\lambda$  from  $0.2\lambda$  to  $\lambda$ , enhances the resolution by  $\Delta y(0.2\lambda)/\Delta y(\lambda) = 5.2$ . An enlargement by the same amount from  $\lambda$  to  $1.8\lambda$ , on the other hand, yields a resolution improvement of only  $\Delta y(1.8\lambda)/\Delta y(\lambda) = 1.5$ .

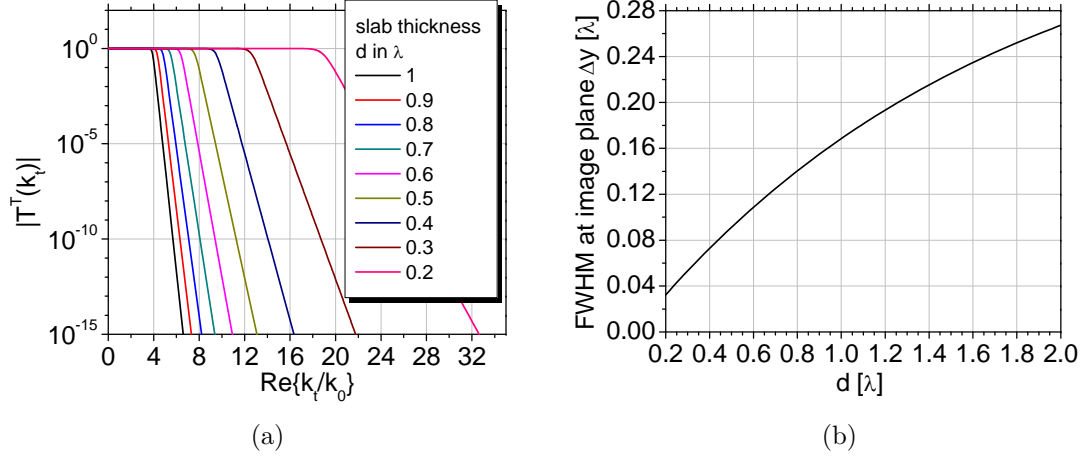


**Figure 3.15:** (a)  $|T^T(k_t)|$  for  $0.2\lambda < d < \lambda$  and (b) FWHM at image plane ( $x = 0$ ,  $y \neq 0$ ,  $z = 2d - |z_0|$ ) with source at  $z_0 = -0.2\lambda$ .

#### 3.6.5 Aperture Size

Theoretical investigations of imaging by a double negative slab have been based so far on the assumption that the slab has an infinite aperture and extends to infinity in the transversal plane ( $xy$  plane in Fig. 3.5). In reality the slab is always transversally limited and the lens has a finite aperture. In this case, physical phenomena like edge diffraction can negatively affect the image quality. The influence of the aperture size of a double negative metamaterial slab onto its imaging quality is investigated next [27].

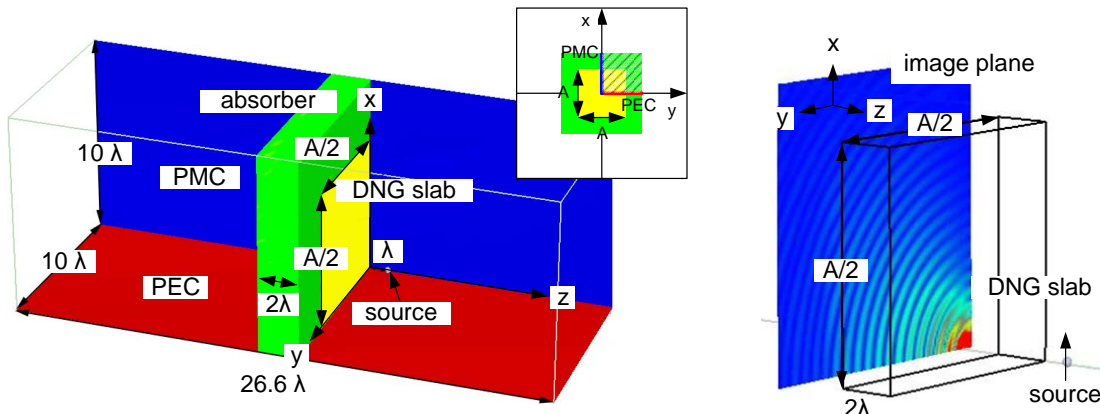


**Figure 3.16:** MEFiSto-3D Pro<sup>®</sup> simulation volume with  $d = 2\lambda$  and  $z_0 = -\lambda$  and image plane at  $z = 3\lambda$ .

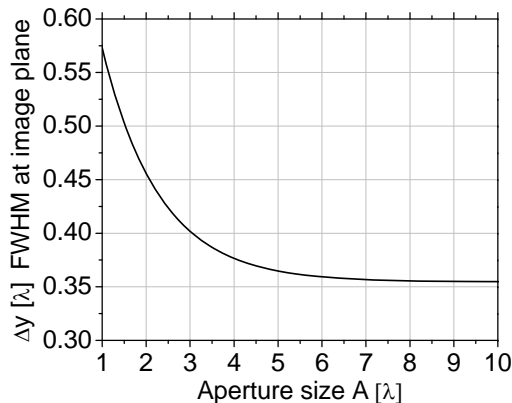


**Figure 3.17:**  $\Delta y$  vs. aperture size  $A$  at image plane.

A lossless and isotropic double negative slab, matched to free space ( $\epsilon_{2r} = \mu_{2r} = -1$ ) at 10 GHz is considered for this purpose. The slab has a thickness of  $2\lambda$  and is excited by a vertical electric dipole with  $\mathbf{J}_0 = \hat{\mathbf{x}}$  positioned at  $z_0 = -\lambda$ . The image plane is at  $z = 2d - |z_0| = 3\lambda$ . Simulations are carried out with MEFiSTo-3D Pro<sup>®</sup>[38]. The simulation volume has dimensions of approximately  $26 \times 10 \times 10 \lambda$  and is discretized with a  $\lambda/10$  symmetrical condensed node mesh. As shown on the left of Fig. 3.16, electric and magnetic walls are imposed on the  $yz$  and  $xz$  planes, respectively, which make it possible to restrict the simulation volume to a single quadrant. The double negative slab is surrounded by an absorber of the same thickness and the simulation volume is terminated with perfectly matched layer (PML) boundaries. All simulations are truncated after 1020 time steps.

The aperture size  $A$  of the slab is varied between  $1\lambda < A < 10\lambda$ . For each slab the image quality or resolution is determined from the FWHM value  $\Delta y$  of the intensity pattern at the image plane as shown on the right of Fig. 3.16. The results are plotted in Fig. 3.17. As expected,  $\Delta y$  decreases monotonically with increasing aperture size, indicating the resolution improvement. Resolution changes significantly for small apertures ranging between  $1\lambda < A < 4\lambda$  and it can be concluded that for slabs with  $A < 5\lambda$  the resolution improves significantly with increasing aperture size. Increasing  $A$  beyond this value has no significant effect.

It should be mentioned at this point that perfect resolution can never be reached in finite time, since the causality of the superlens response is ensured by the time delay in the transmission of the evanescent modes [46]. Especially when the lens is perfectly matched to the surrounding space, it takes an infinite time to reach steady state. The finite cell size (discretization) of the computational domain further restricts the resolution. A detailed discussion of these issues can be found in [51; 52; 56].

### 3.6.6 Excitation by Broadband Pulses

Theoretical investigations of imaging by a double negative slab have assumed so far excitation by monochromatic sources, where dispersion plays no role. In this section the effect of dispersion on the image quality is investigated.

### 3. METAMATERIAL SUPERLENS

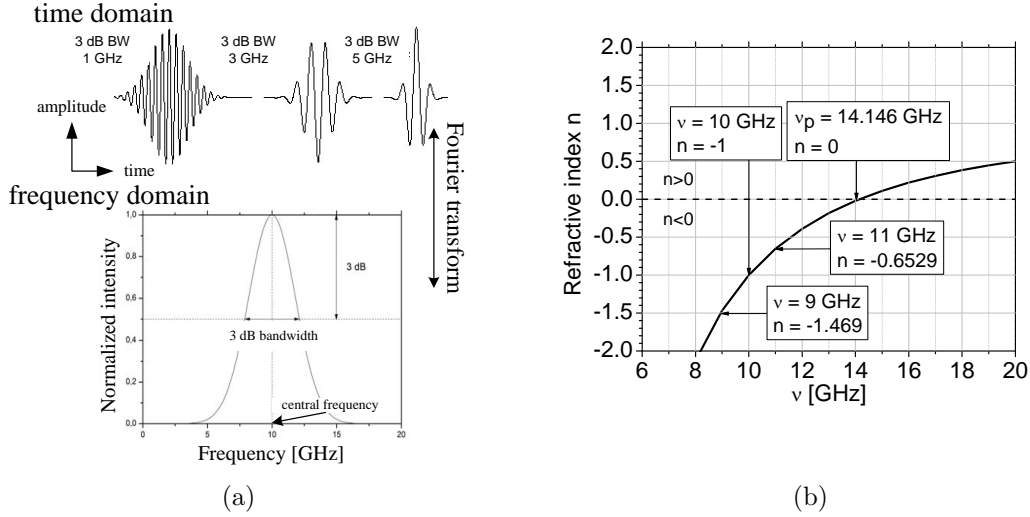


**Figure 3.18:** (a) Gaussian pulse in time and frequency domains and (b) Drude dispersive refractive index of the slab.

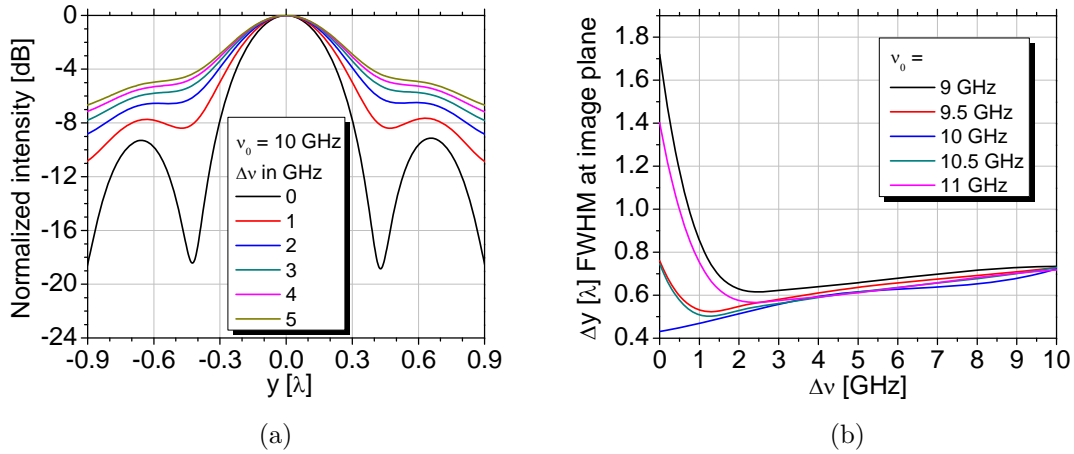


**Figure 3.19:** (a) Variation of the image plane field intensity with an excitation pulse having a central frequency of  $\nu_0 = 10$  GHz and 3dB bandwidth ranging from 0 to 5 GHz. (b) FWHM at image plane vs. pulse width  $\Delta\nu$  for pulses with central frequency  $\nu_0$ .

Imaging of short-time pulses with a Gaussian spectrum are considered (Fig. 3.18(a)). The slab is assumed to be Drude dispersive. Drude dispersion is preferred over Lorentz dispersion since it allows a broader frequency band with a negative refractive index. The simulations are carried out with MEFiSTo-3D Pro<sup>®</sup> [38], where CRLH Drude dispersive unit cells are modeled by matching an inter cell network to a standard 3D symmetrical condensed node (SCN) [112].

The Drude model parameters of the slab (2.25) are chosen so as to yield a refractive index of  $n = -1$  at the design frequency  $\nu_d = 10$  GHz ( $\omega_{pe} = \omega_{pm}$ ). The slab is assumed to be lossless ( $\Gamma_e = \Gamma_m = 0$ ). Its frequency dependent refractive index is plotted in Fig. 3.18(b). The slab has a thickness of  $d = 2\lambda$  and a transversal extension or aperture size of  $8\lambda$  at  $\nu_d$ . The simulation volume is similar to the one in Fig. 3.16.

The source is placed at a distance of  $\lambda$  in front of the slab. A broadband pulse with a Gaussian spectral distribution centered at  $\nu_0$  and a 3 dB bandwidth of  $\Delta\nu$  (Fig. 3.18(b)) is used throughout the simulations. Field monitors are positioned at the expected image plane, located at a distance of  $\lambda$  behind the slab. The intensity distribution is calculated by extracting the time averaged electric field intensities.

The image quality is determined from the FWHM value  $\Delta y$  at the image plane. The time averaged field intensities along the transversal axis in the image plane are plotted in Fig. 3.19(a). The curves show the results for excitation pulses with  $\nu_0 = 10$  GHz and spectral bandwidths  $\Delta\nu$  ranging between 0 and 5 GHz. Broadening the spectral width results in an increase of  $\Delta y$ , corresponding to a degradation of the image quality.

Furthermore, the center frequency is varied between  $9 \leq \nu_0 \leq 11$  GHz. The spot size  $\Delta y$  is plotted for various pulse widths and center frequencies in Fig. 3.19(b). The blue curve represents  $\Delta y$  for  $\nu_0 = \nu_D = 10$  GHz. Resolution reduces almost linearly with increasing pulse width  $\Delta\nu$ . For pulses with center frequencies  $\nu_0$  other than  $\nu_D$ , on the other hand, broadening the pulse width leads to an enhancement of the resolution until a maximum is reached. Contrary to the case of  $\nu_0 = \nu_D$  where resolution decreases linearly with increasing pulse width, for pulses with  $\nu_0 \neq \nu_D$  the resolution enhances until a bandwidth of  $\Delta\nu \approx 2|\nu_0 - \nu_D|$  is reached and decreases afterwards.

### 3. METAMATERIAL SUPERLENS

---

## 4

# Metamaterial Microwave Absorbers

The electromagnetic spectrum used for detection purposes extends from microwave and infrared up to visible frequencies. For microwave frequencies the detectability of a target is measured in terms of its radar cross section (RCS), which strongly depends on the targets size, shape and the material it is fabricated from. Among the most practical and commonly used radar cross section reduction (RCSR) techniques is the usage of radar absorbing materials (RAM). RAMs are principally based on the development of low reflection coatings (LRC), whose reflectivity for electromagnetic waves in the frequency range of interest is small. Common types of RAMs are Salisbury, Jaumann and Dallenbach absorbers [64; 94].

A Salisbury screen consists of a resistive sheet placed an odd multiple of quarter wavelengths in front of a metal backing separated by a dielectric. In terms of transmission line theory, the quarter wavelength transmission line transforms the short circuit at the conductor into an open circuit at the resistive sheet, so that the overall input impedance of the structure becomes the sheet resistance. Reflection is completely suppressed if the sheet resistance is matched to free space. A Salisbury screen is narrow banded. Improved performances over broader range of frequencies is obtained by combining multiple layers, yielding the Jaumann absorber. Another type of absorber is the Dallenbach layer, which is composed of a homogeneous lossy layer and low reflectivity is achieved through adjusting the layers permittivity and permeability. Impedance matching is used to reduce reflection at the air-absorber interface and electromagnetic waves are absorbed as they penetrate into the lossy layer.

Adjusting the electromagnetic specifications of the absorber to the given application is an important task during the design process. The limited choice of naturally occurring materials with suitable dielectric and magnetic properties constitutes thereby a major challenge. The fulfillment of low reflectivity for broad range of frequencies, incidence angles and polarizations are important design factors in the development of absorbers. Many applications require electrically thin, easily applicable and robust absorbers. In recent years, artificial electromagnetic materials or metamaterials have been effectively employed in the design of novel absorbers at microwave frequencies [20; 33; 77].

## 4. METAMATERIAL MICROWAVE ABSORBERS

---

In the first part of this chapter, the possibility of realizing planar and electrically thin Dallenbach like absorbers with dispersive and resonant metamaterials is analyzed. The metamaterial absorber consists of a single layer strip-SRR or CLS-SRR metamaterial. Designs operating in the Ku band (12 - 18 GHz) are proposed and methods for adjusting the absorbers permittivity and permeability to reduce reflectivity at a specific frequency are given. The extracted effective material parameters in Sec. 2.10 are thereby employed.

In the second part, a systematic way of designing a truly planar metamaterial absorber consisting of a 2D periodic arrangement of capacitively loaded strips (CLS) is presented and its applicability in the realization of electrically thin low reflection coatings is investigated.

Though designed to operate at a single frequency and at a particular incidence angle, metamaterial coatings of this kind, in fact, function over a broader range of frequencies and incidence angles. Already simplest absorbers with a thickness of  $\lambda/80$  have relative bandwidths of about 3 %, and various approaches to widening the bandwidth and improving the absorption rate at the operation frequencies are under development. Furthermore, such coatings have the additional advantage of being realizable in planar technology.

### 4.1 Drude and Lorentz Dispersive Microwave Absorbers

In this section, the possibility of realizing planar and electrically thin absorbers assembled from a single layer strip-SRR or CLS-SRR metamaterial is investigated. Designs operating in the Ku band (12 - 18 GHz) are proposed. The electromagnetic response of the metamaterial absorber is described by an effective medium model (Sec. 2.10) with Lorentz and/or Drude dispersion. For a layer with predetermined permeability, a condition for reducing reflection at a specific frequency and a method for tuning its permittivity to the required value are given. The effective response of the absorber is adjusted by suitably choosing, combining and dimensioning the inclusions/unit cells constituting the metamaterial. The outlined procedure can be regarded as a fundamental step in the design of metamaterial absorbers at microwave frequencies.

#### 4.1.1 Principles of Operation

As shown in Fig. 4.1(a), absorbers consisting of a planar metamaterial layer backed by a metallic ground are considered. The absorber extends from  $z = 0$  to  $z = d$  and has a refractive index of  $n_1 = \sqrt{\epsilon_r \mu_r}$ . A TEM plane wave propagating through free space with an impedance of  $\eta_0 = \sqrt{\epsilon_0/\mu_0} = 377 \Omega$  and incident perpendicularly upon the layer with  $\eta_1 = \sqrt{\mu_r/\epsilon_r} \eta_0$  is reflected according to (A.13) as

$$R = \frac{j\eta_1 \tan \alpha - \eta_0}{j\eta_1 \tan \alpha + \eta_0}, \quad (4.1)$$

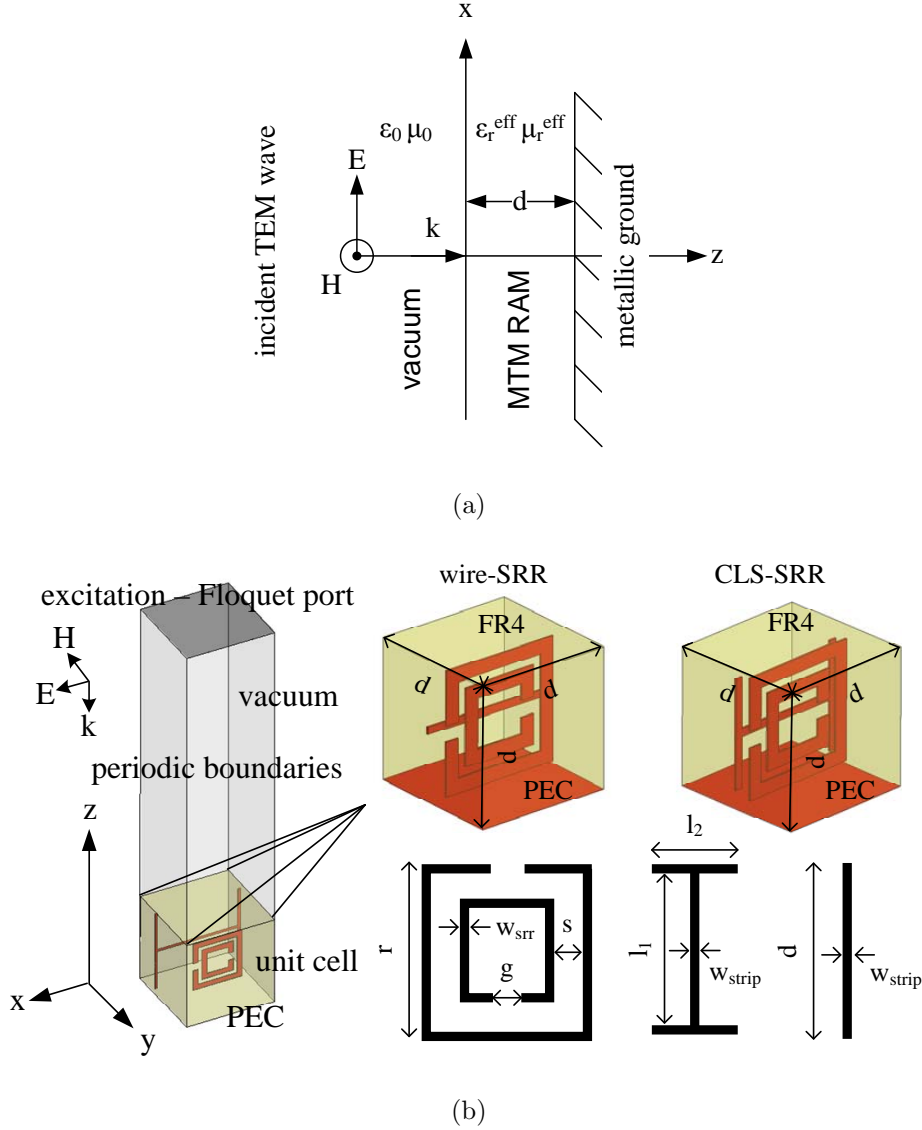


**Figure 4.1:** (a) General absorber backed by a metallic ground and (b) realization in terms of metallic strip, CLS and SRR inclusions.

with  $\alpha = n_1 k_0 d$  the electrical thickness of the layer and  $k_0 = 2\pi/\lambda$ . The condition for zero reflection is obtained by setting  $R = 0$  and is given by

$$1 - \sqrt{\frac{\mu_r}{\epsilon_r}} \tanh \left[ \frac{2j\pi d}{\lambda} \sqrt{\mu_r \epsilon_r} \right] = 0. \quad (4.2)$$

As seen from the equation above, zero reflection requires a material with appropriate values of  $\epsilon_r$  and  $\mu_r$ , making the utilization of metamaterials highly feasible. Remember that metamaterials appear homogeneous for electromagnetic waves if the unit cells or inclusions they are composed of are electrically small. As discussed in Sec. 2.9 and 2.10, metamaterials can then be homogenized and their properties can be described by dispersive effective material parameters  $\epsilon_r^{\text{eff}}(\omega)$  and  $\mu_r^{\text{eff}}(\omega)$ . By a suitable

## 4. METAMATERIAL MICROWAVE ABSORBERS

---

choice, combination and dimensioning of the inclusions, the effective material parameters of metamaterials can be adjusted to satisfy (4.2), providing multiple degrees of freedom during the design process.

In resonant metamaterials composed of conducting strip, CLS and SRR inclusions the electric and magnetic polarizabilities are tuned separately. The strips or CLSs are responsible for the electric and the SRRs for the magnetic polarizability. Hence, controllability of resonant frequencies of the inclusions is needed to ensure an optimal overlapping of the electric and magnetic resonance frequency regimes.

In the following, this property is used to design metamaterial absorbers composed of strip-SRR or CLS-SRR inclusions. The absorbers are described by the effective material parameters obtained from the homogenization procedure in Sec. 2.10 and their effective response is optimized by suitably choosing, combining and dimensioning the unit cell composition of the metamaterial. The designs are then verified through full wave simulations of the realistic structure with HFSS<sup>®</sup>.

As shown in Fig. 4.1(b), the simulation model is based on a unit cell and is terminated with periodic boundary conditions on the side walls, whereby it is assumed that the absorber extends to infinity in the  $xy$  plane. The reflection response for plane wave excitation with  $E_x, H_y, k_z$  is evaluated at a wave (Floquet) port, located at a distance of  $2\lambda$  above the absorber. The simulation volume is terminated at the bottom by a metallic ground plane (PEC). The inclusions constituting the metamaterial are modeled by  $35 \mu\text{m}$  thick copper and are immersed in a dielectric host of permittivity  $\epsilon_r^h$  and a loss tangent  $\tan \delta$ .

### 4.1.2 Realization

Let us consider a single layer strip-SRR metamaterial absorber. For this type of metamaterial it is well known that permittivity and permeability are subject to Drude and Lorentz dispersion, respectively.

We will start our analysis by specifying a frequency range at which a reduction in reflection is desired. Let us assume for instance that  $13 < \nu_i < 14$  GHz, where  $\nu_i$  is the frequency of interest. As a first step, it has to be ensured that the magnetic resonance frequency  $\nu_{0m}$  of the SRR lies in the frequency range of interest. The next step consists of obtaining  $|R(\nu_i)| = 0$  by adjusting  $\nu_{pe}$ , which is achieved through varying the strip width  $w_{strip}$ .

According to the retrieved effective material parameters in Sec. 2.10, unit cell compositions satisfying these requirements could be as follows:

- SRRs with dimensions of  $w_{srr} = 0.2$  mm,  $r = 1.4$  mm,  $g = 0.1$  mm and  $s = 0.1$  mm, ensuring that the magnetic resonance frequency is in the frequency range of interest ( $13 < \nu_i < 14$  GHz)
- Strips with widths from  $w_{strip} = 0.1$  mm to  $w_{strip} = 0.6$  mm, so that the electric plasma frequency varies between  $26.9 < \nu_{pe} < 36.3$  GHz
- A unit cell size of  $d = 2.5$  mm and a distance between strip and SRR inclusions of  $0.25$  mm

## 4.1 Drude and Lorentz Dispersive Microwave Absorbers

- Host material of standard FR4 with  $\epsilon_r^h = 4.4$  and  $\tan \delta = 0.02$

The extracted Drude and Lorentz model parameters are provided in Tab. 4.1. It is seen that  $\nu_{pe}$  shifts to higher frequencies as  $w_{strip}$  increases. The remaining parameters stay almost constant, so that they are replaced by following averages:

$$\epsilon_r^{av}(\infty) = 4.7, \mu_r^{av}(\infty) = 1.1, \Gamma_e^{av} = 1.2, \nu_{pm}^{av} = 4.3, \nu_{m0}^{av} = 13.3 \text{ and } \Gamma_m^{av} = 2.2$$

Together with  $\nu_{pe}$ , these averages are then plugged into (2.25) and (2.24) to determine the effective material parameters of the metamaterial layer. The reflection coefficient of the absorber is then obtained from (4.1). As stated previously, the aim is to obtain  $|R(\nu_i)| = 0$  in the frequency range of interest  $\nu_i$  by adjusting  $\nu_{pe}$ .

Assuming that  $\nu_{pe}$  varies between 20 and 50 GHz, the magnitude of the reflection coefficient for  $13 < \nu_i < 14$  GHz is plotted in Fig. 4.3. It is seen that  $|R(\nu_i)|$  is at minimum in the vicinity of  $\nu_{pe} \approx 35$  GHz and  $\nu_i \approx 13.6$  GHz. According to the design proposals in Tab. 4.1, maximum amount of reduction in reflection is therefore obtained with configurations III or IV.

The frequency dependent behavior of  $|R(\nu)|$  for these configurations is shown in Fig. 4.4 by the solid lines. The dotted lines represent full wave simulations of the realistic structure with HFSS<sup>®</sup>. Both results are in good agreement and it can be concluded that the metamaterial absorber is accurately characterized by effective material parameters.

	(mm)		(GHz)					
	$w_{strip}$	$\epsilon_r(\infty) \mu_r(\infty)$	$\nu_{pe}$	$\Gamma_e$	$\nu_{pm}$	$\nu_{m0}$	$\Gamma_m$	
I	0.10	4.8 1.0	26.9	1.3	4.1	13.2	2.2	
II	0.20	4.7 1.0	29.5	1.6	4.2	13.2	2.0	
III	0.40	4.7 1.2	33.3	1.4	4.3	13.3	1.9	
IV	0.60	4.5 1.1	36.3	0.5	4.5	13.4	2.8	

**Table 4.1:** Drude-Lorentz model parameters for strip-SRR metamaterial absorber.

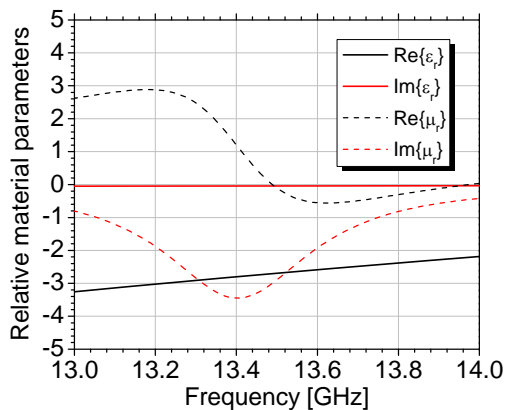


**Figure 4.2:** Extracted effective material parameters for config. IV in Tab. 4.1.

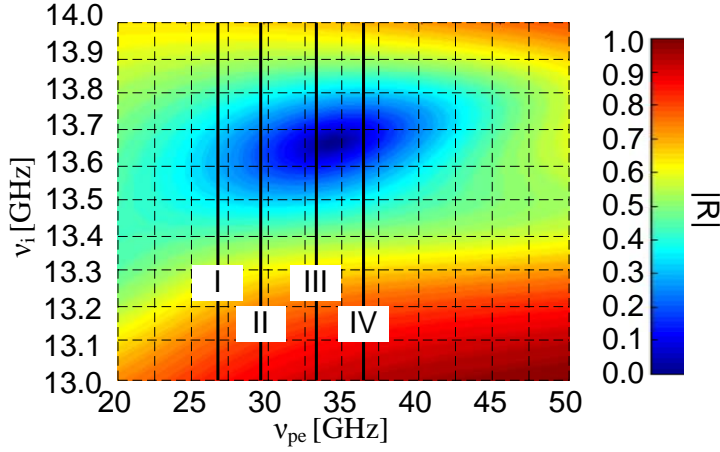


**Figure 4.3:** Plot of  $|R| = 0$  as a function of  $\nu_{pe}$  and  $\nu_i$ .

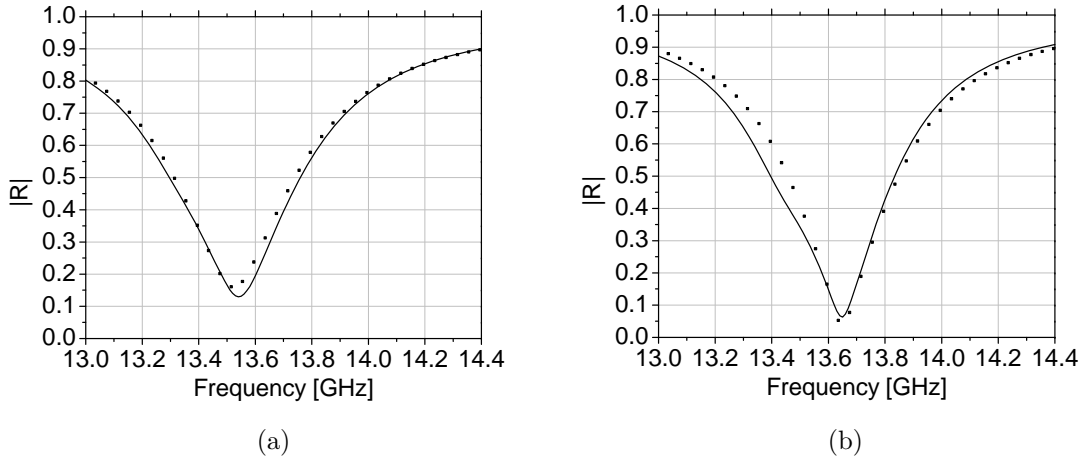


**Figure 4.4:**  $|R|$  for configurations (a) III and (b) IV in Tab. 4.1 obtained with effective medium approach (solid line) and full wave simulation (dotted line).

For configuration IV,  $|R| = 0.06$  at  $\nu_i = 13.65$  GHz. Compared to a purely metallic surface with  $|R| = 1$  (0 dB), reflectivity is reduced by 25 dB and only 0.36% of the incident energy is reflected back. The absorber has an electrical thickness and a unit cell size of approximately  $0.1\lambda$ . The effective material parameters of the metamaterial are  $\epsilon_r = -2.5 - j0.04$  and  $\mu_r = -0.6 - j1.5$  (Fig. 4.2) at  $\nu_i = 13.65$ . The reflection coefficient remains below 0.5 (-6dB) for frequencies between  $\nu_l = 13.4$  GHz and  $\nu_u = 13.8$  GHz, yielding a relative -6 dB bandwidth

$$\text{relative -6 dB bandwidth (in \%)} = \frac{\nu_u - \nu_l}{\nu_i} \times 100 \quad (4.3)$$

of 3%.

It is possible to replace the strips by CLS. The permittivity changes thereby from Drude to Lorentz type dispersion and the electric resonance frequency  $\nu_{0e}$  has to be optimized additionally in this case. A detailed investigation of metamaterials with CLS-SRR unit cells has been given in Sec. 2.10. Furthermore, absorbers composed

## 4.1 Drude and Lorentz Dispersive Microwave Absorbers

of double Lorentz dispersive metamaterials have been analyzed and a method for optimizing the material parameters has been worked out in [24].

Two distinct CLS inclusions with

- Configuration I:  $l_1 = 2.7$  mm,  $l_2 = 2.6$  mm and  $w_{strip} = 0.1$  mm
- Configuration II:  $l_1 = 2.3$  mm,  $l_2 = 2.3$  mm and  $w_{strip} = 0.1$  mm

are considered. The physical dimensions of the SRR inclusions and unit cell parameters are the same as those in the case of the strip-SRR metamaterial. Only the unit cell size is enlarged from  $d = 2.5$  mm to  $d = 3$  mm.

The extracted Lorentz-Lorentz dispersive model parameters and the corresponding reflection curves are provided in Tab. 4.2 and Fig. 4.5, respectively.

	(mm)		(GHz)							
	$l_1$	$l_2$	$\epsilon_r(\infty)$	$\mu_r(\infty)$	$\nu_{pe}$	$\nu_{pm}$	$\nu_{0e}$	$\nu_{0m}$	$\Gamma_e$	$\Gamma_m$
I	2.7	2.6	4.2	1.2	20.3	3.5	7.2	13.1	1.4	2.1
II	2.3	2.3	4.0	1.5	18.2	3.9	10.9	13.3	1.4	1.8

**Table 4.2:** Lorentz-Lorentz model parameters for CLS-SRR metamaterial absorber.

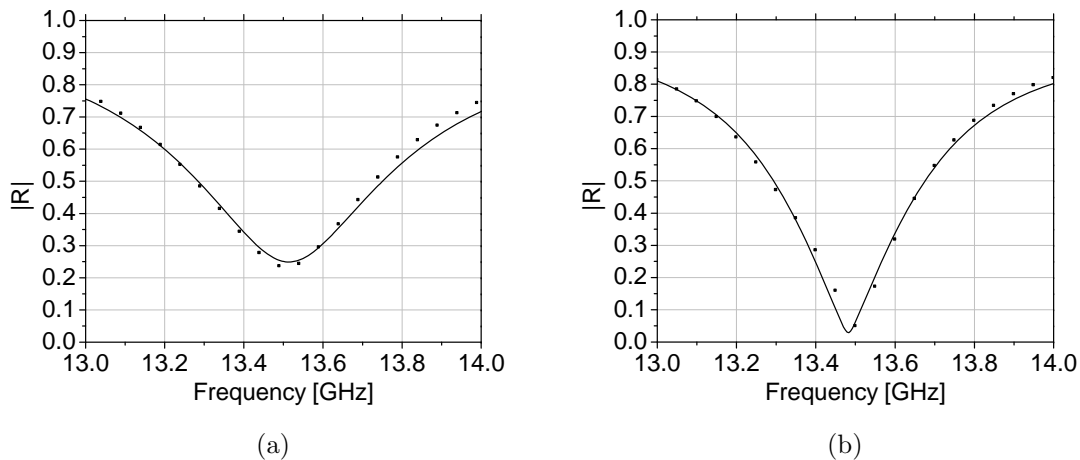


**Figure 4.5:**  $|R|$  for configurations (a) I and (b) II in Tab. 4.2 obtained with effective medium approach (solid line) and full wave simulation (dotted line).

Maximum reduction in reflection is obtained with configuration II and is  $|R| = 0.03$  at  $\nu_i = 13.48$  GHz. The effective material parameters of the metamaterial are  $\epsilon_r = -1.5 - j0.25$  and  $\mu_r = -0.3 - j1.5$  at this frequency and the absorber has an electrical thickness of  $0.14\lambda$ . The agreement between the effective medium approach and full wave simulations of the realistic structure is again very good.

Before closing this section, it has to be mentioned that the inclusions investigated in this section provide an anisotropic response and operate only for a specific polarization ( $E_x, H_y, k_z$  in Fig. 4.1(b)), restricting the operation of the absorber. This problem can be overcome by using one of the isotropic inclusions described at the end

of Sec. 2.7. On the other hand, a single 2D periodic array of capacitively loaded strips can be employed more efficiently in the realization of truly planar metamaterial low reflection coatings. This concept is investigated in the following section.

### 4.2 Metamaterial Low Reflection Coatings

In recent years, metamaterials have been employed in the design of electrically thin low reflection coatings at microwave frequencies [20; 33; 77]. In contrast to the Drude and Lorentz dispersive metamaterial absorbers investigated in the previous section, metamaterial low reflection coatings have the advantage of being entirely realizable in planar technology and are much thinner. A significant amount of weight reduction is thereby achieved, which is an important issue in many applications.

In its most general form, a metamaterial low reflection coating (MTM-LRC) is composed of a 2D periodic array of sub-wavelength sized inclusions printed on a substrate. They differ from frequency selective surfaces (FSS) [85] in that the size of inclusions in MTM-LRCs is significantly smaller than the wavelength. In conventional FSS with unit cell sizes comparable to the wavelength, grating lobes can emerge during the reflection process, leading to undesirable reflection at specific frequencies and incidence angles. Furthermore, MTM-LRCs have the advantage of being frequency scalable. Their performance and electromagnetic specification can be adjusted by a suitable choice and combination of durable materials such as Teflon, ceramic or fiber/resin mixtures. They can withstand high mechanical stress and due to their flexibility can be applied to curved surfaces.

In this section, MTM-LRCs composed of metallic arrays of capacitively loaded strip (CLS) inclusions are investigated. An equivalent circuit model based on coupled microstrip line theory is used to characterize their electromagnetic response. The designs are then verified through unit cell based full wave simulations of the realistic structures with HFSS<sup>®</sup>. Optimization procedures to adjust their performances are given. A coating with a unit cell size of  $\lambda/6$  and an overall thickness of  $\lambda/80$  at its operation range lying in the Ka-band (30 - 40 GHz) is designed and fabricated. Applied on top of a metallic surface the coating reduces reflectivity by approximately 10 dB at a center frequency of 36.925 GHz. In order to demonstrate its applicability in radar cross section reduction of finite sized objects, mono- and bistatic RCS measurements of a metallic cube with an edge length of  $6\lambda$  and coated with the developed coating are carried out. The experimental results are verified by conducting additional simulations with HFSS<sup>®</sup> and an in-house tool BISTRO, in which case the coating is described by an effective surface impedance and modeled with an impedance boundary condition.

#### 4.2.1 Principles of Operation

As shown in Fig. 4.6(a), the MTM-LRC is assembled from three layers consisting of a periodic array of CLS inclusions placed at a distance  $a_z$  in front of a metallic ground. The medium in between is filled with a dielectric of relative permittivity  $\epsilon_r$ . The

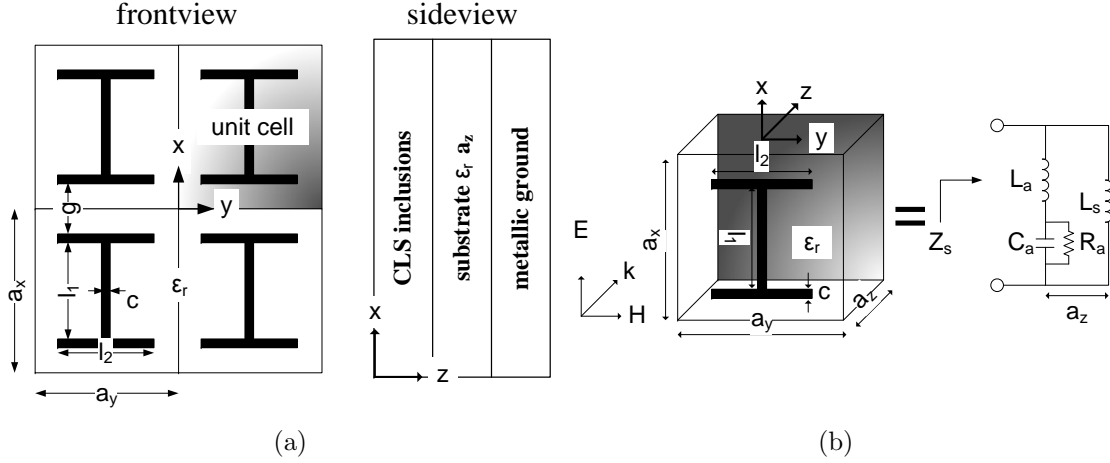


**Figure 4.6:** (a) Composition of the metamaterial low reflection coating (MTM-LRC) with capacitively loaded strip (CLS) inclusions, and (b) equivalent circuit model for TEM wave excitation with  $E_x$ ,  $H_y$ ,  $k_z$ .

size of a unit cell is given by  $a_x$  and  $a_y$ . The dimension of a single CLS inclusion is determined by its vertical ( $l_1$ ) and lateral ( $l_2$ ) armlengths, each being strips of width  $c$ .

The 2D CLS array acts analogous to an LC oscillator. Impinging electromagnetic waves induce currents on the inclusions. The metallic strips are inductive, which together with the gap capacitances between contiguous elements creates a series combination of inductors and capacitors. The lateral arms provide additional loading, increasing the overall capacitance. This is needed to keep the unit cell dimension at a sub-wavelength scale, i.e.  $a_x$  and  $a_y \ll \lambda$ . Resistivity is added to the structure by using patches with finite and variable conductivities, providing ohmic losses, or by using a lossy dielectric spacer.

It is possible to describe the electromagnetic response of the coating in terms of a frequency dependent effective surface impedance  $Z_s(\nu) = G(\nu) + jX(\nu)$ , composed of a resistive ( $G$ ) and a reactive ( $X$ ) part. The reflection coefficient is given by

$$R(\nu) = \frac{Z_s(\nu) - \eta_0}{Z_s(\nu) + \eta_0}, \quad (4.4)$$

with  $\eta_0 \approx 377 \Omega$  the free space impedance. The condition  $|R(\nu)| = 0$  requires that the surface impedance of the coating is perfectly matched to that of free space, i.e.  $G(\nu) = \eta_0$  and  $X(\nu) = 0$ . In the following section the surface impedance will be determined with the help of an equivalent circuit model based on coupled microstrip line theory [9].

### 4.2.2 Equivalent Circuit Model

The equivalent circuit model (Fig. 4.6(b)) is based on coupled microstrip line theory and is valid only for quasi TEM modes with  $E_x$ ,  $H_y$ ,  $k_z$ . The following closed form ex-

#### 4. METAMATERIAL MICROWAVE ABSORBERS

---

pressions for the characteristic impedance  $Z_0$  and effective relative dielectric constant  $\epsilon_{re}$  of a microstrip transmission line are found in Chapter 14 of [9]:

$$Z_0 = \begin{cases} \frac{\eta_0}{2\pi\sqrt{\epsilon_{re}}} \ln \left\{ \frac{8a_z}{c} + 0.25 \frac{c}{a_z} \right\} & \frac{c}{a_z} \leq 1 \\ \frac{\eta_0}{\sqrt{\epsilon_{re}}} \left\{ \frac{c}{a_z} + 1.393 + 0.667 \ln \left( \frac{c}{a_z} + 1.444 \right) \right\}^{-1} & \frac{c}{a_z} \geq 1, \end{cases} \quad (4.5)$$

$$\epsilon_{re} = \frac{\epsilon_r + 1}{2} + \frac{\epsilon_r - 1}{2} F \left( \frac{c}{a_z} \right) \quad (4.6)$$

and

$$F \left( \frac{c}{a_z} \right) = \begin{cases} \left( 1 + \frac{12a_z}{c} \right)^{-1/2} + 0.041 \left( 1 - \frac{c}{a_z} \right)^2 & \frac{c}{a_z} \leq 1 \\ \left( 1 + \frac{12a_z}{c} \right)^{-1/2} & \frac{c}{a_z} \geq 1. \end{cases} \quad (4.7)$$

The capacitance due to the gap of width  $g = a_x - l_1 - 2c$  between two adjacent CLS inclusions is estimated as the odd-mode capacitance of a coupled microstrip line, as described in Sec. 14.3.2 of [9], and is composed of four parts

$$C_a = (C_p + C_g + C_d + C_f) \frac{l_2}{2}. \quad (4.8)$$

In order to account for lossy substrates  $C_a$  is allowed to be complex, i.e.  $C_a = C'_a - jC''_a$ . The first term represents the parallel plate capacitance between the strip and ground plane and is given by

$$C_p = \epsilon_0 \epsilon_r \frac{c}{a_z}. \quad (4.9)$$

The second term describes the gap capacitance in air as

$$C_g = \begin{cases} \frac{\epsilon_0}{\pi} \ln \left\{ 2 \frac{1+\sqrt{m'}}{1-\sqrt{m'}} \right\} & 0 \leq k \leq 0.707 \\ \pi \epsilon_0 / \ln \left\{ 2 \frac{1+\sqrt{m}}{1-\sqrt{m}} \right\} & 0.707 \leq k \leq 1 \end{cases}. \quad (4.10)$$

where  $m = \frac{g}{g+2c}$ ,  $m' = \sqrt{1-m^2}$  and  $g = a_x - l_1 - 2c$  is the gap between two adjacent inclusions. The capacitance  $C_d$  due to the electric flux inside the substrate is estimated by

$$C_d = \frac{\epsilon_0 \epsilon_r}{\pi} \ln \coth \left( \frac{\pi g}{4a_z} \right) + 0.65 C_f \left\{ \frac{0.02 a_z \sqrt{\epsilon_r}}{g} + \left( 1 - \frac{1}{\epsilon_r^2} \right) \right\}. \quad (4.11)$$

$C_f$  denotes the fringe capacitance at the outer edge of the lateral ( $l_2$ ) strips and is given by

$$C_f = 0.5 \left\{ \frac{\sqrt{\epsilon_{re}}}{c_0 Z_0} - \frac{\epsilon_0 \epsilon_r c}{a_z} \right\}. \quad (4.12)$$

The inductive part  $L_a$  of a CLS is determined according to the width and length of  $l_1$  (Equation 2.39 in [9]) as

$$L_a = \frac{Z_0 \sqrt{\epsilon_{re}}}{c_0} l_1. \quad (4.13)$$

Finally, for thin layers with  $a_z \ll \lambda$ , the inductance at the termination of the transmission line with a ground plane is approximated by

$$L_s = \mu_0 a_z. \quad (4.14)$$

The overall surface impedance  $Z_s(\nu) = G(\nu) + jX(\nu)$  is given by a series combination of  $L_a$  and  $C_a$  which is connected in parallel with  $L_s$

$$Z_s(\nu) = (j\omega L_s) \parallel \left( j\omega L_a + \frac{1}{j\omega C_a} \right). \quad (4.15)$$

The reflection coefficient is then obtained from (4.4). The resonance frequency is given by

$$\nu_{res} = 1/\sqrt{L_a C_a}. \quad (4.16)$$

### 4.2.3 Design Example

A design operating in the Ka-band (30 - 40 GHz) is proposed. The unit cell composition is as follows:  $a_x = a_y = 1.4$  mm,  $l_1 = 0.9$  mm,  $l_2 = 0.8$  mm and  $c = 0.1$  mm. A lossy dielectric (standard FR4) with  $\epsilon_r = 4.4$ ,  $\tan \delta = 0.02$  and thickness  $a_z = 0.1$  mm is used as the dielectric spacer. The effective surface impedance  $Z_s(\nu)$  is determined from the equivalent circuit model and the reflection response  $R(\nu)$  is obtained afterwards from (4.4).  $|R(\nu)|$  and  $Z_s(\nu)$  are plotted in Fig. 4.7 (a) (solid line) and (b) (solid and dashed line), respectively.

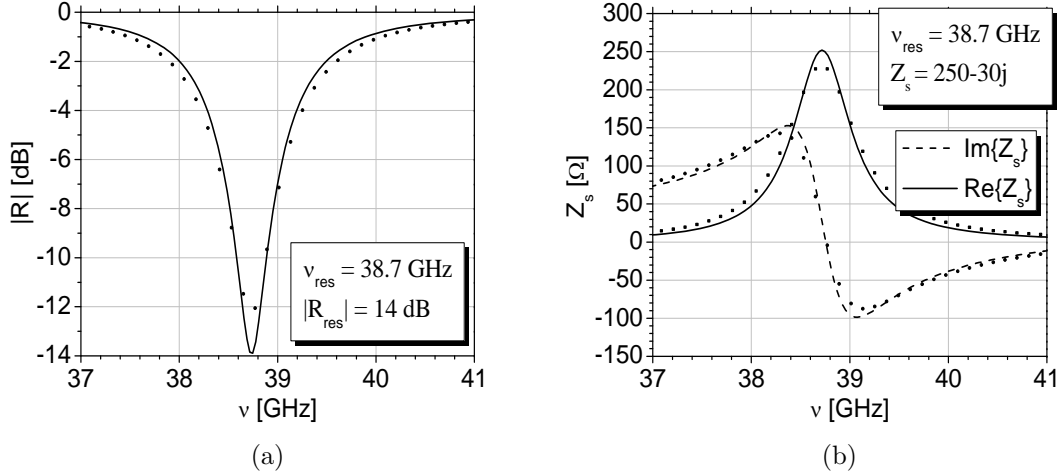


**Figure 4.7:** (a)  $|R(\nu)|$  and (b)  $Z_s(\nu)$  for the MTM-LRC described in Sec. 4.2.3. Results obtained with equivalent circuit model (solid, dashed line) and full wave simulation (dotted line).

The design is then verified through full wave simulations of the realistic structure with HFSS<sup>®</sup>, where the simulation model is based on a unit cell and it is assumed that the coating extends to infinity in the  $xy$  plane. The simulation volume is shown in the left side of Fig. 4.11 and is terminated by a pair of PEC and PMC boundaries at the sidewalls. The reflection response for TEM wave incidence is obtained at the excitation (Floquet) port located at a distance of  $2\lambda$  above the coating. The simulation volume is terminated with a metallic ground plane on the bottom. The CLS inclusions and ground plane are modeled by  $5 \mu\text{m}$  thick copper. The simulation results are plotted by the dotted lines in Fig. 4.7 and are in good agreement with the equivalent circuit model data.

Reflectivity is reduced by approximately 14 dB at  $\nu = 38.7$  GHz, where the unit cell size and the layer thickness are on the order of  $\lambda/6$  and  $\lambda/80$ , respectively.

#### 4.2.4 Optimization and Tuning

Methods for optimizing and tuning the reflection response of MTM-LRCs composed of CLS inclusions are discussed next. The amount of reflection from the coating is primarily determined by the effective surface impedance  $Z_s(\nu) = G(\nu) + jX(\nu)$  (4.15). According to (4.4)  $|R(\nu)| = 0$  when  $Z_s(\nu) = \eta_0$ .

As shown in Fig. 4.7(b),  $Z_s$  is entirely reactive except in a narrow region near  $\nu_{res}$ . It is inductive for  $\nu < \nu_{res}$  and capacitive for  $\nu > \nu_{res}$ . In the vicinity of  $\nu_{res}$  the reactive part passes through zero, such that  $X(\nu_{res}) \approx 0$ , and the amount of reduction in reflection is primarily determined by the resistive part  $G(\nu_{res})$ .

Therefore, in order to reduce the amount of reflection at a specific frequency  $\nu_i$ , it has to be ensured that  $\nu_{res} \approx \nu_i$ . The resonance frequency is tuned by adjusting the inductive and capacitive properties of a unit cell and CLS. This is achieved by varying  $l_1$ ,  $l_2$  and  $c$ . Multiple configurations with different resonance frequencies are

## 4.2 Metamaterial Low Reflection Coatings

listed in Tab. 4.3 and the corresponding reflectivity curves are plotted in Fig. 4.8.

In the following methods for adjusting the resonance frequency will be given. Unless otherwise indicated, it will be assumed from now on that  $a_x = a_y = 1.4$  mm and  $a_z = 0.1$  mm. The dielectric spacer is standard FR4 with  $\epsilon_r = 4.4$  and  $\tan \delta = 0.02$ . In full wave simulations the CLS and ground plane are modeled by 5  $\mu\text{m}$  thick copper.

The influence of the vertical armlength  $l_1$  on  $\nu_{res}$  is discussed first. Coatings with  $l_2 = 0.8$  mm,  $c = 0.1$  mm and  $l_1$  varying between  $0.6 < l_1 < 1.1$  mm are considered. As shown in Fig. 4.9(a),  $\nu_{res}$  shifts from approximately 47 to 33 GHz as  $l_1$  increases from 0.6 to 1.1 mm, which is due to the increasing capacitance. Increasing  $l_1$  decreases the gap  $g$  between the lateral arms of two contiguous CLS and increases the capacitance (Fig. 4.6a). Due to the fact that  $\nu_{res}$  is inversely proportional to the capacitance,  $\nu_{res}$  shifts to lower frequencies as  $l_1$  increases and vice versa.

A similar effect is obtained by varying  $l_2$ . Coatings with  $l_1 = 0.9$  mm,  $c = 0.1$  mm and  $l_2$  varying between  $0.6 < l_2 < 1.2$  mm are considered. The results are plotted in Fig. 4.9(b). As mentioned previously, the gap between two consecutive lateral arms can be regarded as a parallel plate capacitor whose effective area increases as  $l_2$  gets

Sample	mm			GHz
	$l_1$	$l_2$	$c$	
I	0.6	1.2	0.25	35.4
II	0.9	0.9	0.10	36.9
III	0.8	0.8	0.2	38.7
IV	0.8	0.8	0.15	39.8
V	0.6	0.8	0.30	42.3
VI	0.6	0.8	0.25	43.6

**Table 4.3:** Dependence of  $\nu_{res}$  on  $l_1$ ,  $l_2$  and  $c$  with  $a_x = a_y = 1.4$  mm,  $a_z = 0.1$  mm,  $\epsilon_r = 4.4$  and  $\tan \delta = 0.02$ .

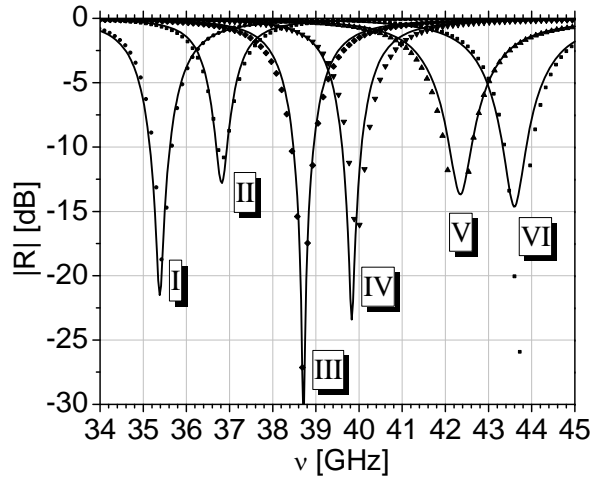


**Figure 4.8:**  $|R|$  for configurations in Tab. 4.3. Results obtained with equivalent circuit model (solid line) and full wave simulation (dotted line).

#### 4. METAMATERIAL MICROWAVE ABSORBERS

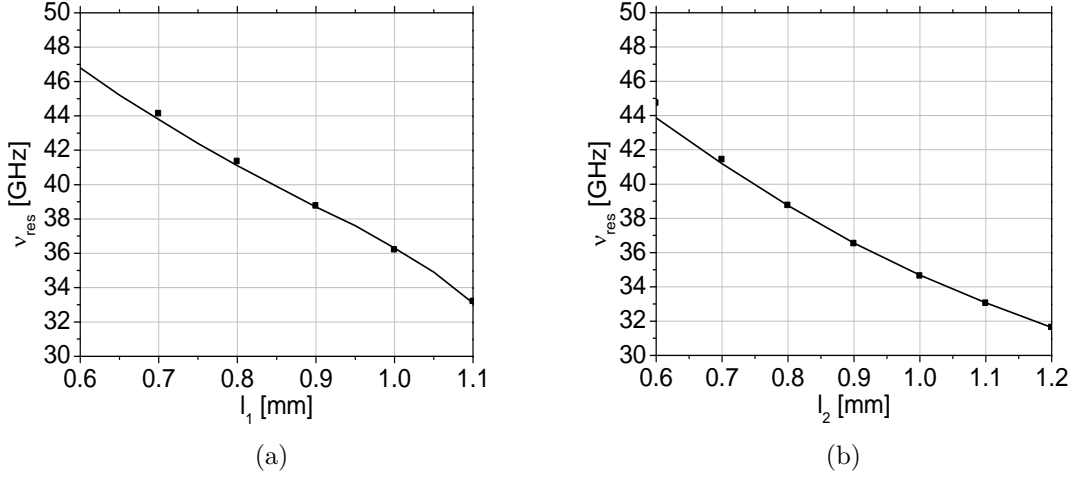


**Figure 4.9:** (a) Effect of  $l_1$  and (b)  $l_2$  on  $\nu_{res}$ . Results obtained with equivalent circuit model (solid line) and full wave simulation (dotted line).

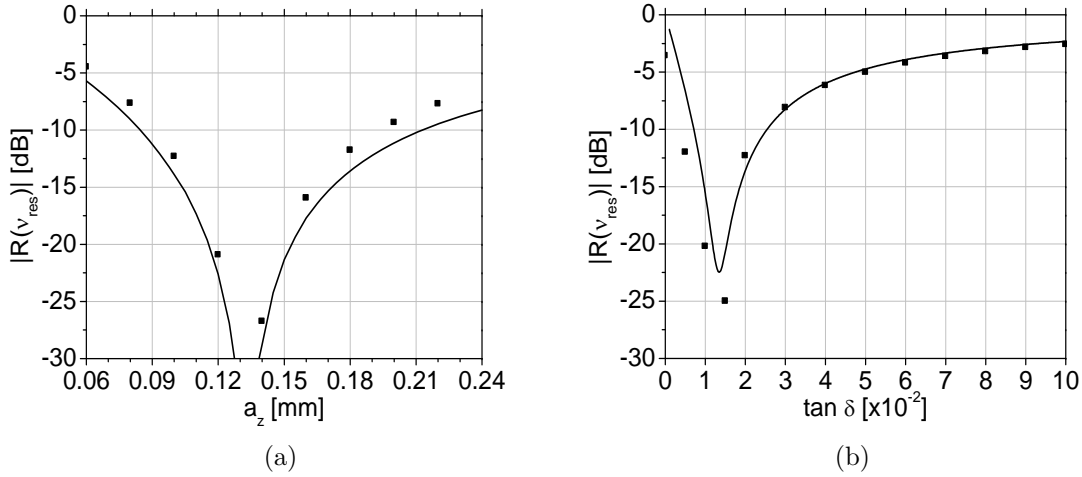


**Figure 4.10:** (a) Effect of  $a_z$  and (b)  $\tan \delta$  on  $|R(\nu_{res})|$ . Results obtained with equivalent circuit model (solid line) and full wave simulation (dotted line).

larger and more charge can build up in the gap. This enhances the capacitance and  $\nu_{res}$  shifts to lower frequencies.

The influence of the strip width  $c$  is discussed next. If the vertical ( $l_1$ ) and lateral ( $l_2$ ) armlengths are held fixed, increasing  $c$  has two effects. The first effect is that the gap  $g$  between contiguous inclusions decreases, as a result of which the total capacitance grows and  $\nu_{res}$  shifts to lower frequencies. The second effect is that the total inductance, which is inversely proportional to  $c$ , decreases and  $\nu_{res}$  shifts to higher frequencies. In summary, depending on the change in inductance ( $L$ ) and capacitance ( $C$ ),  $\nu_{res} \approx 1/\sqrt{LC}$  can shift to lower or higher frequencies.

Up to now, methods for adjusting  $\nu_{res}$  which do not provide any control over the amount of absorption (reflection) at  $\nu_{res}$  have been described. Adjusting the amount of absorption at  $\nu_{res}$  by varying the thickness and loss tangent of the substrate is discussed next.

The coating designed in Sec. 4.2.3 with  $a_x = a_y = 1.4$  mm,  $a_z = 0.1$  mm,  $l_1 = 0.9$  mm,  $l_2 = 0.8$  mm,  $c = 0.1$  mm,  $\epsilon_r = 4.4$  and  $\tan \delta = 0.02$  is thereby considered. The thickness of the dielectric spacer is varied between  $0.06 < a_z < 0.24$  mm and the change in reflectivity at  $\nu_{res} = 38.7$  GHz is observed. The result is plotted in Fig. 4.10(a). Reflectivity is at minimum when  $0.12 < a_z < 0.14$  mm, where  $X(\nu_{res}) \approx 0$  and  $G(\nu_{res}) \approx \eta_0$ .

An alternative way of optimizing  $G(\nu_{res})$  is achieved through adjusting  $\tan \delta$ . The thickness is kept constant at  $a_z = 0.1$  mm and  $\tan \delta$  is varied between  $0 < \tan \delta < 0.1$ . The result is plotted in Fig. 4.10(b). Reflectivity is at minimum when  $\tan \delta \approx 0.015$  and increases for higher loss tangents. As  $\tan \delta \rightarrow 0$ ,  $|R(\nu_{res})|$  also increases and approaches unity, indicating that a lossless coating has no effect and is equivalent to a PEC. In summary, the amount of reflection at  $\nu_{res}$  depends strongly on the loss tangent and thickness of the dielectric spacer.

### 4.2.5 Angle of Incidence and Polarization Dependence

The analysis has so far been limited to normally incident waves with a specific polarization, TEM modes with  $E_x$ ,  $H_y$ ,  $k_z$  as shown in Fig. 4.6. The angle and polarization dependence of reflectivity is investigated in the following. The coating designed in Sec. 4.2.3 is thereby considered. The reflectivity is determined at the resonance frequency  $\nu_{res} = 38.7$  GHz. For normal incidence the reflectivity and effective surface impedance have been given in Fig. 4.7. Since the equivalent circuit model is valid only for quasi TEM modes with  $E_x$ ,  $H_y$ ,  $k_z$  and cannot be used for arbitrary angle of incidence and polarization, full wave simulations with HFSS<sup>®</sup> are employed.

From previous discussions, it is known that the simulation model is based on a unit cell and it is assumed that the coating extends to infinity in the  $xy$  plane (Fig. 4.11). For normal plane wave incidence with  $E_x$  or  $E_y$  it suffices to terminate the simulation volume by a pair of PEC and PMC boundaries at the sidewalls. On

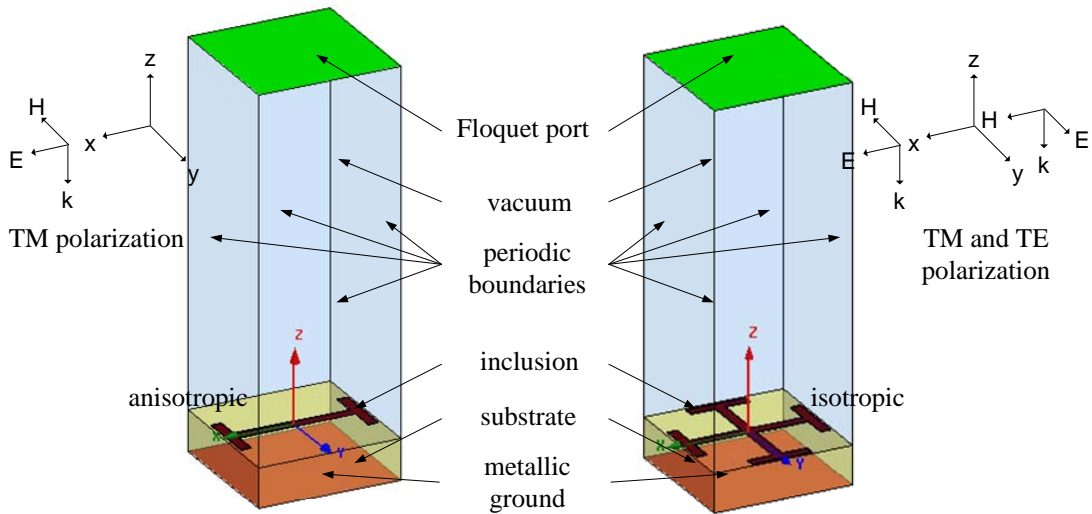


**Figure 4.11:** Simulation volume consisting of a unit cell with anisotropic (left) and isotropic (right) CLS.

#### 4. METAMATERIAL MICROWAVE ABSORBERS

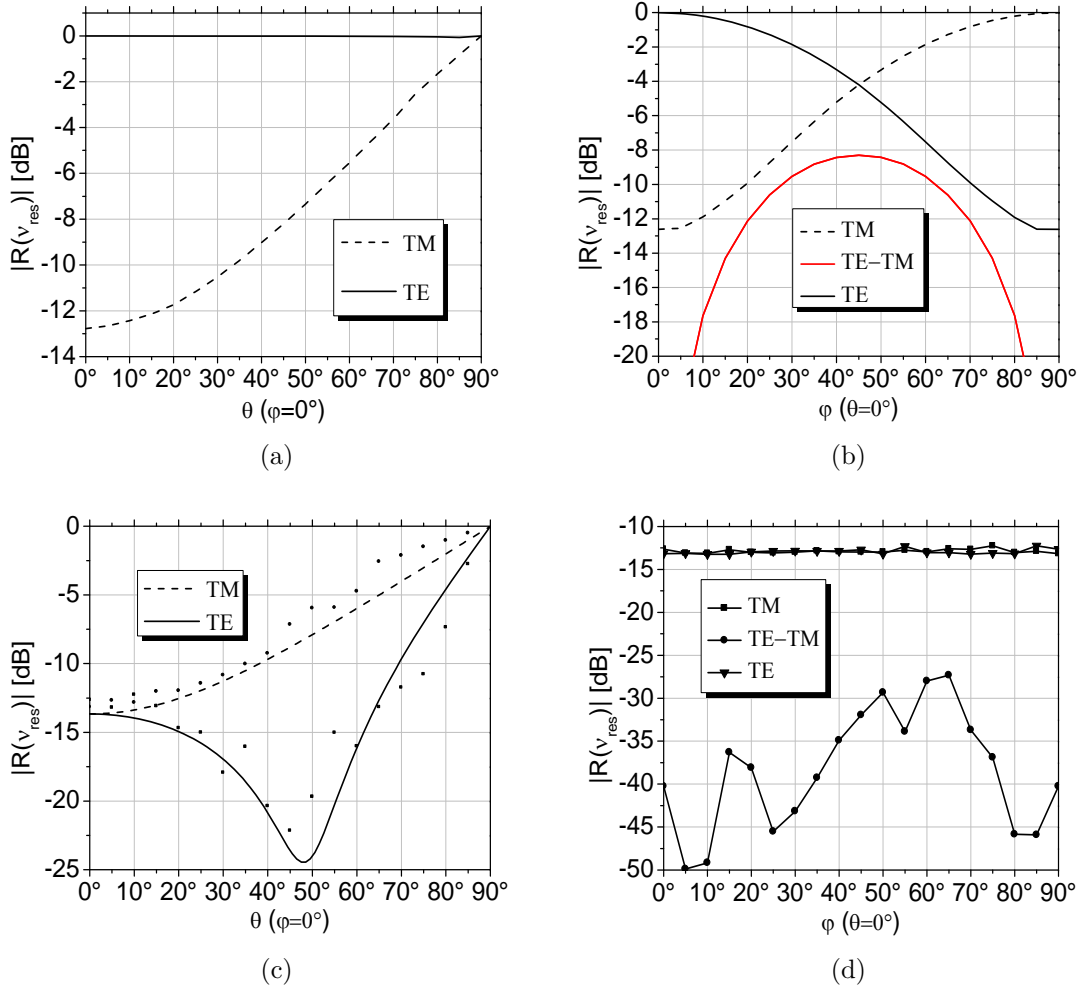


**Figure 4.12:** (a) Angle and (b) polarization dependence of  $|R(\nu_{res})|$  for anisotropic configuration. (c) Angle and (d) polarization dependence of  $|R(\nu_{res})|$  for isotropic configuration. Only in (c): results obtained with full wave simulation (dotted line) and from (A.6) with  $Z_s(\nu_{res}) = 250 - 30j$  (solid line).

the other hand, for waves with general direction of incidence and polarization, the phase of the incident wave varies linearly between unit cells and has to be accounted for. This is incorporated into the simulation model by a pair of linked boundaries (master/slave) and a Floquet port excitation in HFSS<sup>®</sup>.

A global spherical coordinate system with  $\theta$  and  $\varphi$ , where  $\varphi$  is measured from the  $x$  axis and  $\theta$  is measured from the  $z$  axis, is used to describe the direction of the incident wave. The Fresnel reflection coefficients  $R^{\text{TE}}$  for TE and  $R^{\text{TM}}$  for TM polarization (App. A) are computed for the design given in Sec. 4.2.3 at  $\nu_{res} = 38.7$  GHz. The cross polar reflection coefficients are denoted by  $R^{\text{TE-TM}}$ .

The angular dependence of the reflectivity in the  $\varphi = 0^\circ$  plane is plotted in Fig. 4.12(a).  $R^{\text{TM}}$  remains below 10 dB for  $\theta < 40^\circ$ . Irrespective of the incidence angle, the coating does not operate for TE polarization. This is due to the anisotropy of the CLS. The anisotropic response is more clearly seen in Fig. 4.12(b), where  $\theta = 0^\circ$  and the plane of incidence and therefore polarization direction is rotated from  $\varphi = 0^\circ$

to  $90^\circ$ .  $R^{\text{TE}}$  and  $R^{\text{TM}}$  are symmetric with respect to  $\varphi = 45^\circ$  at which the coupling between the two polarization states, i.e.  $R^{\text{TE-TM}}$ , is at maximum.

Isotropy can be provided by adding a second element of the same size and shape rotated by  $\varphi = 90^\circ$ , yielding a subwavelength Jerusalem cross inclusion [85] as shown in the right of Fig. 4.11. The resonance frequency remains thereby unaffected. The angular dependence of the reflectivity in the  $\varphi = 0^\circ$  plane for the isotropic configuration is indicated in Fig. 4.12(c) by the dotted lines. The solid lines represent results obtained from (A.6) with  $\eta_2 = Z_s(\nu_{\text{res}}) = 250 - 30j$  and  $\eta_1 = \eta_0$ . The results are in good agreement and it is concluded that the reflection response of an isotropic coating is accurately described by the surface impedance obtained at normal incidence with  $\theta = 0^\circ$  and  $\varphi = 0^\circ$ .  $R^{\text{TE}}$  shows a minimum at the Brewster's angle which occurs at  $\theta \approx 50^\circ$ . The isotropy is further verified by Fig. 4.12(d).  $R^{\text{TE}}$  and  $R^{\text{TM}}$  are equal in magnitude and do not change with  $\varphi$ . They are found to remain almost constant at 14 dB. Cross coupling is almost negligible and remains below 25 dB.

### 4.2.6 Realization

The unit cell composition is chosen according to configuration II in Tab. 4.3, with  $a_x = a_y = 1.4$  mm,  $l_1 = l_2 = 0.9$  mm and  $c = 0.1$  mm. A lossy dielectric (standard FR4) with  $\epsilon_r = 4.4$ ,  $\tan \delta = 0.02$  and thickness  $a_z = 0.1$  mm is used as the dielectric spacer. The CLS and ground plane consist of  $5 \mu\text{m}$  thick copper. Before manufacturing, the proposed design is verified with HFSS<sup>®</sup>.  $|R(\nu)|$  and  $Z_s(\nu)$  are plotted in Fig. 4.13 (a) and (b), respectively. At the resonance frequency  $\nu_{\text{res}} = 36.925$  GHz maximum reduction in reflectivity is 11 dB, the ratio of wavelength to layer thickness is about  $\lambda/80$  and the size of a unit cell is approximately  $\lambda/6$ .

A plate measuring  $250 \times 250 \text{ mm}^2$  and composed of  $178 \times 178$  unit cells is fabricated with printed circuit board technology and its reflection response is measured in

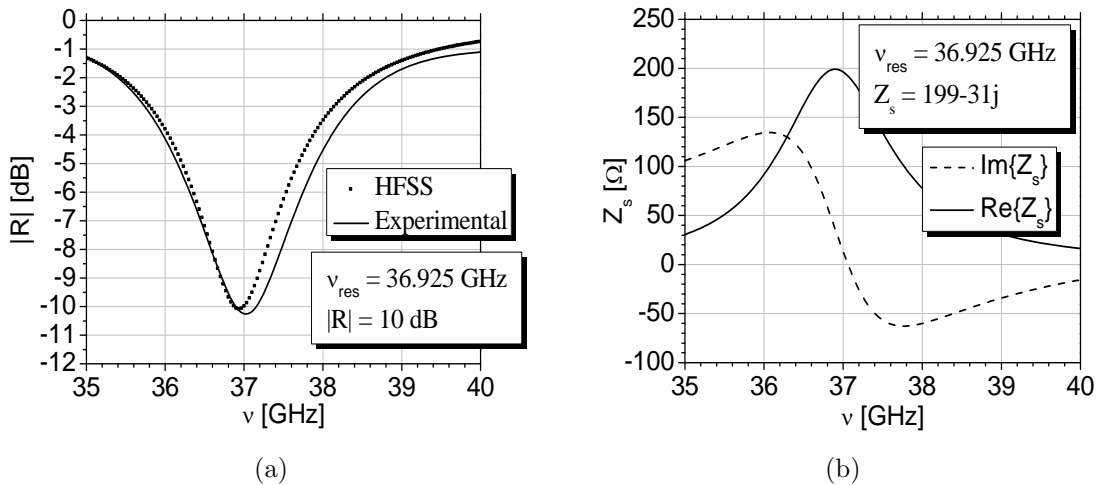


**Figure 4.13:** (a)  $|R(\nu)|$  and (b)  $Z_s(\nu)$  for the realized MTM-LRC as described in Sec. 4.2.6. In (a) the solid line represents measurement and the dotted line represents full wave simulation results.

## 4. METAMATERIAL MICROWAVE ABSORBERS

---

free space. A portion of the realized sample is shown in Fig. 4.14(a). The measurement result is shown by the dotted line in Fig. 4.13(a). A good agreement between simulation and measurement is obtained.

A major advantage of MTM-LRCs is that they are much thinner than conventional absorbers, which can greatly reduce their weight. For example, the rate of absorption in conventional absorbers, such as the ECCOSORB<sup>®</sup> MF-112 from Emerson and Cuming for example, is about 10 dB/cm and in order to achieve an attenuation of 10 dB, a layer thickness of 1 cm would be necessary. The material has a density of 4 g/cm<sup>3</sup>, yielding an effective surface density of 4 g/cm<sup>2</sup>. In comparison, the realized MTM-LRC with a comparable attenuation level of approximately 10 dB, has an overall thickness of 0.11 mm (0.01 mm FR4 + 2 x 5 μm copper) resulting in a surface density of about 0.03 g/cm<sup>2</sup> (FR4 has a density of 2 g/cm<sup>3</sup>). A weight reduction by a factor of 140 per cm<sup>2</sup> is thereby achieved. In addition to this, MTM-LRCs can be applied to curved surfaces and can withstand high mechanical stress.

### 4.2.7 Radar Cross Section Reduction

Canonically shaped bodies play a key role in theoretical and experimental analysis of electromagnetic scattering. In order to demonstrate the applicability and effectiveness of the realized MTM-LRC in radar cross section reduction (RCSR), mono and bistatic RCS measurements of an aluminum cube with an edge length of 5 cm and coated with the realized sample are performed. The amount of scattering reduction is obtained by comparing the scattering patterns of the coated and uncoated cube. The cube is coated on three of its vertical faces with the realized coating from Sec. 4.2.6.

A bistatic measurement setup with separate receive and transmit antennas, as shown in Fig. 4.14(b), is used. The measurements are carried out at 36.925 GHz, where the reflectivity of the coating is at minimum. The distance between object and antennas is 80 cm, so that the far field condition  $2D^2/\lambda \approx 60$  cm with  $D = 5$  cm and  $\lambda \approx 0.8$  cm is satisfied. In order to account for different incidence angles, the cube is positioned on a turntable whose orientation is controlled with a motor controller. The transmitted and received signals are measured with a vector network analyzer (Anritsu 37269A). The whole measurement process (positioning the cube and antennas, synchronization of the transmit and receive times of signals) is automated with the help of a measurement and analysis software.

Measurements are carried out in the  $\varphi$  plane with  $\theta = 90^\circ$ . Horizontal polarization with  $E_\varphi$  is considered. To provide the correct response of the coating, the vertical arms ( $l_1$ ) of the CLS are oriented parallel to the  $\varphi$  plane. The complex scattering parameter for the coated  $S_{21}^c(\varphi)$  and uncoated  $S_{21}^{uc}(\varphi)$  case is measured at different scattering angles  $\varphi$ . The normalized scattering cross sections for the coated and uncoated cube are determined as

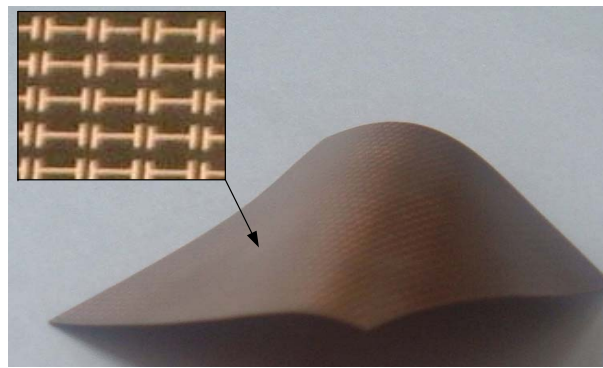
$$\sigma^c(\varphi) = 20 \log \frac{|S_{21}^c(\varphi)|}{|S_{21}^{uc}(0^\circ)|} \quad \sigma^{uc}(\varphi) = 20 \log \frac{|S_{21}^{uc}(\varphi)|}{|S_{21}^{uc}(0^\circ)|} \quad (4.17)$$

## 4.2 Metamaterial Low Reflection Coatings

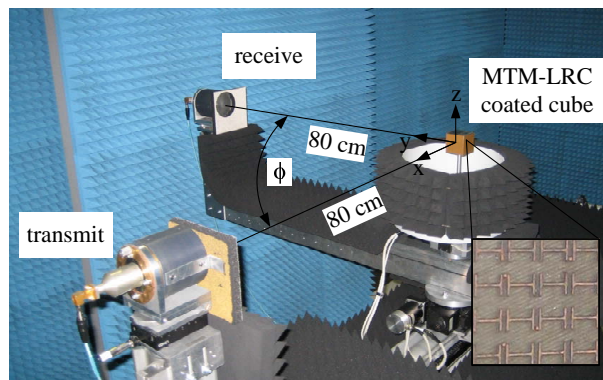
in the monostatic case and

$$\sigma^c(\varphi) = 20 \log \frac{|S_{21}^c(\varphi)|}{|S_{21}^{uc}(\varphi_s)|} \quad \sigma^{uc}(\varphi) = 20 \log \frac{|S_{21}^{uc}(\varphi)|}{|S_{21}^{uc}(\varphi_s)|} \quad (4.18)$$

in the bistatic case, where  $\varphi_s$  corresponds to the specular angle at which scattering is at maximum.

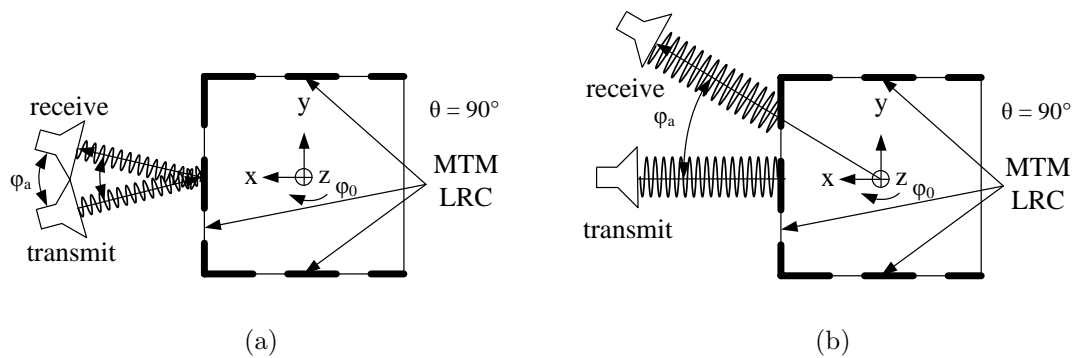


(a)



(b)

**Figure 4.14:** (a) A portion of the manufactured MTM-LRC consisting of CLS inclusions. (b) Measurement setup with the coated cube at its center. The inset shows a magnification of a part of the MTM-LRC.



(a)

(b)

**Figure 4.15:** (a) Quasi-mono and (b) bistatic RCS measurement configurations.

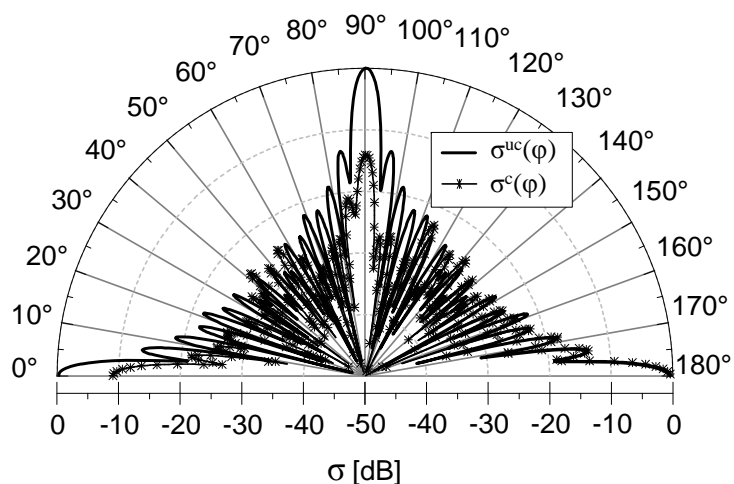


**Figure 4.16:** Normalized monostatic RCS for the coated and uncoated cube with horizontal polarization at 36.925 GHz.

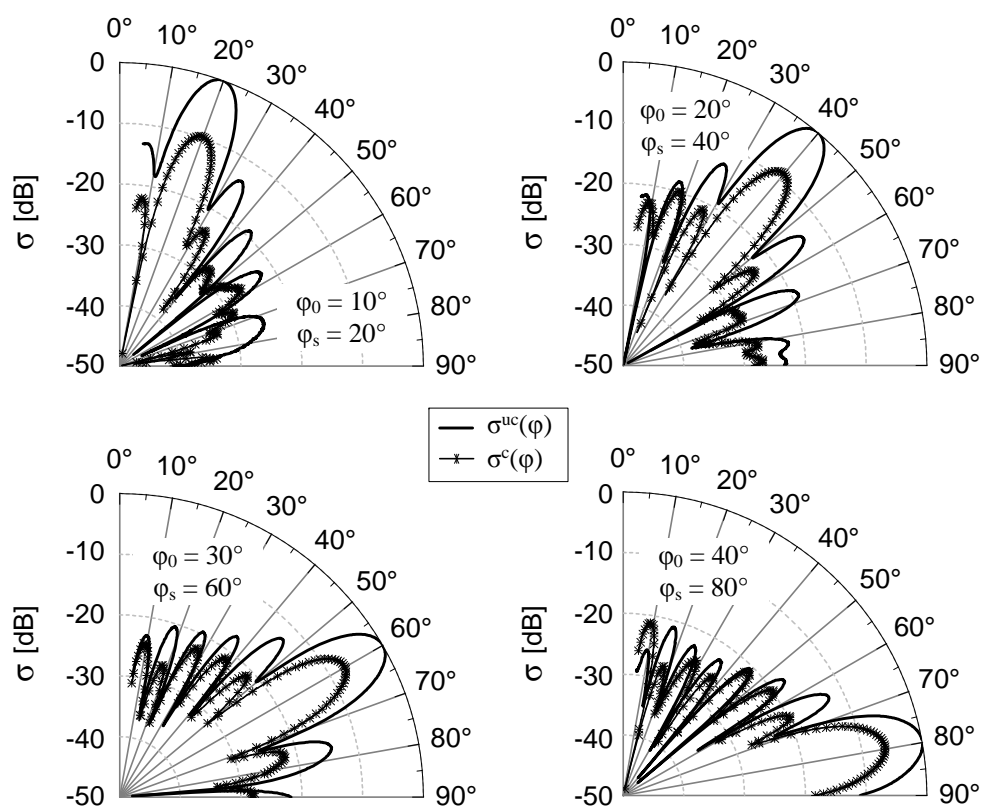


**Figure 4.17:** Normalized bistatic RCS for the coated and uncoated cube for incidence angles  $\varphi_o = 10^\circ, 20^\circ, 30^\circ$  and  $40^\circ$ . Horizontal polarization at 36.925 GHz.

The monostatic configuration with collocated transmit and receive antennas plays a crucial role in the development of low reflection coatings and is considered first. In this work, a quasi-monostatic configuration (Fig. 4.15(a)) with fixed receive and transmit antennas at  $\varphi \approx 0^\circ$  and a separation angle of  $\varphi_a = 3^\circ$  is used. Different backscattering angles are realized by rotating the cube in the  $\varphi$  plane. Due to the symmetry of the cube with respect to the  $x$  axis, only backscattering angles between  $0^\circ < \varphi < 180^\circ$  are considered. The uncoated cube is measured first.

The results are plotted in Fig. 4.16. Maximum scattering (0 dB) occurs at specular directions, which are given by  $\varphi = 0^\circ, 90^\circ$  and  $180^\circ$ , and the scattering pattern is normalized to its value at  $\varphi = 0^\circ$ . The coated cube is measured next. Its scattering pattern is plotted in the same figure. A reduction in RCS of approximately 10 dB is obtained at  $\varphi = 0^\circ$  and  $90^\circ$ , which is in accordance with the reflectivity of the flat sample of the MTM-LRC shown in Fig. 4.13(a). For  $0^\circ < \varphi < 90^\circ$  the RCS pattern of the coated cube is well below that of the uncoated one. As the uncoated side of the cube gets illuminated, i.e.  $\varphi \geq 90^\circ$ , the scattering reduction decreases and the RCS patterns of the coated and uncoated cube become almost identical.

The bistatic RCS, as shown in Fig. 4.15(b), is measured next. The transmitting antenna is fixed at  $\varphi = 0^\circ$  and the receiving one is swept from  $\varphi = 3^\circ$  to  $\varphi = 90^\circ$ . In order to account for different incidence angles, the object is rotated by  $\varphi_o = 10^\circ, 20^\circ, 30^\circ$  and  $40^\circ$ . The results are plotted in Fig. 4.17. RCS is at maximum in the specular direction for both the coated and uncoated cube. Due to the coating a reduction of approximately 10 dB is observed in the specular direction at  $\varphi = 2\varphi_o$ . The effect of the coating decreases with increasing incidence angle or  $\varphi_o$ .

### 4.2.8 Modeling with Impedance Boundaries

Due to limitations on memory and computer performance, it is practically impossible to simulate scattering from electrically large and complex scatterers that are coated with a realistic MTM-LRC composed of many unit cells. The effective surface impedance provides thereby a simplified description which permits modeling the coating with impedance boundary conditions. In order to evaluate the accuracy and efficiency of the impedance approach, simulations with HFSS<sup>®</sup> and BISTRO have been carried out. BISTRO is an in house tool based on physical theory of diffraction, which corrects physical optics by accounting for edge diffraction phenomena. It is capable of modeling basic scattering mechanisms, including reflection from non-metallic interfaces and curved surfaces, multiple reflections and diffraction by edges.

As in the previous section, the cube is coated on three of its vertical faces with the MTM-LRC, which is modeled as an impedance boundary with  $Z_s = 199 - 31j \Omega$  at 36.925 GHz. Results for the bistatic configuration with  $\varphi_o = 10^\circ$  are shown in Fig. 4.18(a). The measurement results are normalized to the RCS value for the uncoated cube, obtained with HFSS at the specular angle  $\varphi_s = 2\varphi_o = 20^\circ$  where scattering is at maximum and slightly above 0 dBsm. For the main lobe and the first sidelobes the agreement between the RCS curves obtained with different methods is very good. It can be concluded that the MTM-LRC is accurately described by its

#### 4. METAMATERIAL MICROWAVE ABSORBERS

effective surface impedance and can be modeled by an impedance boundary condition, which greatly simplifies the analysis.

According to (4.4), maximum reduction in reflectivity is obtained when  $Z_s = \eta_0 = 377 \Omega$ . The influence of an ideal coating with  $Z_s = 377 \Omega$  on the scattering pattern of the cube is illustrated in Fig. 4.18(b). The results obtained with HFSS<sup>®</sup> indicate a scattering reduction of approximately 28 dBsm in the specular direction.

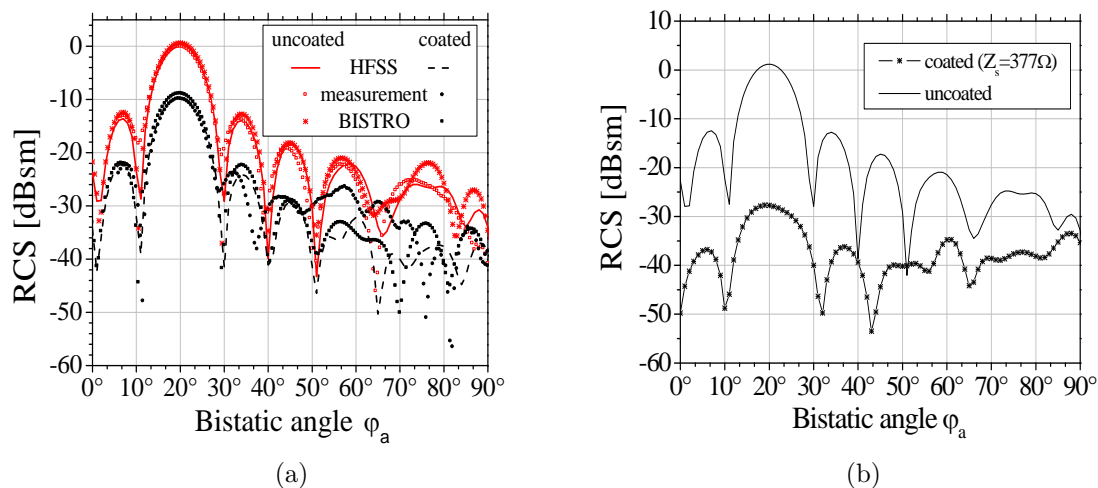


**Figure 4.18:** Comparison between different methods for bistatic RCS of coated and uncoated cube at 36.925 GHz and horizontal polarization. (a) Measurement, HFSS<sup>®</sup> and BISTRO with  $Z_s = 199 - 31j \Omega$  and (b) HFSS<sup>®</sup> with  $Z_s = 377 \Omega$  (ideal case).

# 5

## Results and Conclusion

Metamaterials constitute a new class of composite artificial electromagnetic materials. The possibility of engineering materials with unique and controllable electromagnetic properties has led to novel approaches in the realization of enhanced microwave devices. The concepts of metamaterial microwave superlenses and absorbers have been considered in this work.

In Chapter 3, the imaging capabilities of double negative metamaterial superlenses excited with arbitrarily oriented dipoles have been investigated. A new type of image distortion, the unequal transmission of TE and TM portions of the fields, by imaging with a superlens with slightly perturbed  $\epsilon_r$  and  $\mu_r$  has been identified and studied.

The imaging characteristics of a double negative metamaterial slab have been considered up to now mainly in two dimensions, in combination with a line source, and in three dimensions with a dipole oriented perpendicular to the surface of the slab. In Sec. 3.2, a complete analytical solution for the imaging capabilities of a double negative metamaterial slab excited by an arbitrarily oriented electric or magnetic dipole has been derived. The solution for perpendicular dipole source excitation has thereby been extended to the case of arbitrary excitation and a tool for evaluating the field intensities in the vicinity of the image plane has been developed.

This tool has been used to determine the exact field distribution in the vicinity of the image plane of non ideal slabs with  $\epsilon_r \neq -1$ ,  $\mu_r \neq -1$  excited by generally oriented sources. It has been shown that even slight perturbations in the slab material cause a high-frequency cutoff in the wavenumber spectrum of the transmitted field and lead to a significant change of the field distribution in the vicinity of the image plane, resulting in a degradation of the image quality.

The main results of the chapter can be summarized as follows: As long as the real part of the refractive index of the slab retains its value of  $\text{Re}\{n\} = -1$ , deviations in the real or imaginary parts of  $\epsilon_r$  and  $\mu_r$  have identical effects on the field distribution at the image plane, irrespective of the type and orientation of the excitation dipole. On the other hand, if  $\epsilon_r$  and  $\mu_r$  are perturbed unequally such that  $\text{Re}\{n\} \neq -1$  and the slab is excited by a dipole oriented parallel to its surface, the TE and TM portions of the source field are unequally transmitted through the slab. Approximations in the electrostatic limit fail to predict this phenomenon and obtaining the exact field distribution in the vicinity of the image plane behind the slab becomes important. Based

## 5. RESULTS AND CONCLUSION

---

on the analytical formulation in Sec. 3.2, a tool has been developed for this purpose. Furthermore, field intensities behind the slab reveal that a double negative metamaterial slab does not provide super-resolving capabilities in three dimensions. Double negative metamaterial superlenses provide super-resolution only in two dimensions at the image plane.

It can be concluded that, although a double negative metamaterial slab may outperform diffraction limited imaging devices, the logarithmic dependence of the cutoff wavenumber and hence the image quality on the perturbations in the slab material indicates that it is difficult to realize a 100% perfect metamaterial superlens.

In Chapter 4, the applicability of Drude and Lorentz dispersive metamaterials in the realization of electrically thin microwave absorbers composed of a single layer strip-SRR or CLS-SRR metamaterial has been studied. Designs operating in the Ku band (12 - 18 GHz) have been proposed and methods for adjusting the absorbers permittivity and permeability to reduce reflectivity at a specific frequency have been given. It has been shown that it is possible to adjust the effective response of metamaterial absorbers by suitably choosing, combining and dimensioning the inclusions, providing multiple degrees of freedom during the design process.

Radar absorbing materials are among the most practical and common radar cross section reduction techniques. Adjusting the electromagnetic specifications of the absorber to a given application is an important task during the design process. The limited choice of naturally occurring materials with suitable dielectric and magnetic properties constitutes thereby a major challenge, making the application of metamaterials highly feasible.

In the second part of Chapter 4, a systematic way of designing truly planar metamaterial low reflection coatings consisting of periodic arrangements of capacitively loaded strip inclusions has been described. An equivalent circuit model based on coupled microstrip line theory has been developed to characterize and optimize the reflectivity. It has been shown that the amount of reflectivity is strongly associated with dielectric and conductive loss mechanisms inside the coating.

A design for a coating operating in the Ka-band (30 - 40 GHz), with a unit cell size of  $\lambda/6$  and overall thickness of  $\lambda/80$  has been proposed, realized and measured. Although the sample is only 0.1 mm thick, it reduces reflectivity by 10 dB at the design frequency and has a bandwidth of about one GHz measured at the -6 dB level.

Furthermore, the applicability and effectiveness in radar cross section reduction has been demonstrated by considering mono- and bistatic scattering from a metallic cube coated with the realized sample. It has been shown that it is possible to describe the electromagnetic response of the coating by an effective surface impedance, which can then be used in the framework of impedance boundary conditions to simulate the radar cross section of electrically large and complex scatterers.

The use of metamaterial low reflection coatings is a promising approach to reduce scattering from real targets. This kind of coatings can be made much thinner than conventional absorbers, which can greatly reduce their weight. In addition to this, they can be applied to curved surfaces and can withstand high mechanical stress.

It has to be mentioned that, due to its resonant characteristics, the operation

---

bandwidth of the investigated metamaterial low reflection coatings is limited. The relative -6 dB bandwidth of the realized coating in Sec. 4.2.6 for example is about 3%. Various approaches to widening the bandwidth and improving the absorption rate at the operation frequencies are under development. A broadband operation range could be achieved by a combination of multiple layers, each having its own resonance characteristic, or the application of multiple inclusions with close but slightly different resonances in a single layer structure.

## 5. RESULTS AND CONCLUSION

---

# Appendix A

## Reflection and Transmission through Layered Media

Reflection and transmission of plane electromagnetic waves from planar layers with arbitrary stratification is considered. The material provides supplementary information for Chapters 3 and 4. Its contents can be found in [57].

For plane electromagnetic waves incident on a medium composed of planar layers with arbitrary stratification and various dielectric and magnetic properties the reflected and transmitted fields are specified in terms of the reflection and transmission coefficients

$$R = \frac{E^r}{E^i} \quad \text{and} \quad T = \frac{E^t}{E^i}. \quad (\text{A.1})$$

$E^i$ ,  $E^r$  and  $E^t$  are the incident, reflected and transmitted electric fields, respectively. Reflection and transmission in three different configurations consisting of semi-infinite media, a slab of thickness  $d$  between two semi-infinite media and slab of thickness  $d$  backed by a conductor are considered in the following (Fig. A.1).

### A.1 Semi-infinite Media

Plane waves incident on an interface between two planar media of refractive indices  $n_1 = \sqrt{\epsilon_{1r}\mu_{1r}}$ ,  $n_2 = \sqrt{\epsilon_{2r}\mu_{2r}}$  and characteristic impedances  $\eta_1 = \sqrt{\mu_{1r}/\epsilon_{1r}}\eta_0$ ,  $\eta_2 = \sqrt{\mu_{2r}/\epsilon_{2r}}\eta_0$ , as shown in Fig. A.1(a), are considered.

The incident wave is decomposed into perpendicular and parallel components with respect to the plane of incidence ( $xz$  plane), i.e. perpendicular (TE) and parallel (TM) polarizations. TE polarization with  $E_x^i = 0$ ,  $E_y^i \neq 0$ ,  $E_z^i = 0$  and TM polarization with  $E_x^i \neq 0$ ,  $E_y^i = 0$ ,  $E_z^i \neq 0$  are treated separately. The two polarization states can be combined by the principle of superposition to treat arbitrary polarization.

The boundary condition requires that the tangential field components are continuous across the interface, i.e.  $E_{x,y}^i + E_{x,y}^r = E_{x,y}^t$ . The law of reflection states that  $\theta_i = \theta_r$  and that the angle of incidence is equal to the angle of reflection. The angle

## A. REFLECTION AND TRANSMISSION THROUGH LAYERED MEDIA

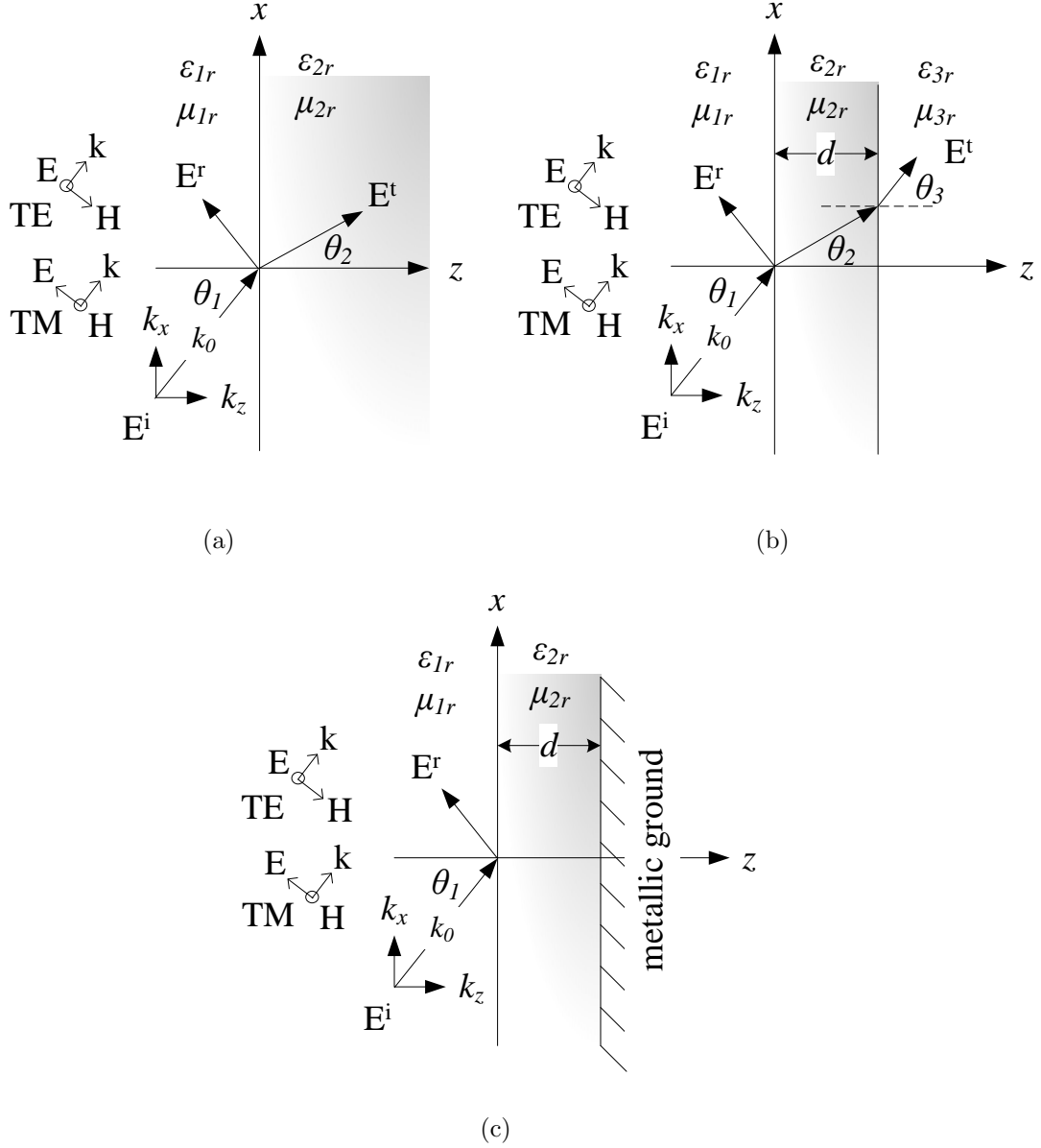


**Figure A.1:** Reflection and transmission of plane electromagnetic waves incident on (a) semi-infinite media, (b) single layer slab of thickness  $d$  and (c) same slab backed by a metallic ground.

of refraction  $\theta_2$  is determined from Snell's law

$$n_2 \sin \theta_2 = n_1 \sin \theta_1 \quad (\text{A.2})$$

as  $\sin \theta_2 = (n_1/n_2) \sin \theta_1$ . The TE-TM reflection and transmission coefficients are

$$R = \frac{\eta_2^T - \eta_1^T}{\eta_1^T + \eta_2^T} \quad \text{and} \quad T = \frac{2\eta_2^T}{\eta_1^T + \eta_2^T}, \quad (\text{A.3})$$

with transverse impedances  $\eta_{1,2}^T = \eta_{1,2}/\cos \theta_{1,2}$  and  $\eta_{1,2}^T = \eta_{1,2} \cos \theta_{1,2}$  for TE and TM

polarizations, respectively. Using the identity

$$\cos \theta_2 = [1 - (n_1/n_2)^2 \sin^2 \theta_1]^{1/2}, \quad (\text{A.4})$$

the reflection coefficients are rewritten as

$$\begin{aligned} R^{\text{TE}} &= \frac{(\eta_2/\eta_1) \cos \theta_1 - [1 - (n_1/n_2)^2 \sin^2 \theta_1]^{1/2}}{(\eta_2/\eta_1) \cos \theta_1 + [1 - (n_1/n_2)^2 \sin^2 \theta_1]^{1/2}} \\ R^{\text{TM}} &= -\frac{(\eta_1/\eta_2) \cos \theta_1 - [1 - (n_1/n_2)^2 \sin^2 \theta_1]^{1/2}}{(\eta_1/\eta_2) \cos \theta_1 + [1 - (n_1/n_2)^2 \sin^2 \theta_1]^{1/2}}. \end{aligned} \quad (\text{A.5})$$

Furthermore, if  $(n_1/n_2)^2 \sin^2 \theta_1 \ll 1$ , this term can be neglected and R approximated as

$$R^{\text{TE}} \approx \frac{\eta_2 \cos \theta_1 - \eta_1}{\eta_2 \cos \theta_1 + \eta_1} \quad \text{and} \quad R^{\text{TM}} \approx \frac{\eta_2 - \eta_1 \cos \theta_1}{\eta_2 + \eta_1 \cos \theta_1}. \quad (\text{A.6})$$

## A.2 Layered Media

A more complex situation occurs when plane waves are incident on media consisting of an arbitrary number of layers with different dielectric and magnetic properties. Consider a two-interface problem consisting of a slab of thickness  $d$  with  $n_2 = \sqrt{\epsilon_{2r}\mu_{2r}}$ , separating the semi-infinite media with  $n_1 = \sqrt{\epsilon_{1r}\mu_{1r}}$  and  $n_3 = \sqrt{\epsilon_{3r}\mu_{3r}}$  (Fig. A.1(b)). The propagation matrix

$$A = \begin{bmatrix} \cos \alpha_2 & j\eta_2^T \sin \alpha_2 \\ \frac{j}{\eta_2^T} \sin \alpha_2 & \cos \alpha_2 \end{bmatrix} \quad (\text{A.7})$$

relates the tangential field components at the slab interfaces to each other. The electrical thickness of the slab is given by  $\alpha_2 = k_2 d [1 - (n_1/n_2)^2 \sin^2 \theta]^{1/2}$  and  $k_2 = n_2 \omega / c$  is the wavenumber inside the slab. The transverse impedances for TE and TM polarizations are given by

$$\eta_{1,2,3}^T = \eta_{1,2,3} / \cos \theta_{1,2,3} \quad \text{and} \quad \eta_{1,2,3}^T = \eta_{1,2,3} \cos \theta_{1,2,3}, \quad (\text{A.8})$$

respectively. The cosines of the refraction angles in the second and third medium are determined in terms of the angle of incidence  $\theta_1$  from Snell's law in (A.2) as

$$\cos \theta_2 = [1 - (n_1/n_2)^2 \sin^2 \theta_1]^{1/2} \quad \text{and} \quad \cos \theta_3 = [1 - (n_1/n_3)^2 \sin^2 \theta_1]^{1/2}. \quad (\text{A.9})$$

## A. REFLECTION AND TRANSMISSION THROUGH LAYERED MEDIA

---

If the media 1 and 3 are identical, i.e.  $n_1 = n_3$ , then  $\theta_3 = \theta_1$  and the wave exits the slab with the incidence angle. An effective input impedance at the first interface of the slab is defined as

$$Z = \frac{A_{11}\eta_3^T - A_{12}}{A_{22} - A_{21}\eta_3^T} = \eta_2^T \frac{\eta_3^T + j\eta_2^T \tan \alpha_2}{\eta_2^T + j\eta_3^T \tan \alpha_2}, \quad (\text{A.10})$$

where  $A_{11}$ ,  $A_{12}$ ,  $A_{21}$  and  $A_{22}$  are elements of the matrix  $A$ . The reflection and transmission coefficients are

$$R = \frac{Z - \eta_1^T}{Z + \eta_1^T} \quad \text{and} \quad T = \frac{2(ZA_{22} + A_{12})}{Z + \eta_1^T} \quad (\text{A.11})$$

and can be further expressed as

$$R = \frac{\eta_2^T [\eta_3^T - \eta_1^T] + j [(\eta_2^T)^2 - \eta_1^T \eta_3^T] \tan \alpha_2}{\eta_2^T [\eta_3^T + \eta_1^T] + j [(\eta_2^T)^2 + \eta_1^T \eta_3^T] \tan \alpha_2}$$

$$T = \frac{2\eta_2^T \eta_3^T}{\eta_2^T [\eta_3^T + \eta_1^T] \cos \alpha_2 + j [(\eta_2^T)^2 + \eta_1^T \eta_3^T] \sin \alpha_2}. \quad (\text{A.12})$$

Finally, if the slab is backed by a perfectly electric conductor as shown in Fig. A.1(c), its reflection coefficient is obtained from (A.12) by setting  $\eta_3^T = 0$  and is

$$R = \frac{-\eta_1^T + j\eta_2^T \tan \alpha_2}{\eta_1^T + j\eta_2^T \tan \alpha_2}. \quad (\text{A.13})$$

The wave is completely reflected at the metallic ground and the transmission coefficient is zero in this case.

# Appendix B

## Radar Cross Section

The formal definition of radar cross section and a brief overview of electromagnetic scattering from arbitrarily shaped objects (or targets) is provided in this appendix. The material supports Chapter 4, especially the results presented in Sec. 4.2 and Sec. 4.2.7. Its contents is mainly taken from [64] and [94].

The detectability of an object (or target) at microwave frequencies is determined by its radar cross section (RCS). The RCS gives a measure of the scattered energy in a specific direction when an object is illuminated by an incident wave. It is defined as

$$\sigma = \frac{\text{power scattered toward receiver per unit solid angle}}{\text{incident power density}/4\pi} \quad (\text{B.1})$$

or

$$\sigma = \lim_{r \rightarrow \infty} 4\pi r^2 \left| \frac{W_s}{W_i} \right| = \lim_{r \rightarrow \infty} 4\pi r^2 \left| \frac{\mathbf{E}_s}{\mathbf{E}_i} \right|^2, \quad (\text{B.2})$$

where  $W_i \approx |\mathbf{E}_i|^2$  and  $W_s \approx |\mathbf{E}_s|^2$  are the incident and scattered power densities. There are basically two types of radar arrangements, which are the monostatic and bistatic configurations. As shown in Fig. B.1, the receiver and transmitter are collocated in the monostatic or backscattering arrangement. In the bistatic arrangement, on the other hand, the transmitter and receiver are separated.

To describe scattering from finite objects, a global spherical coordinate system as shown in Fig. B.2 can be used. For a time dependence of  $e^{j\omega t}$ , the incident wave is described by

$$\mathbf{E}_i = E_0 \hat{p} e^{-jkr\hat{i}\cdot\hat{s}} \quad \text{and} \quad \eta_0 \mathbf{H}_i = \hat{i} \times \mathbf{E}_i, \quad (\text{B.3})$$

where

## B. RADAR CROSS SECTION

---

$$\hat{i} = -\hat{x} \sin \theta_i \cos \varphi_i - \hat{y} \sin \theta_i \sin \varphi_i + \hat{z} \cos \theta_i$$

and

$$\hat{s} = \hat{x} \sin \theta_s \cos \varphi_s + \hat{y} \sin \theta_s \sin \varphi_s + \hat{z} \cos \theta_s \quad (\text{B.4})$$

are the unit vectors in the directions of the incident and scattered waves, respectively. The polarization vector  $\hat{p}$  of the incident wave is perpendicular to the direction of propagation and is given by

$$\hat{p} = a_{\theta_i} \hat{\theta}_i + a_{\varphi_i} \hat{\varphi}_i \quad (\text{B.5})$$

with the unit vectors

$$\hat{\theta}_i = \hat{x} \cos \theta_i \cos \varphi_i + \hat{y} \cos \theta_i \sin \varphi_i - \hat{z} \sin \theta_i$$

and

$$\hat{\varphi}_i = -\hat{x} \sin \varphi_i + \hat{y} \cos \varphi_i. \quad (\text{B.6})$$

In the far-field ( $kr \rightarrow \infty$ ), the scattered field is also directed perpendicular to the scattering direction and is given by

$$\mathbf{E}_s = E_0 \frac{e^{-jkr}}{kr} \left( b_{\theta_s} \hat{\theta}_s + b_{\varphi_s} \hat{\varphi}_s \right) \quad (\text{B.7})$$

with the unit vectors

$$\hat{\theta}_s = \hat{x} \cos \theta_s \cos \varphi_s + \hat{y} \cos \theta_s \sin \varphi_s - \hat{z} \sin \theta_s$$

and

$$\hat{\varphi}_s = -\hat{x} \sin \varphi_s + \hat{y} \cos \varphi_s. \quad (\text{B.8})$$

The corresponding magnetic field is  $\mathbf{H}_s = \eta_0 \hat{s} \times \mathbf{E}_s$ . The transformation between incident and scattered fields is described by the scattering matrix  $\mathbf{S}$  which is defined as

$$\begin{bmatrix} b_{\theta_s} \\ b_{\varphi_s} \end{bmatrix} = \begin{bmatrix} S_{\theta_s \theta_i} & S_{\theta_s \varphi_i} \\ S_{\varphi_s \theta_i} & S_{\varphi_s \varphi_i} \end{bmatrix} \begin{bmatrix} a_{\theta_i} \\ a_{\varphi_i} \end{bmatrix}. \quad (\text{B.9})$$

Finally, the scattering cross section is obtained as

$$\sigma_{uw} = \lim_{kr \rightarrow \infty} 4\pi r^2 |\mathbf{E}_u / \mathbf{E}_v|^2 = \lambda^2 / \pi |S_{uw}|^2, \quad (\text{B.10})$$

where  $u$  is given by  $\theta_s$  or  $\varphi_s$  and  $v$  is given by  $\theta_i$  or  $\varphi_i$ . RCS is usually expressed in Decibels as  $\sigma(\text{dBsm}) = 10 \log \sigma$ .

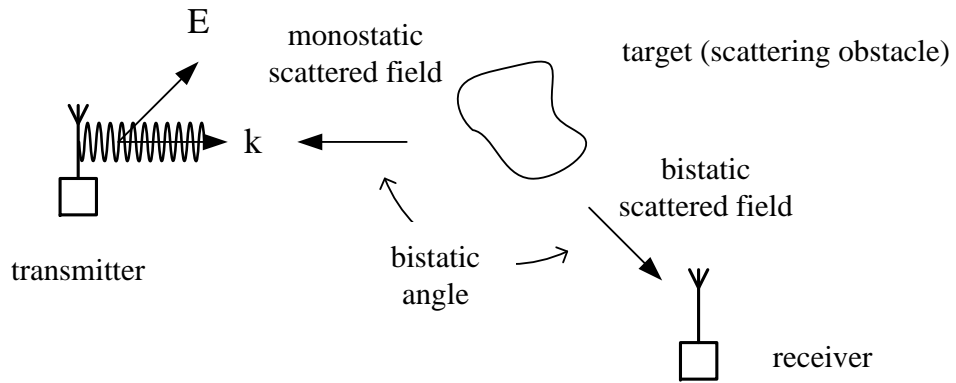


**Figure B.1:** Monostatic and bistatic RCS.

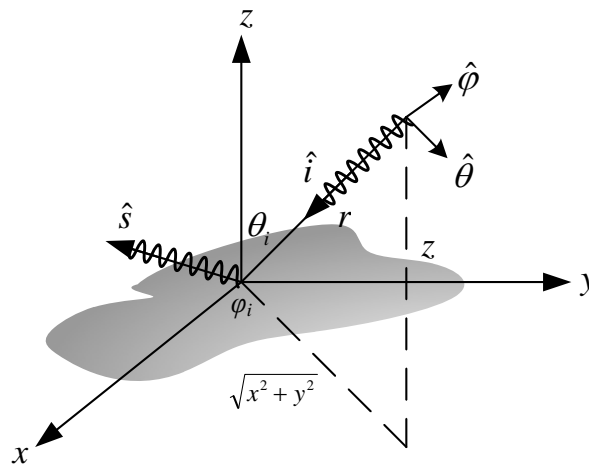


**Figure B.2:** Scattering in spherical coordinates.

## B. RADAR CROSS SECTION

---

# List of Figures

2.1	Feature size of a metamaterial with subwavelength inclusions embedded in a host. . . . .	8
2.2	(a) Swiss roll type magnetic resonator, taken from [120], (b) realization of a 1D double negative metamaterial (DNG MTM) in terms of a periodic arrangement of metallic wires and split ring resonators (SRR), taken from [108], (c) planarized version with metallic strips, taken from [101], (d) 2D planar transmission line metamaterial composed of lumped inductors and capacitors, taken from [31]. . . . .	9
2.3	Material classification according to $\epsilon'$ and $\mu'$ and types of supported waves. . . . .	12
2.4	(a) Distributed parameter model of a right handed transmission line and (b) corresponding dispersion diagram. . . . .	17
2.5	(a) Distributed parameter model of a left-handed transmission line and (b) corresponding dispersion diagram. . . . .	17
2.6	(a) Distributed parameter model of a composite right-left-handed transmission line and (b) corresponding dispersion diagram. . . . .	17
2.7	(a) Equivalent circuit representation of a metamaterial unit cell of size $d \ll \lambda$ with (b) Drude and (c) Lorentz dispersion as taken from [126].	20
2.8	(a) Material parameters of a Lorentz dispersive medium with equal $\epsilon_r(\omega)$ and $\mu_r(\omega)$ , (b) corresponding dispersion relation. . . . .	22
2.9	Various inclusion types (arranged in a periodic lattice) used in the realization of metamaterials. Insets show the equivalent circuit representation. . . . .	23
2.10	Realization of CRLH transmission line metamaterials, (a) 1D [17], (b) 2D [60] and (c) 3D [124]. . . . .	24
2.11	(a) Operation principle and realization of a 2D cylindrical metamaterial cloak with (b) plane wave scattering, taken from [98]. . . . .	26
2.12	Simulation volume consisting of a unit cell, (a) strip-SRR and (b) CLS-SRR metamaterial. . . . .	29
2.13	Physical dimensions of (a) SRR (b) strip and (c) CLS inclusion. . . . .	29
2.14	(a) Magnitude and (b) phase of R and T for the strip-SRR metamaterial in Tab. 2.2. $R^{\text{eff}}$ , $T^{\text{eff}}$ (solid line) and $R^{\text{sim}}$ , $T^{\text{sim}}$ (dotted line). . . . .	31
2.15	Extracted (a) $\epsilon_r^{\text{eff}}(\omega)$ and $\mu_r^{\text{eff}}(\omega)$ and (b) $n^{\text{eff}}$ for the strip-SRR metamaterial given in Tab. 2.2. . . . .	31

## LIST OF FIGURES

---

2.16	(a) Magnitude and (b) phase of R and T for the CLS-SRR metamaterial with parameters as in row IV of Tab. 2.5. $R^{\text{eff}}$ , $T^{\text{eff}}$ (solid line) and $R^{\text{sim}}$ , $T^{\text{sim}}$ (dotted line). . . . .	33
2.17	Extracted (a) $\epsilon_r^{\text{eff}}(\omega)$ and $\mu_r^{\text{eff}}(\omega)$ and (b) $n^{\text{eff}}$ for the CLS-SRR metamaterial given in row IV of Tab. 2.5. . . . .	33
3.1	(a) Focusing of propagating modes (solid lines) and recovery of evanescent modes (dashed line) by a double negative metamaterial slab perfectly matched to vacuum, (b) MEFiSTo-3D Pro <sup>®</sup> simulation showing a snapshot of the electric field distribution. . . . .	36
3.2	Problem setup in (a) 3D and (b) 2D. . . . .	38
3.3	Analytic properties of (a) $\text{Re}\{k_{1z}\}$ and (b) $\text{Im}\{k_{1z}\}$ in the $k_t$ plane. . . . .	40
3.4	Integration contour. . . . .	41
3.5	(a) Considered configuration and (b) intensity pattern at transversal planes, showing the spot size $\Delta y$ determined from the FWHM value of the main lobe. . . . .	45
3.6	$T^{\text{T}}(k_t)$ for a slab with material parameters as given in (3.24). . . . .	46
3.7	$ \mathbf{E} $ along the y axis at image plane $z = 0.4\lambda$ ( $x = 0$ ) for (a) $\mathbf{J}_0 = \hat{\mathbf{z}}$ and (b) $\mathbf{J}_0 = \hat{\mathbf{x}}$ . The dipole field in the ideal case is shown for comparison purposes. Corresponding normalized field intensities for (c) $\mathbf{J}_0 = \hat{\mathbf{z}}$ and (d) $\mathbf{J}_0 = \hat{\mathbf{x}}$ . Squares: diffraction limited intensity distribution. . . . .	47
3.8	$ \mathbf{E} $ in the $yz$ plane, immediately behind the slab. Perpendicular $\mathbf{J}_0 = \hat{\mathbf{z}}$ and parallel $\mathbf{J}_0 = \hat{\mathbf{x}}$ source excitation for $\Gamma = 10^{-6}$ and $\Gamma = 10^{-10}$ . The image plane is shown by the dashed line. . . . .	48
3.9	$I_{\text{diff}}$ for the same configurations in Fig. 3.8. . . . .	48
3.10	$T^{\text{T}}(k_t)$ for a slab with material parameters as given in (3.26) . . . . .	50
3.11	$ \mathbf{E} $ along the y axis at image plane $z = 0.4\lambda$ ( $x = 0$ ) for (a) $\mathbf{J}_0 = \hat{\mathbf{z}}$ and (b) $\mathbf{J}_0 = \hat{\mathbf{x}}$ . The dipole field in the ideal case is shown for comparison purposes. Corresponding normalized field intensities for (c) $\mathbf{J}_0 = \hat{\mathbf{z}}$ and (d) $\mathbf{J}_0 = \hat{\mathbf{x}}$ . Squares: diffraction limited intensity distribution. . . . .	50
3.12	$T^{\text{T}}(k_t)$ for a slab with material parameters as given in (3.29). . . . .	52
3.13	(a) $I_{\text{norm}}^{\text{yz}}$ and (b) $I_{\text{diff}}^{\text{yz}}$ for $\mathbf{J}_0 = \hat{\mathbf{z}}$ (top row) and $\mathbf{J}_0 = \hat{\mathbf{x}}$ (bottom row). . . . .	53
3.14	(a) $I_{\text{norm}}^{\text{xy}}$ and (b) $I_{\text{diff}}^{\text{xy}}$ at the image plane for $\mathbf{J}_0 = \hat{\mathbf{z}}$ (top row) and $\mathbf{J}_0 = \hat{\mathbf{x}}$ (bottom row). . . . .	54
3.15	(a) $ T^{\text{T}}(k_t) $ for $0.2\lambda < d < \lambda$ and (b) FWHM at image plane ( $x = 0$ , $y \neq 0$ , $z = 2d -  z_0 $ ) with source at $z_0 = -0.2\lambda$ . . . . .	56
3.16	MEFiSTo-3D Pro <sup>®</sup> simulation volume with $d = 2\lambda$ and $z_0 = -\lambda$ and image plane at $z = 3\lambda$ . . . . .	56
3.17	$\Delta y$ vs. aperture size A at image plane. . . . .	57
3.18	(a) Gaussian pulse in time and frequency domains and (b) Drude dispersive refractive index of the slab. . . . .	58

3.19 (a) Variation of the image plane field intensity with an excitation pulse having a central frequency of $\nu_0 = 10$ GHz and 3dB bandwidth ranging from 0 to 5 GHz. (b) FWHM at image plane vs. pulse width $\Delta\nu$ for pulses with central frequency $\nu_0$ . . . . .	58
4.1 (a) General absorber backed by a metallic ground and (b) realization in terms of metallic strip, CLS and SRR inclusions. . . . .	63
4.2 Extracted effective material parameters for config. IV in Tab. 4.1. . . . .	65
4.3 Plot of $ R  = 0$ as a function of $\nu_{pe}$ and $\nu_i$ . . . . .	66
4.4 $ R $ for configurations (a) III and (b) IV in Tab. 4.1 obtained with effective medium approach (solid line) and full wave simulation (dotted line). . . . .	66
4.5 $ R $ for configurations (a) I and (b) II in Tab. 4.2 obtained with effective medium approach (solid line) and full wave simulation (dotted line). . . . .	67
4.6 (a) Composition of the metamaterial low reflection coating (MTM-LRC) with capacitively loaded strip (CLS) inclusions, and (b) equivalent circuit model for TEM wave excitation with $E_x, H_y, k_z$ . . . . .	69
4.7 (a) $ R(\nu) $ and (b) $Z_s(\nu)$ for the MTM-LRC described in Sec. 4.2.3. Results obtained with equivalent circuit model (solid, dashed line) and full wave simulation (dotted line). . . . .	72
4.8 $ R $ for configurations in Tab. 4.3. Results obtained with equivalent circuit model (solid line) and full wave simulation (dotted line). . . . .	73
4.9 (a) Effect of $l_1$ and (b) $l_2$ on $\nu_{res}$ . Results obtained with equivalent circuit model (solid line) and full wave simulation (dotted line). . . . .	74
4.10 (a) Effect of $a_z$ and (b) $\tan \delta$ on $ R(\nu_{res}) $ . Results obtained with equivalent circuit model (solid line) and full wave simulation (dotted line). . . . .	74
4.11 Simulation volume consisting of a unit cell with anisotropic (left) and isotropic (right) CLS. . . . .	75
4.12 (a) Angle and (b) polarization dependence of $ R(\nu_{res}) $ for anisotropic configuration. (c) Angle and (d) polarization dependence of $ R(\nu_{res}) $ for isotropic configuration. Only in (c): results obtained with full wave simulation (dotted line) and from (A.6) with $Z_s(\nu_{res}) = 250 - 30j$ (solid line). . . . .	76
4.13 (a) $ R(\nu) $ and (b) $Z_s(\nu)$ for the realized MTM-LRC as described in Sec. 4.2.6. In (a) the solid line represents measurement and the dotted line represents full wave simulation results. . . . .	77
4.14 (a) A portion of the manufactured MTM-LRC consisting of CLS inclusions. (b) Measurement setup with the coated cube at its center. The inset shows a magnification of a part of the MTM-LRC. . . . .	79
4.15 (a) Quasi-mono and (b) bistatic RCS measurement configurations. . . . .	79
4.16 Normalized monostatic RCS for the coated and uncoated cube with horizontal polarization at 36.925 GHz. . . . .	80

## LIST OF FIGURES

---

4.17	Normalized bistatic RCS for the coated and uncoated cube for incidence angles $\varphi_o = 10^\circ, 20^\circ, 30^\circ$ and $40^\circ$ . Horizontal polarization at 36.925 GHz. . . . .	80
4.18	Comparison between different methods for bistatic RCS of coated and uncoated cube at 36.925 GHz and horizontal polarization. (a) Measurement, HFSS <sup>®</sup> and BISTRO with $Z_s = 199 - 31j \Omega$ and (b) HFSS <sup>®</sup> with $Z_s = 377 \Omega$ (ideal case). . . . .	82
A.1	Reflection and transmission of plane electromagnetic waves incident on (a) semi-infinite media, (b) single layer slab of thickness $d$ and (c) same slab backed by a metallic ground. . . . .	88
B.1	Monostatic and bistatic RCS. . . . .	93
B.2	Scattering in spherical coordinates. . . . .	93

# List of Tables

2.1	Sign of wave parameters, reproduced from the results in [130]. . . . .	12
2.2	Physical dimensions of unit cell/inclusions and extracted parameters of a strip-SRR metamaterial with host permittivity $\epsilon_r^h = 4.4$ and loss tangent $\tan \delta = 0.02$ . . . . .	31
2.3	Effect of host permittivity $\epsilon_r^h$ (strip-SRR metamaterial). . . . .	34
2.4	Effect of physical dimensions on the extracted model parameters of a strip-SRR metamaterial. . . . .	34
2.5	Effect of physical dimensions on the extracted model parameters of a CLS-SRR metamaterial. . . . .	34
3.1	$k_t^c$ and $\Delta y$ at image plane $z = 0.4\lambda$ , for various values of $\Gamma$ . . . . .	46
3.2	Cutoff wavenumber $k_{te,tm}^c/k_0$ for material parameters as given in (3.29). . . . .	52
4.1	Drude-Lorentz model parameters for strip-SRR metamaterial absorber. . . . .	65
4.2	Lorentz-Lorentz model parameters for CLS-SRR metamaterial absorber. . . . .	67
4.3	Dependence of $\nu_{res}$ on $l_1$ , $l_2$ and $c$ with $a_x = a_y = 1.4$ mm, $a_z = 0.1$ mm, $\epsilon_r = 4.4$ and $\tan \delta = 0.02$ . . . . .	73



# Abbreviations and Symbols

AIS	artificial impedance surface	TLM	transmission line matrix
BW	backward wave	$\epsilon$	permittivity
CLS	capacitively loaded strips	$\epsilon_0$	vacuum permittivity
CRLH	composite right-left-handed	$\epsilon_r$	relative permittivity
CW	cut wire	$\epsilon_r(\infty)$	high frequency relative permittivity
DNG	double negative	$\epsilon_r^h$	relative host permittivity
EBG	electromagnetic bandgap	$\epsilon_r^{\text{eff}}$	relative effective permittivity
FSS	frequency selective surface	$\eta$	characteristic impedance
FWHM	full width at half maximum	$\Gamma$	loss factor
HIS	high impedance surface	$\Gamma_e$	electric loss factor
LH	left handed	$\Gamma_m$	magnetic loss factor
LRC	low reflection coating	$\lambda$	wavelength
MTM	metamaterial	$\mu$	permeability
NRI	negative refractive index	$\mu_0$	vacuum permeability
PEC	perfect electric conductor	$\mu_r$	relative permeability
PFDM	parameter fitting of dispersive models	$\mu_r(\infty)$	high frequency relative permeability
PMC	perfect magnetic conductor	$\mu_r^{\text{eff}}$	relative effective permeability
PML	perfectly matched layer	$\nu$	frequency
PTD	physical theory of diffraction	$\omega$	angular frequency
RAM	radar absorbing material	$\omega_0$	angular resonance frequency
RCS	radar cross section	$\omega_p$	angular plasma or cutoff frequency
RCSR	radar cross section reduction	$\omega_{0e}$	electric angular resonance frequency
RH	right handed	$\omega_{0m}$	magnetic angular resonance frequency
SRR	split ring resonator	$\omega_{pe}$	electric angular plasma or cutoff frequency
TL	transmission line	$\omega_{pm}$	magnetic angular plasma or cutoff frequency
		<b>B</b>	magnetic flux density vector
		<b>D</b>	electric displacement vector
		<b>E</b>	electric field vector
		<b>H</b>	magnetic field vector
		<b>I</b>	intensity
		<b>k</b>	wave vector
		<b>R</b>	reflection coefficient
		<b>r</b>	position vector

## ABBREVIATIONS AND SYMBOLS

---

<b>S</b>	Poynting vector	$c_0$	speed of light in vacuum
<b>T</b>	transmission coefficient	$k$	wavenumber
<b>C</b>	capacitance	$k_0$	angular wavenumber in vacuum
<b>L</b>	inductance	$n$	refractive index
$\tan \delta$	loss tangent	$t$	time
<b>W</b>	energy density	$v_g$	group velocity
<b>Y</b>	admittance	$v_p$	phase velocity
<b>Z</b>	impedance		

# References

- [1] P. Alitalo, F. Bongard, J. Zuercher, J. Mosig, and S. A. Tretyakov. Experimental verification of broadband cloaking using a volumetric cloak composed of periodically stacked cylindrical transmission-line networks. *Applied Physics Letters*, 94:014103, 2009. (pages 3, 26).
- [2] P. Alitalo, A. Culhaoglu, A. Osipov, S. Thurner, E. Kemptner, and S. A. Tretyakov. Experimental characterization of a broadband transmission-line cloak in free space. *Antennas and Propagation, IEEE Transactions on*, submitted, 2011. (page 26).
- [3] P. Alitalo, S. Maslovski, and S. A. Tretyakov. Experimental verification of the key properties of a three-dimensional isotropic transmission-line superlens. *Journal of Applied Physics*, 99:124910, 2006. (pages 2, 25, 35).
- [4] P. Alitalo, S. Maslovski, and S. A. Tretyakov. Three-dimensional isotropic perfect lens based on LC-loaded transmission lines. *Journal of Applied Physics*, 99:064912, 2006. (page 25).
- [5] A. Alù and N. Engheta. Achieving transparency with plasmonic and metamaterial coatings. *Phys. Rev. E*, 72(1):016623, Jul 2005. (pages 3, 27).
- [6] A. Alù and N. Engheta. Plasmonic and metamaterial cloaking: physical mechanisms and potentials. *Journal of Optics A: Pure and Applied Optics*, 10(9):093002, 2008. (page 27).
- [7] ANSYS, Inc., Southpointe 275, Technology Drive, Canonsburg, PA 15317, USA. *High Frequency Structure Simulator (HFSS), ver. 11*. (page 28).
- [8] K. Aydin and E. Ozbay. Capacitor-loaded split ring resonators as tunable metamaterial components. *Journal of Applied Physics*, 101:024911, 2007. (page 23).
- [9] I. Bahl. *Lumped Elements for RF and Microwave Circuits*. Artech House, 2003. (pages 69, 70, 71).
- [10] S. E. Bankov. Analytic study of electromagnetic-field focusing by a Veselago lens. *Journal of Communications Technology and Electronics*, 54(2):123–133, 2009. (page 2).

## REFERENCES

---

- [11] F. Bilotti, L. Nucci, and L. Vegni. An SRR based microwave absorber. *Microwave and Optical Technology Letters*, 48(11):2171–2175, 2006. (page 27).
- [12] F. Bilotti and L. Vegni. Metamaterial-inspired electrically small radiators: it is time to draw preliminary conclusions and depict the future challenges. In *Proceedings of the 3rd International Congress on Advanced Electromagnetic Materials in Microwaves and Optics*, London, UK, Sept 2009. (page 25).
- [13] J. Brown. Artificial dielectrics. *Progress in Dielectrics*, 2:195–225, 1960. (page 8).
- [14] I. Bulu, H. Caglayan, and E. Ozbay. Experimental demonstration of labyrinth-based left-handed metamaterials. *Optics Express*, 13(25):10238, 2005. (page 23).
- [15] C. Caloz. Perspectives on EM metamaterials. *Materials Today*, 12(3):12–20, 2009. (page 25).
- [16] C. Caloz and T. Itoh. *Electromagnetic Metamaterials: Transmission Line Theory and Microwave Applications*. Wiley, 2004. (pages 1, 7, 9, 13, 15, 16, 18, 24, 25).
- [17] C. Caloz and T. Itoh. Transmission line approach of left-handed (LH) materials and microstrip implementation of an artificial LH transmission line. *Antennas and Propagation, IEEE Transactions on*, 52(5):1159–1166, 2004. (pages 24, 95).
- [18] F. Capolino. *Theory and Phenomena of Metamaterials*. CRC-Press, 2009. (page 1).
- [19] W. C. Chew. Sommerfeld integrals for left-handed materials. *Microwave and Optical Technology Letters*, 42(5):369–372, 2004. (page 2).
- [20] F. Costa, A. Monorchio, and G. Manara. Analysis and design of ultra thin electromagnetic absorbers comprising resistively loaded high impedance surfaces. *Antennas and Propagation, IEEE Transactions on*, 58(5):8, 2010. (pages 61, 68).
- [21] A. Culhaoglu, A. Osipov, and P. Russer. Numerical analysis of focusing by a metamaterial lens. In *Proceedings of the Vth International Workshop on Electromagnetic Wave Scattering*, Antalya, Turkey, 2008. (pages 4, 43).
- [22] A. Culhaoglu, A. Osipov, and P. Russer. Numerical study of focusing by a composite right left handed metamaterial with Drude dispersion characteristics. In *Proceedings of the 2nd International Congress on Advanced Electromagnetic Materials in Microwaves and Optics*, Pamplona, Spain, 2008. (page 4).
- [23] A. Culhaoglu, A. Osipov, and P. Russer. Determination of spectral focusing features of a metamaterial slab. In *Proceedings ACES 2009*, Monterey California, USA, 2009. (pages 4, 43).

- 
- [24] A. Culhaoglu, A. Osipov, and P. Russer. Towards low reflection microwave coatings with Lorentz dispersive metamaterials. In *Proceedings of the IVth International Congress on Advanced Electromagnetic Materials in Microwaves and Optics*, Karlsruhe, Germany, 2010. (pages 4, 67).
- [25] A. Culhaoglu, A. Osipov, and P. Russer. Metamaterial slab excited by an arbitrarily oriented dipole. In *General Assembly and Scientific Symposium, 2011 XXXth URSI*, Istanbul, Turkey, 2011. (pages 4, 45).
- [26] A. Culhaoglu, A. Osipov, and P. Russer. Scattering reduction by a metamaterial low reflection coating. *Antennas and Propagation, IEEE Transactions on*, submitted, 2011. (page 4).
- [27] A. Culhaoglu, M. Zedler, W. J. R. Hoefler, A. Osipov, and P. Russer. Full wave numerical simulation of a finite 3D metamaterial lens. In *Proceedings ACES 2008*, Niagara Falls, Canada, 2008. (pages 4, 56).
- [28] S. A. Cummer. Simulated causal subwavelength focusing by a negative refractive index slab. *Applied Physics Letters*, 82(10):1503–1506, 2003. (pages 2, 35, 44).
- [29] G. Donzelli, A. Vallecchi, F. Capolino, and A. Schuchinsky. Metamaterial made of paired planar conductors: Particle resonances, phenomena and properties. *Metamaterials*, 3:10–27, 2009. (page 24).
- [30] G. V. Eleftheriades. EM transmission-line metamaterials. *Materials Today*, 12(3):30–41, 2009. (page 24).
- [31] G. V. Eleftheriades and K. G. Balmain. *Negative-Refractive Metamaterials: Fundamental Principles and Applications*. Wiley-IEEE Press, 2005. (pages 1, 9, 13, 18, 19, 24, 95).
- [32] N. Engheta. An idea for thin subwavelength cavity resonators using metamaterials with negative permittivity and permeability. *IEEE Antennas and Wireless Propagation Letters*, 1:10–13, 2002. (page 25).
- [33] N. Engheta. Thin absorbing screens using metamaterial surfaces. In *Antennas and Propagation Society International Symposium, IEEE*, pages 392–395, vol.2, 2002. (pages 3, 27, 61, 68).
- [34] N. Engheta and R. W. Ziolkowski. *Metamaterials: Physics and Engineering Explorations*. Wiley-IEEE, 2006. (pages 1, 13, 19).
- [35] A. Erentok, P. Luljak, and R. W. Ziolkowski. Characterization of a volumetric metamaterial realization of an artificial magnetic conductor for antenna applications. *Antennas and Propagation, IEEE Transactions on*, 53(1):160–172, 2005. (page 25).

## REFERENCES

---

- [36] T. Ergin, N. Stenger, P. Brenner, J. B. Pendry, and M. Wegener. Three-dimensional invisibility cloak at optical wavelengths. *Science*, 328(5976):337–339, 2010. (pages 3, 27).
- [37] N. Fang and X. Zhang. Imaging properties of a metamaterial superlens. *Applied Physics Letters*, 82(2):161–163, 2003. (page 2).
- [38] Faustus Scientific Corporation, 1256 Beach Drive, Victoria, BC, Canada. *MEFiSTo-3D Pro, version 5.0*. (pages 5, 36, 57, 58).
- [39] L. B. Felsen and N. Marcuvitz. *Radiation and Scattering of Waves*. IEEE Press, 1994. (pages 5, 35, 37, 42).
- [40] R. P. Feynman, R. B. Leighton, and M. Sands. *The Feynman Lectures on Physics including Feynman’s Tips on Physics: The Definitive and Extended Edition*. Addison Wesley, 2nd edition, 2005. (page 19).
- [41] M. J. Freire, R. Marques, and L. Jelinek. Experimental demonstration of a  $\mu = -1$  metamaterial lens for magnetic resonance imaging. *Applied Physics Letters*, 93(231108), 2008. (page 35).
- [42] O. E. French, K. I. Hopcraft, and E. Jakeman. Perturbation on the perfect lens: the near-perfect lens. *New Journal of Physics*, 8(271), 2006. (page 43).
- [43] J. Garcia-Garcia, F. Martin, J. D. Baena, R. Marques, and L. Jelinek. On the resonances and polarizabilities of split ring resonators. *Journal of Applied Physics*, 98(3):033103, 2005. (page 23).
- [44] P. Gay-Balmaz and O. J. F. Martina. Electromagnetic resonances in individual and coupled split-ring resonators. *Journal of Applied Physics*, 92(5):2929–2936, 2002. (page 23).
- [45] M. Gil, J. Bonachea, and F. Martin. Metamaterial filters: A review. *Metamaterials*, 2(4):186–197, 2008. (page 25).
- [46] G. Gómez-Santos. Universal features of the time evolution of evanescent modes in a left-handed perfect lens. *Phys. Rev. Lett.*, 90:077401, Feb 2003. (page 57).
- [47] I. S. Gradshteyn and I. M. Ryzik. *Table of Integrals, Series and Products*. Academic Press, 7th edition, 2007. (page 43).
- [48] A. Grbic and G. V. Eleftheriades. Overcoming the diffraction limit with a planar left-handed transmission-line lens. *Physical Review Letters*, 92(11):117403, 2004. (pages 2, 35).
- [49] A. Grbic and G. V. Eleftheriades. An isotropic three-dimensional negative-refractive-index transmission line metamaterial. *Journal of Applied Physics*, 98(20), 2005. (page 25).

- 
- [50] W. Hardy and L. Whitehead. Split-ring resonator for use in magnetic resonance from 200-2000 MHz. *Review of Scientific Instruments*, 52(2):213–216, 1981. (page 8).
- [51] R. Hedge, Y. L. Hor, Z. Szabo, E. P. Li, and W. Hoefer. Veselago-Pendry superlens imaging modeled with a spectral waveguide approach. In *General Assembly and Scientific Symposium, 2011 XXXth URSI*, Istanbul, Turkey, 2011. (page 57).
- [52] R. Hegde, Z. Szabo, Y. L. Hor, Y. E. P. L. Kiasat, E. P. Li, and W. Hoefer. The dynamics of nanoscale superresolution imaging with the superlens. *Microwave Theory and Techniques, IEEE Transactions on*, 59(10):2612 – 2623, 2011. (page 57).
- [53] L. E. Helseth. The almost perfect lens and focusing of evanescent waves. *Optics Communications*, 281:1981–1985, 2008. (page 35).
- [54] W. Hoefer. *The transmission line matrix (TLM) method, Chap. 8 of Numerical Techniques for microwave and millimeter-wave passive structures*. John Wiley and sons, 1989. (pages 5, 36).
- [55] W. J. R. Hoefer, P. P. M. So, D. Thompson, and M. M. Tentzeris. Topology and design of wide-band 3D metamaterials made of periodically loaded transmission lines. In *Microwave Symposium Digest, 2005 IEEE MTT-S International*, 2005. (page 25).
- [56] Y. L. Hor, R. Hegde, E. P. Li, and W. Hoefer. Transient study of the dynamic response of the Veselago-Pendry superlens. In *Microwave Symposium Digest (MTT), 2011 IEEE MTT-S International*, pages 1–4, Baltimore, MD, USA, 2011. (page 57).
- [57] A. Ishimaru. *Electromagnetic Wave Propagation, Radiation and Scattering*. Prentice Hall, 1991. (pages 10, 19, 37, 43, 87).
- [58] R. Islam and G. V. Eleftheriades. Phase-agile branch-line couplers using metamaterial lines. *Microwave and Wireless Components Letters, IEEE*, 14(7):340–342, 2004. (page 25).
- [59] A. Iyer and G. Eleftheriades. Free-space sub-diffraction imaging using a transmission-line superlens. In *Antennas and Propagation Society International Symposium, 2008. AP-S 2008. IEEE*, pages 1–4, july 2008. (pages 2, 35).
- [60] A. Iyer and G. V. Eleftheriades. Negative refractive index metamaterials supporting 2-D waves. In *Microwave Symposium Digest, 2002 IEEE MTT-S International*, pages 1067–1070, Seattle, WA , USA, 2002. (pages 24, 95).
- [61] A. K. Iyer and G. V. Eleftheriades. Mechanisms of subdiffraction free-space imaging using a transmission-line metamaterial superlens: An experimental verification. *Applied Physics Letters*, 92(13):131105, 2008. (pages 2, 35).

## REFERENCES

---

- [62] J. D. Joannopoulos, S. G. Johnson, J. N. Winn, and R. D. Meade. *Photonic Crystals: Molding the Flow of Light*. Princeton University Press, 2nd edition, 2008. (page 9).
- [63] P. Johns and R. L. Beurle. Numerical modeling of 2-dimensional scattering problems using a transmission line matrix. *Proceedings of IEEE*, 118(9):1203–1208, 1971. (pages 5, 36).
- [64] E. F. Knott. *Radar Cross Section*. Artech House, 2nd edition, 1993. (pages 3, 61, 91).
- [65] W. E. Kock. Metal-lens antennas. *Proceedings of the IRE*, 34(11):828–836, 1946. (page 7).
- [66] T. Koschny, P. Markos, D. R. Smith, and C. M. Soukoulis. Resonant and antiresonant frequency dependence of the effective parameters of metamaterials. *Physical Review E*, 68:065602, 2003. (page 27).
- [67] T. Koschny, L. Zhang, and C. M. Soukoulis. Isotropic three-dimensional left-handed metamaterials. *Physical Review B*, 71:121103, 2005. (page 25).
- [68] D. Kwon, D. H. Werner, A. V. Kildishev, and V. M. Shalaev. Material parameter retrieval procedure for general bi-isotropic metamaterials and its application to optical chiral negative-index metamaterial design. *Optics Express*, 16:11822–11829, 2008. (page 27).
- [69] A. N. Lagarkov and V. N. Kissel. Near-perfect imaging in a focusing system based on a left-handed-material plate. *Physical Review Letters*, 92(077401), 2004. (page 35).
- [70] L. D. Landau and E. M. Lifshitz. *Electrodynamics of Continuous Media*. Pergamon Press, 2nd edition, 1984. (pages 19, 20).
- [71] M. Lapine, L. Jelinek, M. J. Freire, and R. Marques. Realistic metamaterial lenses: Limitations imposed by discrete structure. *Physical Review B*, 82(165124):39663969, 2010. (page 35).
- [72] M. Lapine and S. A. Tretyakov. Contemporary notes on metamaterials. *Microwaves, Antennas and Propagation, IET*, 1(1):3–11, 2007. (pages 1, 2, 7).
- [73] U. Leonhardt. Optical conformal mapping. *Science*, 312:1777–1780, 2006. (page 26).
- [74] Z. Li, K. Aydin, and E. Ozbay. Determination of the effective constitutive parameters of bianisotropic metamaterials from reflection and transmission coefficients. *Physical Review E*, 79:026610, 2009. (page 27).
- [75] L. Liu, C. Caloz, and T. Itoh. Dominant mode leaky-wave antenna with backfire-to-endfire scanning capability. *Electronics Letters*, 38(23):1414–1416, 2002. (page 25).

- 
- [76] G. Lubkowski, R. Schuhmann, and T. Weiland. Extraction of effective meta-material parameters by parameter fitting of dispersive models. *Microwave and Optical Technology Letters*, 49(2):285–288, 2007. (pages 4, 5, 28).
- [77] O. Luukkonen, F. Costa, C. R. Simovski, A. Monorchio, and S. A. Tretyakov. A thin electromagnetic absorber for wide incidence angles and both polarizations. *Antennas and Propagation, IEEE Transactions on*, 57(10):3119–3125, 2009. (pages 61, 68).
- [78] R. Marques and J. Baena. Effect of losses and dispersion on the focusing properties of left-handed media. *Microwave and Optical Technology Letters*, 41(4):290–294, 2004. (pages 2, 35).
- [79] R. Marques, F. Martin, and M. Sorolla. *Metamaterials with Negative Parameters: Theory, Design and Microwave Applications*. Wiley, 2008. (pages 1, 3, 36, 48).
- [80] R. Marques, F. Mesa, J. Martel, and F. Medina. Comparative analysis of edge- and broadside-coupled split ring resonators for metamaterial design - theory and experiments. *Antennas and Propagation, IEEE Transactions on*, 51(10):2572–2581, 2003. (page 23).
- [81] S. Maslovski, P. Ikonen, I. Kolmakov, and S. A. Tretyakov. Artificial magnetic materials based on the new magnetic particle: Metasolenoid. *Progress In Electromagnetics Research*, 54:61–68, 2005. (page 23).
- [82] C. Menzel, C. Rockstuhl, T. Paul, F. Lederer, and T. Pertsch. Retrieving effective parameters for metamaterials at oblique incidence. *Physical Review B*, 77:195328, 2008. (page 27).
- [83] P. Mercure, R. Haley, A. Bogle, and L. Kempel. Three-dimensional isotropic metamaterials. In *Antennas and Propagation Society International Symposium, 2005 IEEE*, pages 623–626, 2005. (page 25).
- [84] R. Merlin. Analytical solution of the almost-perfect-lens problem. *Applied Physics Letters*, 84(8):1290–1292, 2004. (pages 2, 35, 43).
- [85] B. A. Munk. *Frequency Selective Surfaces: Theory and Design*. Wiley, 2000. (pages 9, 68, 77).
- [86] A. M. Nicolson and G. Ross. Measurement of the intrinsic properties of materials by time domain techniques. *IEEE Trans. Instrum.*, IM-19:377–382, 1970. (page 27).
- [87] E. Ozbay, K. Aydin, E. Cubukcu, and M. Bayindir. Transmission and reflection properties of composite double negative metamaterials in free space. *Antennas and Propagation, IEEE Transactions on*, 51:2592, 2003. (page 23).

## REFERENCES

---

- [88] J. B. Pendry. Negative refraction makes a perfect lens. *Physical Review Letters*, 85:3966–3969, 2000. (pages 2, 35, 37).
- [89] J. B. Pendry, A. J. Holden, D. J. Robbins, and W. J. Stewart. Low frequency plasmons in thin-wire structures. *Journal of Physics: Condensed Matter*, 10:4785–4809, 1998. (page 8).
- [90] J. B. Pendry, A. J. Holden, D. J. Robbins, and W. J. Stewart. Magnetism from conductors and enhanced nonlinear phenomena. *Microwave Theory and Techniques, IEEE Transactions on*, 47(11):2075–2084, 1999. (page 8).
- [91] J. B. Pendry, D. Schurig, and D. R. Smith. Controlling electromagnetic fields. *Science*, 312(5781):1780–1782, 2006. (page 26).
- [92] E. Plum, J. Zhou, J. Dong, V. A. Fedotov, T. Koschny, C. M. Soukoulis, and N. I. Zheludev. Metamaterial with negative index due to chirality. *Physical Review B*, 79:035407, 2009. (page 27).
- [93] W. H. Press, S. A. Teukolsky, W. T. Vetterling, and B. P. Flannery. *Numerical Recipes: The Art of Scientific Computing*. Cambridge University Press, 3rd edition, 2007. (page 42).
- [94] G. T. Ruck. *Radar Cross Section Handbook*, volume 2. Plenum Press, 1970. (pages 3, 61, 91).
- [95] P. Russer. *Electromagnetics, Microwave Circuit, and Antenna Design for Communications Engineering*. Artech House, 2nd edition, 2006. (pages 13, 24).
- [96] B. Sauviac, C. R. Simovski, and S. A. Tretyakov. Double split ring resonators: Analytical modeling and numerical simulations. *Electromagnetics*, 24(5):317–338, 2004. (pages 23, 32).
- [97] S. Schelkunoff and H. Friis. *Antennas: Theory and Practice*. Wiley, 1952. (page 8).
- [98] D. Schurig, J. J. Mock, B. J. Justice, S. A. Cummer, J. B. Pendry, A. F. Starr, and D. R. Smith. Metamaterial electromagnetic cloak at microwave frequencies. *Science*, 314(5801):977–980, 2006. (pages 3, 26, 95).
- [99] A. Schuster. *An Introduction to the Theory of Optics*. Edward Arnold, London, 1904. (page 13).
- [100] V. M. Shalaev, W. Cai, U. K. Chettiar, H. Yuan, A. K. Sarychev, V. P. Drachev, and A. V. Kildishev. Negative index of refraction in optical metamaterials. *Optics Letters*, 30(24):3356–3358, 2005. (pages 10, 24).
- [101] R. A. Shelby, D. R. Smith, and S. Schultz. Experimental verification of a negative index of refraction. *Science*, 292(292):77–79, 2001. (pages 2, 9, 13, 95).

- 
- [102] L. Shen and S. He. Studies of imaging characteristics for a slab of a lossy left-handed material. *Physics Letters A*, 309:298–305, 2003. (pages 2, 35).
- [103] D. Sievenpiper. *High-impedance Electromagnetic Surfaces*. PhD thesis, UCLA, Ph.D. Dissertation, 1999. (page 10).
- [104] D. Sievenpiper, H. P. Hsu, J. Schaffner, G. Tangonan, R. Garcia, and S. Oniveros. Low-profile, four-sector diversity antenna on high-impedance ground plane. *Electronics Letters*, 36(23):1343–1345, 2000. (page 25).
- [105] D. Sievenpiper, L. Zhang, R. F. J. Broas, N. G. Alexopolous, and E. Yablonovitch. High-impedance electromagnetic surfaces with a forbidden frequency band. *Microwave Theory and Techniques, IEEE Transactions on*, 47(11):2059–2074, 1999. (page 10).
- [106] A. Sihvola. Metamaterials in electromagnetics. *Metamaterials*, 1(1):2–11, 2007. (pages 1, 7).
- [107] C. R. Simovski and B. Sauviac. Role of wave interaction of wires and splitting resonators for the losses in a left-handed composite. *Physical Review E*, 70(046607), 2004. (page 23).
- [108] D. R. Smith, W. J. Padilla, D. C. Vier, S. C. Nemat-Nasser, and S. Schultz. Composite medium with simultaneously negative permeability and permittivity. *Physical Review Letters*, 84(18):4184–4187, 2000. (pages 2, 8, 9, 95).
- [109] D. R. Smith and J. B. Pendry. Homogenization of metamaterials by field averaging. *Journal of the Optical Society of America B*, 23(3):391–403, 2006. (page 28).
- [110] D. R. Smith, D. Schurig, M. Rosenbluth, and S. Schultz. Limitations on sub-diffraction imaging with a negative refractive index slab. *Applied Physics Letters*, 82(10):1506–1508, 2003. (pages 2, 35, 43, 44).
- [111] D. R. Smith, D. C. Vier, T. Koschny, and C. M. Soukoulis. Electromagnetic parameter retrieval from inhomogeneous metamaterials. *Physical Review E*, 71:036617, 2005. (page 27).
- [112] P. M. So, H. Du, and W. J. R. Hoefer. Modeling of metamaterials with negative refractive index using 2-D shunt and 3-D SCN TLM networks. *Microwave Theory and Techniques, IEEE Transactions on*, 53(4):9480, 2005. (pages 36, 58).
- [113] H. Tao, W. J. Padilla, X. Zhang, and R. D. Averitt. Recent progress in electromagnetic metamaterial devices for terahertz applications. *IEEE Journal of Selected Topics in Quantum Electronics*, 99:1–10, 2010. (page 27).
- [114] S. A. Tretyakov. *Analytical Modeling in Applied Electromagnetics*. Artech, 2003. (pages 3, 9, 22, 24, 27).

## REFERENCES

---

- [115] A. Vallecchi, F. Capolino, and A. G. Schuchinsky. 2-D isotropic effective negative refractive index metamaterial in planar technology. *Microwave and Wireless Components Letters, IEEE*, 19(5):269–271, 2009. (page 24).
- [116] I. Vendik, O. Vendik, and M. Odit. Isotropic artificial media with simultaneously negative permittivity and permeability. *Microwave and Optical Technology Letters*, 48(12):2553–2556, 2006. (page 25).
- [117] V. G. Veselago. The electrodynamics of substances with simultaneously negative values of  $\epsilon$  and  $\mu$ . *Soviet Physics Uspekhi*, 10(4):509–514, 1968. (pages 2, 13, 35).
- [118] J. B. Weir. Automatic measurement of complex dielectric constant and permeability at microwave frequencies. *Proc. IEEE*, 62:33–36, 1974. (page 27).
- [119] J. D. Wilson and Z. D. Schwartz. Multifocal flat lens with left-handed metamaterial. *Applied Physics Letters*, 86(021113), 2005. (page 35).
- [120] M. C. K. Wiltshire, J. B. Pendry, I. R. Young, D. J. Larkman, D. J. Gilderdale, and J. V. Hajnal. Microstructured magnetic materials for RF flux guides in magnetic resonance imaging. *Science*, 291(5505):849–851, 2001. (pages 8, 9, 95).
- [121] E. Yablonovitch. Inhibited spontaneous emission in solid-state physics and electronics. *Physical Review Letters*, 58(20):20592062, 1987. (page 9).
- [122] E. Yablonovitch. Photonic bandgap structures. *Journal of the Optical Society of America B*, 10:283–295, 1993. (page 9).
- [123] M. Zedler. *Systematic Topological Design of Metamaterials: Scalar and Vectorial 3D Metamaterials and their Realisation*. PhD thesis, Technische Universität München, Lehrstuhl für Hochfrequenztechnik, 2008. (pages 13, 18, 19, 25).
- [124] M. Zedler, C. Caloz, and P. Russer. A 3D isotropic left-handed metamaterial based on the rotated transmission line matrix (tln) scheme. *Springer Proceedings in Physics*, 121:239–262, 2008. (pages 24, 25, 95).
- [125] M. Zedler and P. Russer. Three-dimensional CRLH metamaterials for microwave applications. *Proceedings of the European Microwave Association*, 3:151–162, 2006. (page 16).
- [126] M. Zedler, U. Siart, and P. Russer. Circuit theory unifying description for metamaterials. In *Proceedings of the URSI GA 2008*, page 623, Chicago, USA, July 2008. (pages 19, 20, 24, 95).
- [127] X. Zhang and Z. Liu. Superlenses to overcome the diffraction limit. *Nature Materials*, 7:435–441, 2008. (page 25).

- [128] J. Zhou, E. N. Economou, T. Koschny, and C. M. Soukoulis. Unifying approach to left-handed material design. *Optics Letters*, 31(24):3620–3622, 2006. (page 24).
- [129] R. Ziolkowski. Design, fabrication, and testing of double negative metamaterials. *Antennas and Propagation, IEEE Transactions on*, 51(7):1516–1529, 2003. (page 22).
- [130] R. Ziolkowski and E. Heyman. Wave propagation in media having negative permittivity and permeability. *Physical Review E*, 84(056625), 2001. (pages 2, 11, 12, 99).

## Curriculum Vitae

### Personal Data

Name	Ali Eren Culhaoglu
E-mail	ali.culhaoglu@dlr.de
Place and date of birth	Ankara, Turkey on March 30th, 1983
Nationality	Turkish

since 03/2011	German Aerospace Center (DLR), Oberpfaffenhofen Microwaves and Radar Institute Department of Security and Reconnaissance Research scientist
---------------	--

### Education

2004-2006	Technische Universität München Faculty of Informatics Computational Science and Engineering Master of Science (Pass with Merit)
2000-2004	Middle East Technical University, Ankara Faculty of Arts and Sciences Physics Bachelor of Science (High Honours)
1998-2000	Bilim College, Ankara High-school diploma
1989-1998	Private School of the German Embassy Ankara Successful completion of the 9th grade